ELECTROMAGNETIC INDUCTION SPECTROSCOPY FOR THE DETECTION OF SUBSURFACE TARGETS

A Thesis
Presented to
The Academic Faculty

by

Mu-Hsin Wei

In Partial Fulfillment
of the Requirements for the Degree
Doctor of Philosophy in the
School of Electrical and Computer Engineering

Georgia Institute of Technology
December 2012

ELECTROMAGNETIC INDUCTION SPECTROSCOPY FOR THE DETECTION OF SUBSURFACE TARGETS

Approved by:

James H. McClellan, Advisor
School of Electrical and Computer Engineering
Georgia Institute of Technology

Waymond R. Scott, Jr., Advisor
School of Electrical and Computer Engineering
Georgia Institute of Technology

Xiaoli Ma
School of Electrical and Computer Engineering
Georgia Institute of Technology

Gregory D. Durgin
School of Electrical and Computer Engineering
Georgia Institute of Technology

Ghassan Al-Regib
School of Electrical and Computer Engineering
Georgia Institute of Technology

J. Carlos Santamarina
School of Civil and Environmental Engineering
Georgia Institute of Technology

Date Approved: November 2, 2012

To my loving parents.

ACKNOWLEDGEMENTS

Many individuals contributed to the completion of this thesis. I would like to express my gratitude towards those who have walked with me throughout this long Ph.D. journey.

I am deeply grateful for my advisors Dr. James McClellan and Dr. Waymond Scott, for their patient guidance and valuable input. It has been a great privilege to work under their supervision. I would like to thank Dr. McClellan who provided direction and encouragement; I especially appreciate the care he shows for his students. I would like to thank Dr. Scott, who meticulously guided me since the beginning of the project. Many significant results from this thesis originated from his ideas.

I would like to thank my thesis committee members, Dr. Xiaoli Ma, Dr. Gregory Durgin, Dr. Ghassan Al-Regib, and Dr. J. Carlos Santamarina, for providing helpful contributions. Thanks also go to colleagues from the electromagnetics group, including Michael McFadden, Ricardo Lopez, Todd Lee, David Reid, James Sustman, Yoni Gabbay, and Mark Reed, for their interesting discussions and pleasant company in our office. I am also thankful for fellow students from the signal processing group, including Cafer Gurbuz, Chenchi Luo, Kyle Krueger, Carson Wick, Peter Tuuk, and Lingchen Zhu, for helpful discussions.

I have received much encouragement and support from my friends, especially Dr. David Huang, Dr. Michael Lo, Justin Chow, and Daniel Yao. Much of the credit of this work goes to these fantastic people. I would especially like to thank Fidela Chiang for being a great source of joy and help in many ways.

I owe my deepest gratitude to my parents, Dr. Yau-Huei Wei and Dr. Yeh-Jen Lin, who always support me and welcome me. I thank my sister Lily for her frequent encouragement and phone calls. I also acknowledge my brothers Tim and Sean, who despite being physically far away, are close to my heart.

Finally, with all that I am, I thank God, whose love never fails. Through Him, new things are born and new lives begin. The creativity that shaped this work belongs to Him.

This work is supported in part by the U. S. Army REDCOM CERDEC Night Vision and Electronic Sensors Directorate, Science and Technology Division, Countermine Branch and in part by the U. S. Army Research Laboratory and the U. S. Army Research Office under grant number W911NF-11-1-0153.

TABLE OF CONTENTS

LIST OF FIGURES

SUMMARY

This thesis presents a robust method for estimating the relaxations of a metallic object from its electromagnetic induction (EMI) response. The EMI response of a metallic object can be accurately modeled by a sum of real decaying exponentials. However, it is difficult to obtain the model parameters from measurements when the number of exponentials in the sum is unknown or the terms are strongly correlated. Traditionally, the relaxation constants are estimated by nonlinear iterative search that often leads to unsatisfactory results.

An effective EMI modeling technique is developed by first linearizing the problem through enumeration and then solving the linearized model using a sparsity-regularized minimization. This approach overcomes several long-standing challenges in EMI signal modeling, including finding the unknown model order as well as handling the ill-posed nature of the problem. The resulting algorithm does not require a good initial guess to converge to a satisfactory solution.

This new modeling technique is extended to incorporate multiple measurements in a single parameter estimation step. More accurate estimates are obtained by exploiting an invariance property of the EMI response, which states that the relaxation frequencies do not change for different locations and orientations of a metallic object. Using tests on synthetic data and laboratory measurement of known targets, the proposed multiple-measurement method is shown to provide accurate and stable estimates of the model parameters.

The ability to estimate the relaxation constants of targets enables more robust subsurface target discrimination using the relaxations. A simple relaxation-based subsurface target detection algorithm is developed to demonstrate the potential of the estimated relaxations.

CHAPTER I

INTRODUCTION

The landmine crisis remains today as landmines continue to maim or kill civilians everyday worldwide. The International Campaign to Ban Landmines reported that in the year of 2009, landmines and explosive remnants of war caused about 4000 casualties worldwide, of which over 60% are civilians [1] and more than 30% are children. Much effort and research has been invested in remediating landmines with one of the primary tasks being the detection of the landmine itself. However, landmine detection can suffer from a high false-alarm rate as the detectors also detect other metallic non-mine objects like gun shells, metal cans, and shrapnel. Therefore, it is of strong interest to discriminate between landmines and metallic non-mine objects.

Recent research has shown that broadband electromagnetic induction (EMI) sensors are capable of discriminating between certain types of targets [2–7]. Target discrimination using broadband EMI sensors is possible because the EMI response of a target is strongly related to the target's physical size, shape, orientation, and composition.

EMI sensors work by illuminating a target with a time-varying magnetic field, and then detecting the scattered magnetic field which is generated by the eddy currents induced on the target. The broadband EMI sensors measure the scattered field at a finite set of frequencies or over a short interval measurement times. The measured response can be fitted to a parametric model, and discrimination of targets is performed based on the fitted model parameters. This research is performed in the context of frequency-domain broadband EMI sensors, which have the advantage of avoiding undesired signal sources, such as power line harmonics.

The main contribution of this work is a new effective EMI modeling technique developed by first linearizing through enumeration and then solving the linearized model using a sparsity-regularized minimization. Furthermore, this approach is extended to incorporate

multiple measurements simultaneously, utilizing physical properties of the EMI signal in the modeling process, from which more accurate estimates are obtained. This approach overcomes several long standing challenges in EMI signal modeling, including the unknown model order as well as the ill-posed condition of the problem.

1.1 EMI Measurement System

This research is conducted as part of the development of a practical field measurement system to find buried targets. Shown in Fig. 1 is a measurement cart equipped with three frequency-domain broadband EMI sensors [8]. In the field, this cart is mobile, and when it is driven near a target, the EMI frequency response of the target is acquired sequentially, as illustrated in Fig. 2. As the cart moves, multiple EMI responses of a target are measured at different relative sensor-to-target positions and locations. In addition to the target response, the frequency response of the soil is also measured because soil is always present in the field and interacts with the EMI system. Therefore, the total response can be described as

$$\text{Total response} = \text{Target response} + \text{Soil response} + \text{System noise}. \tag{1}$$

The system noise is primarily due to the thermal noise introduced in the preamplifier of the system, which can be modeled as a Gaussian white noise [9].

Figure 1: A broadband EMI system mounted on a cart.

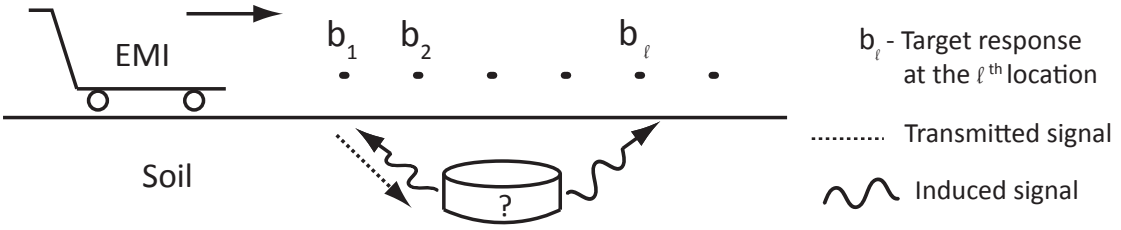

Figure 2: Sequential data acquisition of the EMI system.

To detect and discriminate subsurface targets in the scenario described above, a detection framework, shown in Fig. 3, is developed in this research. Given a measured response, the detection framework first passes the response through a soil prescreener to determine if only soil is present. If a soil-only decision cannot be made, then a metallic object might be present, and this response is then passed to an estimator where the response is fitted to an EMI model and the spectrum of the object is estimated. Lastly, a classifier using the estimated spectrum as a feature vector decides whether this response is from a landmine or clutter.

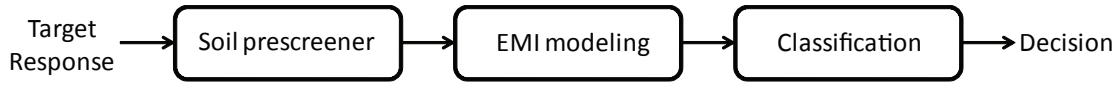

Figure 3: Block diagram for the a system that classifies target from measured EMI responses.

This research focuses on developing techniques to model the EMI response, or, equivalently, to estimate its underlying spectrum. The background for EMI modeling is presented in Section 1.2. To demonstrate target discrimination using the modeled response, classifiers and a soil prescreener are also developed. The background for target discrimination is presented in Section 1.3.

1.2 EMI Models

Several EMI models have been proposed, including ones for canonical targets [10, 11] and ones for targets of more general shape [12–14]. In general, these models are instances of a Fredholm integral equation of the first kind:

$$H(\omega) = g_0 + g_\Delta \int_0^\infty \frac{G(\tau)}{1 + j\omega\tau} \mathrm{d}\tau, \tag{2}$$

where $H(\omega)$ is the frequency response, τ the relaxation time, and g_0 and g_Δ are constants; $G(\tau)$ is the distribution function, or the spectrum.

Depending on characteristics of the distribution function, the EMI models assume a distribution of relaxations that is either continuous or discrete. These two types of spectra are examined in the following sections, where it is also shown that the discrete spectrum is appealing for the work in EMI discrimination because of its physical basis as well as its invariant properties.

1.2.1 Continuous Distribution of Relaxations

Miller et al. proposed a four-parameter model [14], which is also identified with the Cole-Cole model used in polymer science [15]:

$$H_{CC}(\omega) = g_0 + \frac{g_\Delta}{1 + (j\omega\tau_0)^\alpha}, \tag{3}$$

where τ_0 and α are model parameters. It is known from polymer science that this model has a *continuous* distribution of relaxation times (DRT)

$$G_{CC}(\tau) = \frac{1}{2\pi} \frac{\sin(\alpha\pi)}{\cosh(\alpha \log(\tau/\tau_0)) + \cos(\alpha\pi)}. \tag{4}$$

The Cole-Cole model assumes a DRT that is symmetric in $\log \tau$. However, not all targets have a symmetric DRT, e.g. a sphere [16]. More complex DRTs can be described by more complex models, such as the Cole-Davidson or the Havriliak-Negami model [17, 18]. Examples of these DRT models can be found in Fig. 6. While the Cole-Cole model may not exactly describe a target, it has been shown to be practical for target discrimination in the context of EMI [6, 7].

1.2.2 Discrete Spectrum of Relaxations

Several researchers have provided a theoretical basis for modeling the EMI response of a metallic object with an underlying *discrete* distribution of relaxations [12, 13]. In this case, the unit-step time response $h(t)$ is a discrete sum of damped real exponentials:

$$h(t) = d_0 u(t) - \sum_{k=1} d_k e^{-t/\tau_k} u(t), \tag{5}$$

where $\tau_k > 0$ are the real relaxation time constants, d_k the real-valued coefficients, and $u(t)$ the unit step function.

In the frequency domain, the EMI response can be written as

$$H(\omega) = c_0 + \sum_{k=1}^{K} c_k \frac{1 - j\omega/\zeta_k}{1 + j\omega/\zeta_k}, \tag{6}$$

where $\zeta_k = {\tau_k}^{-1}$ are the relaxation frequencies, c_0 the shift, c_k the real spectral amplitudes, and K the model order. Comparing (5) to (6), the model parameters are related by $d_0 = \sum_{k=0}^{K} c_k$ and $d_k = 2c_k$, where $d_0 = H(0)$ is due to the dc magnetization of the target. In this work, the parameter set $S = \{(\zeta_k, c_k) : k = 1 \ldots K\}$ is called the Discrete Spectrum of Relaxation Frequencies (DSRF) or simply the spectrum; each pair (ζ_k, c_k) is defined as one relaxation.

To visualize the time-domain and the frequency-domain model and their relationship, consider a response with $S = \{(10^4, 0.5), (10^5, 0.5)\}$ and $c_0 = -1$. The time-domain response is shown in Fig. 4, where $h(t)$ is a sum of two decaying exponentials. The frequency response $H(\omega)$ measured at 21 frequencies is shown in Fig. 5, where the real and imaginary parts of $H(\omega)$ are shown separately as well as together on an Argand diagram (complex plane), parameterized by ω. The plots of $H(\omega)$ in Fig. 5 illustrate an important fact about modeling the EMI response in which only a limited range of the response is observable. This constraint influences how accurately the true model of an EMI response can be recovered. It is difficult to recover relaxations that are far outside of the observable range because their contributions to the response may not be observed or are indistinguishable from the constant c_0.

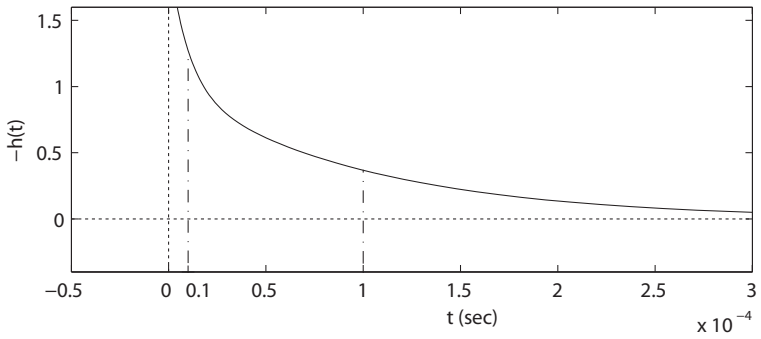

Figure 4: An example unit-step time response $h(t)$.

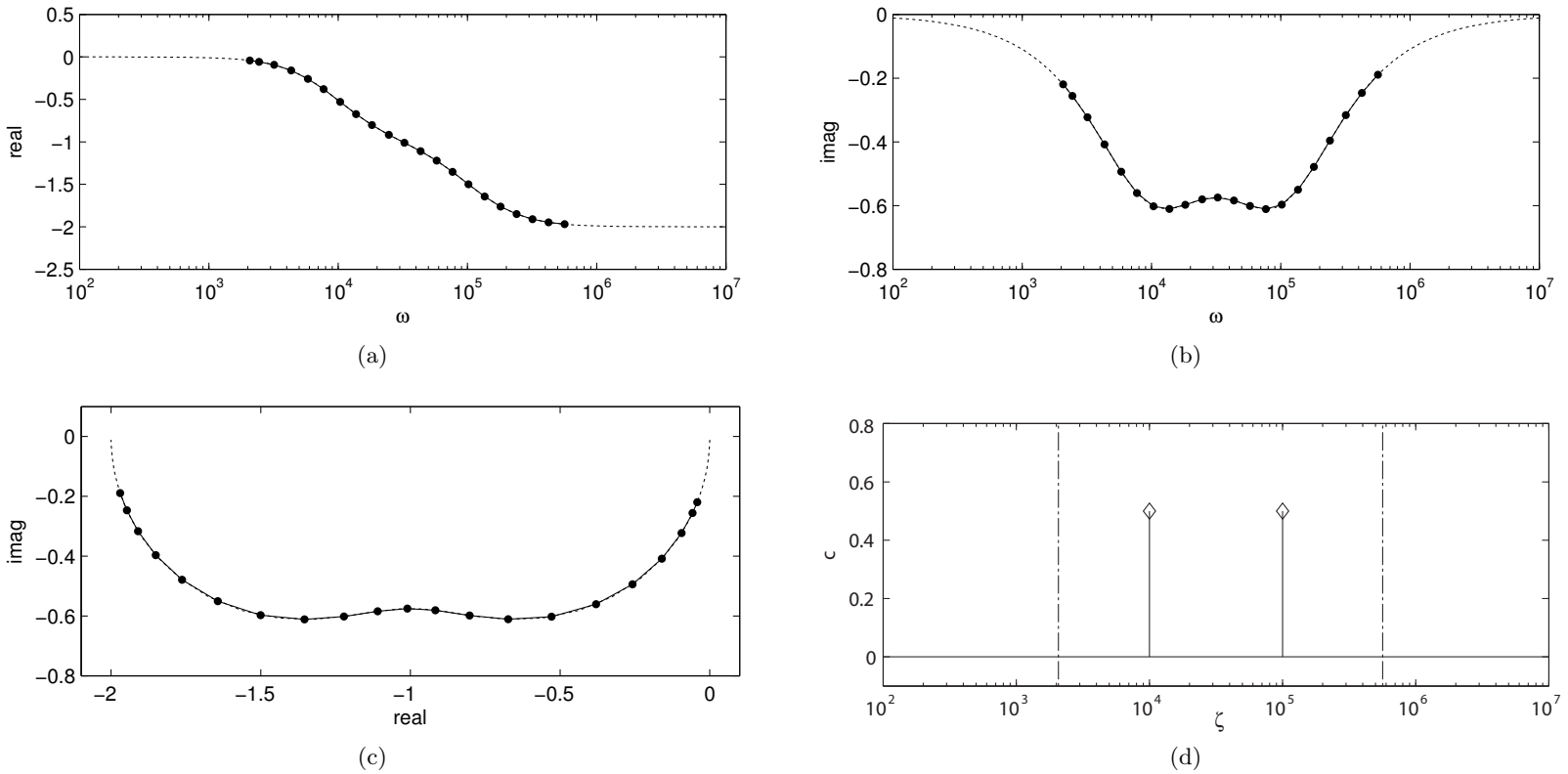

Figure 5: An example frequency response $H(\omega)$ sampled at 21 frequencies over 300-90 kHz. The dotted lines trace out the full range of the response. The solid lines trace out the measured response, i.e., the *observable* part for a band-limited EMI system. The solid circles indicate the samples measured at 21 distinct frequencies. (a) The real part and (b) the imaginary part of $H(\omega)$. (c) The complex response, parameterized by ω, plotted on an Argand diagram (complex plane). (d) The DSRF, where each relaxation is represented by a stem: the stem location is the relaxation frequency ζ_k and the stem height is the spectral amplitude c_k. The dash-dotted lines in (d) indicate the observable range.

A detailed derivation of the relation between (5) and (6), as well as other forms of the EMI model, can be found in Appendix A. The significance of choosing the particular form in (6) is that when this expression is linearized, as in the proposed method, the linearized model results in a matrix with uniform-norm columns. All columns having the same norm translates to an unbiased estimation of relaxation frequencies, as explained in Appendix A.

The measured EMI response is proportional to the product of the transmitted and received magnetic fields and the magnetic polarizability tensor of the target being measured by the EMI sensor (Appendix A). The magnetic polarizability tensor of several canonical targets can be calculated analytically, and these formulas show how the model parameters are related to the target's physical properties such as conductivity, permeability, shape, size, and orientation [12, 16, 19, 20].

One result of this analysis is that the relaxation frequencies ζ_k are invariant with respect to the target's position and orientation relative to the EMI sensor; only the spectral amplitudes change with orientation and position. Therefore, the DSRF, i.e., the ζ_k's and c_k's, are valuable for target discrimination, and even allow estimation of the target depth and orientation.

1.2.3 Existing Estimation Methods and Challenges

It is difficult to find a meaningful low-order model for an EMI frequency response. This is because the modeling process is an ill-posed problem – a small change in $H(\omega)$ can lead to a large change in the DSRF and different DSRFs can generate very similar or even identical responses. To illustrate the ill-posed nature of the modeling problem, shown in Fig. 6 are curve fits for the same target response using different spectral models. It is clear that all four models (spectra) generate a response very close to the measurement. However, the four spectra are actually very different, which illustrates the ill-posed nature of the inverse problem.

Several spectrum modeling techniques have been developed in the past few decades for both continuous and discrete spectra. For continuous spectra, modeling techniques such

as Tikhonov regularization [21], a nonparametric Bayesian approach [22], and a Monte-Carlo method [23] have been proposed. In particular, for the Cole-Cole model, existing methods include nonlinear iterative search, multifold least-squares estimation [24], and a gradient-lookup-table approach [7].

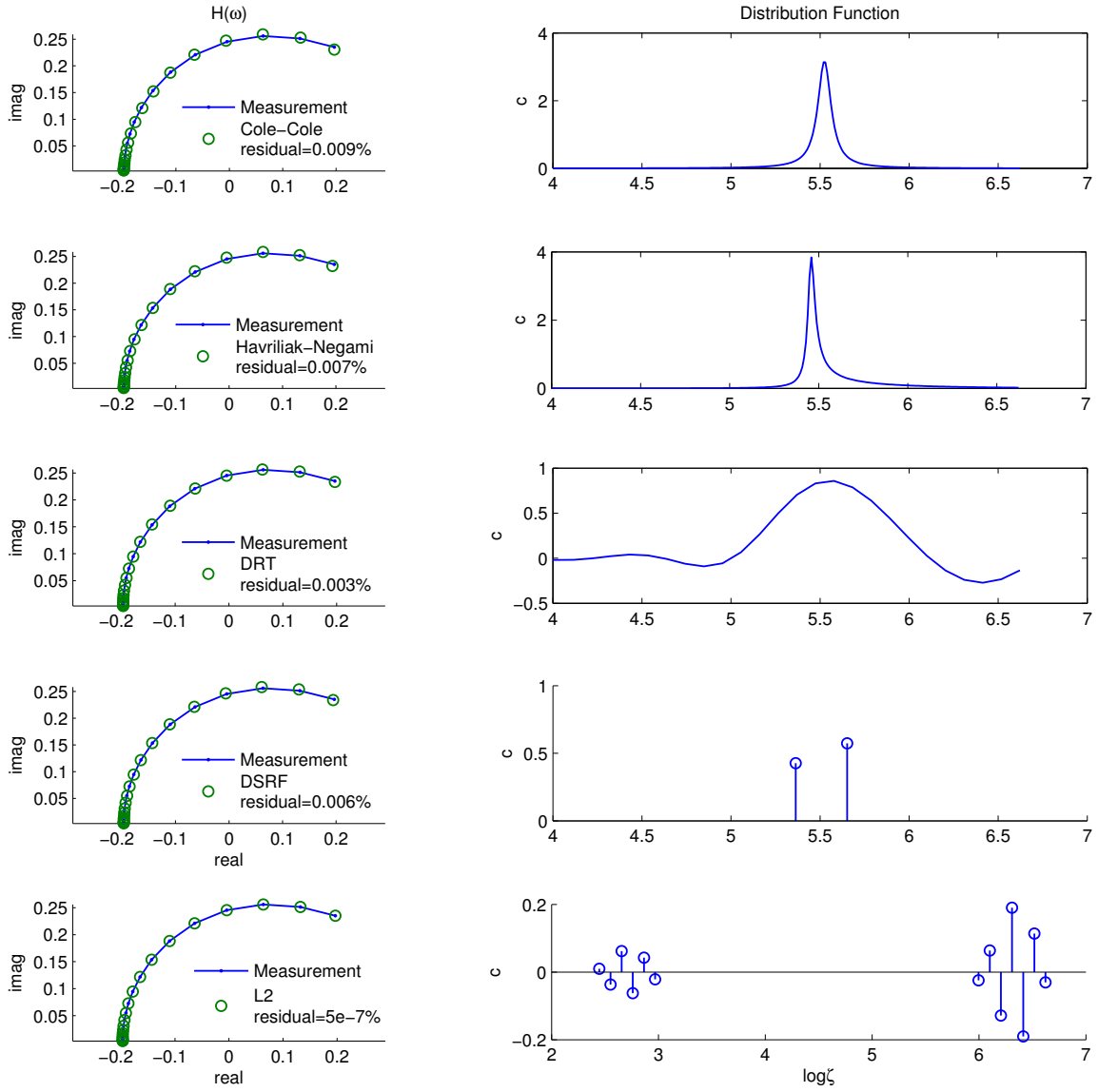

Figure 6: A target response (left) fitted to four different spectral models (right): Cole-Cole, Havriliak-Negami, a general DRT, and the DSRF, plus a standard least-squares fit. All models fit well but have very different distribution function $G(\tau)$. The DRT fit is obtained using the Tikhonov regularization.

In the discrete case, the modeling problem is equivalent to estimating the parameters of a sum of exponentials, which is a classic problem that arises in many fields. Several

notable estimation techniques include iterative nonlinear least-squares fitting, the matrix pencil method [25, 26], modified Prony's methods [27, 28] , and complex-curve fitting [29]. While the listed methods can be robust in other fields of science, in the case of EMI spectral modeling, a major challenge is that the poles are required to be *real-valued*, but most of these model-fitting methods can return complex poles. In addition, often these methods do not perform well when three or more relaxations are present. The goodness of estimation strongly depends on a good guess of the model order, and is also very sensitive to the initial guess for the model parameters.

Riggs et al. proposed a differential correction technique that returns only real relaxations, but the convergence still strongly depends on a good initial guess of the model order. When the guess of K is poor, the techniques fails to converge [5]. Estimating the unknown model order is the primary source of DSRF estimation difficulties.

In addition, as a consequence of the ill-posed problem, it is possible to converge well to a small residual, but obtain a fit that is, in fact, far from the correct solution. This is a common problem in the DSRF estimation to obtain "good fits but poor estimates," where the fitting residual can be minimized but the estimated DSRF is far off. The least-squares fit in Fig. 6 is a good example of this scenario, where the fitting residual is the smallest of all methods, but the estimated spectrum is noise-like with oscillatory, self-canceling relaxations.

The nonlinear relationship between $H(\omega)$ and ζ often requires a nonlinear iterative search to fit a response to the model. Some challenges of the search are that 1) the iteration can settle in local minima that are far from the correct solution, 2) the solution is sensitive to the initial guess, 3) the returned solution may be complex and lack physical meaning. It is possible that an estimate is only a good numerical fit, but has no physical significance [30].

Das and McFee provided a detailed examination of these challenges [30]. In summary, the challenges of DSRF estimation are 1) estimating the model order K, 2) not converging, 3) good numerical fit but poor estimate, and 4) returning complex estimates.

For these reasons, a simplified DSRF model with only one or two relaxations ($K = 1$ or 2) is often assumed [2, 31, 32]. The goal of this work is to accurately estimate parameters from the full model without constraining or assuming K.

1.2.4 Nonnegative Least-Squares (NNLSQ)

The initial effort in this research suggests a constrained linear method that robustly estimates the DSRFs without requiring prior knowledge of the model order and bypasses the nonlinear relationship between ζ and $H(\omega)$ [33, 34]. This is achieved through enumeration to obtain a linear problem, and then minimization of the squared error with a nonnegative constraint on the spectral amplitudes. The nonnegative constraint effectively reduces the size of the feasible solution set and eliminates oscillatory and nonphysical solutions. For example, the oscillatory least-squares solution in Fig. 6 is rejected by the nonnegative constraint.

While the NNLSQ algorithm performs well, the method presumes nonnegative spectra for the targets, i.e., $c_k \geq 0$. This assumption is, in fact, valid for most targets measured by our system [8, 33], but it is possible that some targets can have a spectrum with both positive and negative relaxations. A goal of this work is to develop a more general method that remove the nonnegative constraint.

1.2.5 Proposed Estimation Methods

To robustly estimate the DSRF without the nonnegative constraint but still require no prior knowledge of K and return only real-valued solutions, as in the NNLSQ, a *sparsity-promoting* DSRF estimation method is formulated. The sparsity approach follows the same sampling and linearization setup as in the NNLSQ, but replaces the nonnegative constraint with a sparsity-regularization term. The sparsity regularization is shown to deliver robust estimates without prior knowledge of K and returns only real-valued estimates.

This work further extends the DSRF estimation from the single-measurement case to estimation using multiple measurements. In the laboratory and the field, multiple measurements are often available for a given target of interest. Because different measurements from the same target share the same relaxation frequencies, this invariance property can be exploited to increase the estimation accuracy when multiple measurements are available.

The multiple measurements are utilized simultaneously by recasting the EMI estimation problem into the problem of multiple-measurement vectors (MMV) or jointly-sparse

vectors, where vectors sharing the same underlying structure are recovered. The model parameters can then be estimated through iterative reweighting algorithms. The proposed MMV method is tested against synthetic, laboratory, and field data, and is demonstrated to deliver accurate and stable estimates.

To account for the soil response in field measurements, the proposed DSRF estimation method is also extended to model the soil. A soil model is proposed based on the observation of a large number of soil responses, of which a subset is shown in Fig. 7. From the soil measurements, it is observed that the frequency responses follow a simple log-linear trend. That is,

$$H_{\text{soil}}(\omega) = \gamma \left(\ln \frac{\omega}{\omega_0} + j\frac{\pi}{2} \right), \tag{7}$$

where γ and ω_0 are model parameters. This model has a linear real part with respect to the log-frequency and has a constant imaginary part, which agrees with the observed soil measurements. Using this soil model, an augmented model is developed to consider both the DSRF and the soil simultaneously. It is shown that the augmented model can also be solved by the same proposed sparsity-promoting DSRF estimation method.

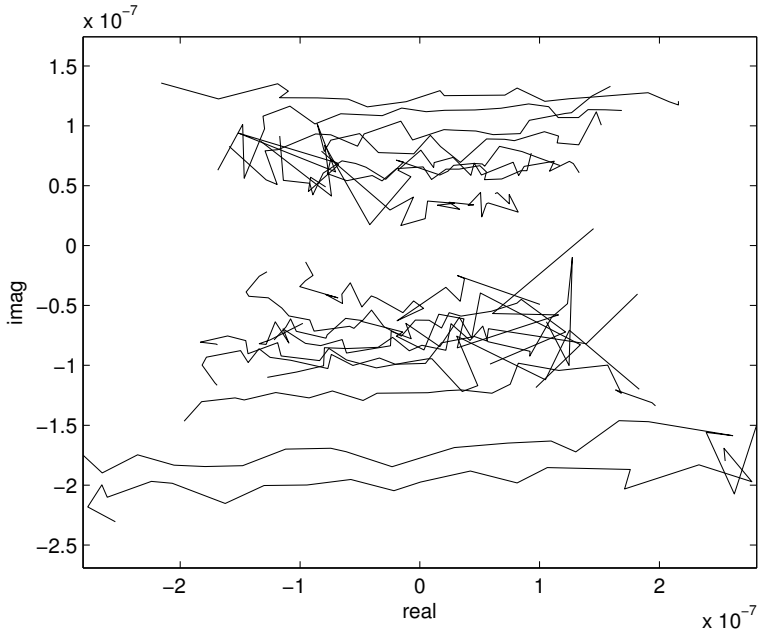

Figure 7: The frequency response of soil samples plotted on an Argand diagram. The real and imaginary part are shown in Fig. 21. The soil responses are collected at various locations in a testing field.

1.3 EMI-based Target Discrimination

1.3.1 Existing Discrimination Methods

Several EMI-based landmine discrimination techniques have been developed in the past decade. Both Bayesian and non-Bayesian classification as well as the continuous and discrete spectral model have been employed. Fails et al. [6] and Ramachandran et al. [7] both demonstrated success in detecting mines using the k-nearest-neighbor (kNN) algorithm based on the EMI model developed by Miller et al., i.e., the Cole-Cole model [14,15]. Using the Cole-Cole model, the target feature is a vector in $\mathbb{R}^4$. In [7], the modeling error is also included in the feature vector. The kNN labels an unknown target based on the closest targets in a training set.

Collins et al. [2] and Gao et al. [4] considered the likelihood ratio test applied to both time and frequency domain data. In [2], it is considered using only the most prominent relaxation, i.e., $K = 1$ in (5). In [4], a body-of-revolution model is considered.

Because the Cole-Cole spectrum and the most prominent relaxation are dependent on the orientation and location of a target, the above discrimination approaches can suffer from orientation variations of buried targets. The use of the DSRF takes into account this variation and is considered by Riggs et al. [5] and is also considered in this work.

Riggs et al. suggested identifying targets using a library of relaxation frequencies obtained from training targets [5]. This approach takes into account the orientation and position variation. The method uses a generalized likelihood ratio test, which results in a simple minimum least-squares-error decision rule. In a sense, this test is a kNN approach that considers only the closest neighbor.

1.3.2 Proposed Discrimination Method

In this work, a discrimination based on the estimated DSRF is considered. Figure 8 demonstrates the consistency of the estimated DSRF across instances of two different types of targets. For each target type, the EMI responses are collect from independent physical instances buried at different locations and depths. It is seen that instances from the same type share a consistent DSRF, while the two types clearly have distinct DSRFs. This observation

agrees with Baum's theory [12] and is the motivation of DSRF-based target discrimination.

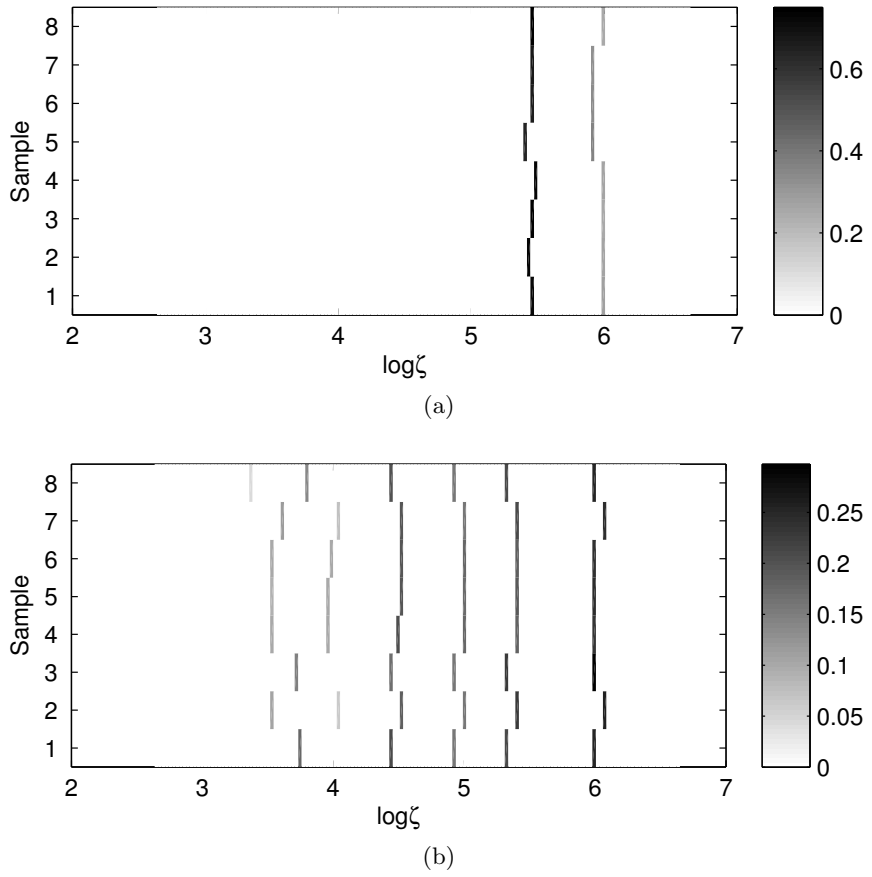

Figure 8: Estimated DSRF of landmines. The spectral amplitude c_k is represented by the intensity: the darker the gray, the larger the amplitude. (a) Seven low-metal content, non-magnetic, moderate EMI response antipersonnel mines. (b) Eight medium-metal content, magnetic, strong EMI response antipersonnel mines.

Two classifiers are examined for the proposed DSRF discrimination: kNN and the support vector machine (SVM). The kNN serves as a simple, proof-of-concept DSRF-based classification. The SVM is a more practical approach as the computation cost is lower for real-time applications.

To build a complete system for discriminating targets, a model-based soil prescreener is also developed to detect the presence of metallic objects. The prescreener is based on the soil model (7), and the prescreener turns out to be a simple least-squares minimizer, which can be computed efficiently. Combining the prescreener and the DSRF-based classifier, the proposed discrimination technique is shown to be competitive to existing methods.

1.4 Outline

The outline of this thesis is as follows: the DSRF estimation method based on a single measurement vector (SMV) utilizing sparsity is presented in Chapter II; this SMV method is extended to multiple measurements in Chapter III; the application of DSRF in target discrimination is demonstrated in Chapter IV, where the soil prescreener is also introduced; lastly, a conclusion is provided in Chapter V.

CHAPTER II

SPECTRUM ESTIMATION FROM SINGLE MEASUREMENTS

To robustly estimate the DSRF without the nonnegative constraint from a given EMI frequency response, a sparsity-promoting estimation method is developed. The estimation problem is first recast into a linear dictionary selection problem by densely sampling the relaxation frequency space. The linearized problem is then solved by minimizing the least-squares error *regularized* with sparsity. Nonconvex iterative sparsity-promoting optimization is employed to achieve robust performance. An interpolation is performed after the optimization step to address the issue if an actual relaxation frequency is split between two sampled relaxation frequencies [33].

The proposed sparsity-promoting DSRF estimation method is shown to be robust through tests on synthetic, laboratory, and field measurements. The method gives accurate estimates and requires no a priori knowledge of the model order and always returns real model parameters. An extension to the Earth Mover's Distance (EMD) [35] is devised to quantify the estimation accuracy. A simulation framework is also proposed to find the best regularization parameter used in the sparsity-promoting optimization.

The soil response is also considered when modeling the field measurements. In the field, a target response is always measured in the presence of soil, so the total response is composed of the target response, the soil response and the system noise. To take into account the effect of the soil, a soil model is proposed based on collected soil measurements. An augmented model is formulated to consider both the DSRF and soil concurrently. This augmented model is also solved by the sparsity-regularized least-squares.

The DSRF of many field targets from different types are examined using the proposed estimation method, and it is observed that targets of the same type have a similar DSRF. This observation affirms the idea to use DSRF as a signature for target discrimination, and this is explored in Chapter 4.

2.1 Method Formulation

When the target response is measured at N distinct frequencies, (6) can be written in matrix form:

$$\begin{bmatrix} H(\omega_1) \\ H(\omega_2) \\ \vdots \\ H(\omega_N) \end{bmatrix} = \underbrace{\begin{bmatrix} 1 & \frac{1-j\omega_1/\zeta_1}{1+j\omega_1/\zeta_1} & \frac{1-j\omega_1/\zeta_2}{1+j\omega_1/\zeta_2} & \cdots & \frac{1-j\omega_1/\zeta_K}{1+j\omega_1/\zeta_K} \\ 1 & \frac{1-j\omega_2/\zeta_1}{1+j\omega_2/\zeta_1} & \frac{1-j\omega_2/\zeta_2}{1+j\omega_2/\zeta_2} & \cdots & \frac{1-j\omega_2/\zeta_K}{1+j\omega_2/\zeta_K} \\ \vdots & \vdots & \vdots & \ddots & \vdots \\ 1 & \frac{1-j\omega_N/\zeta_1}{1+j\omega_N/\zeta_1} & \frac{1-j\omega_N/\zeta_2}{1+j\omega_N/\zeta_2} & \cdots & \frac{1-j\omega_N/\zeta_K}{1+j\omega_N/\zeta_K} \end{bmatrix}}_{\boldsymbol{Z}} \begin{bmatrix} c_0 \\ c_1 \\ c_2 \\ \vdots \\ c_K \end{bmatrix}$$

$$\boldsymbol{b} = \boldsymbol{Z}\boldsymbol{c}, \tag{8}$$

where $\omega_{\min} = \omega_1 < \omega_2 < \cdots < \omega_N = \omega_{\max}$, $\boldsymbol{b} \in \mathbb{C}^N$ is the observation vector, $\boldsymbol{c} \in \mathbb{R}^{K+1}$ the spectral amplitude vector augmented by the shift c_0, and $\boldsymbol{Z} \in \mathbb{C}^{N\times(K+1)}$ a matrix containing information about the relaxation frequencies $\boldsymbol{\zeta}$. The dimension of the matrix $\boldsymbol{Z}$ is dependent on the number of relaxations present in the spectrum, i.e., the model order. In the case of a simple thin wire circular loop, there is only one relaxation, so $\boldsymbol{Z}$ has two columns; the first column is always one to account for c_0.

2.1.1 Sampling The Relaxation Frequency Domain

To linearize the DSRF estimation problem, a large set of *sampled* relaxation frequencies $\{\tilde{\zeta}_m : m = 1 \dots M\}$, $M \gg K$, are generated by sampling within a range of possible or observable relaxation frequencies $[\tilde{\zeta}_{\min}, \tilde{\zeta}_{\max}]$. There are several ways to sample the relaxation frequency domain. The goal is to sample densely enough to ensure an actual relaxation frequency ζ_k will be close to some sampled relaxation frequencies $\tilde{\zeta}_m$.

Because the EMI data are measured at a wide range of frequencies, the observable relaxation frequencies also fall in a wide range of frequency. To sample in a high dynamic range, the relaxation frequencies are uniformly logarithmically spaced, i.e.,

$$\log \tilde{\zeta}_{m+1} = \log \tilde{\zeta}_m + \Delta, \tag{9}$$

where Δ is a fixed spacing between two $\tilde{\zeta}$ in log-space.

This sampling scheme turns out to be similar to the one proposed by Austin et al. [36], where the sampling is nonuniform based on the Fisher information:

$$\tilde{\zeta}_{m+1} = \tilde{\zeta}_m + \alpha \left[\sum_{n=1}^{N} \left(\frac{\omega_n}{\omega_n^2 + \tilde{\zeta}_m^2} \right)^2 \right]^{-\frac{1}{2}}. \tag{10}$$

The parameter α controls the number of samples given a frequency range. The two sampling schemes produce similar sample points (Fig. 9). Uniform sampling is used in this work because it is simpler.

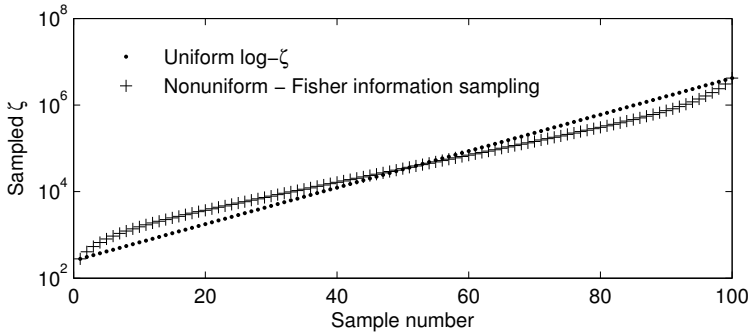

Figure 9: Samples generated from uniform log-ζ sampling and non-uniform sampling based on the Fisher information.

The expression (10) comes from [36]

$$\tilde{\zeta}_{m+1} = \tilde{\zeta}_m + \alpha \, \mathcal{I}(\boldsymbol{b}(\tilde{\zeta}_m))^{-1/2}, \tag{11}$$

where $\mathcal{I}$ is the Fisher information and $\boldsymbol{b}(\tilde{\zeta}_m) \in \mathbb{C}^N$ is the frequency response due to one relaxation frequency $\tilde{\zeta}_m$ measured at N frequencies. Assuming the measurement noise is Gaussian, then [36]

$$\mathcal{I}(\boldsymbol{b}(\tilde{\zeta})) \sim J_{\boldsymbol{b}}(\tilde{\zeta})^{\mathrm{H}} J_{\boldsymbol{b}}(\tilde{\zeta}), \tag{12}$$

where $J_{\boldsymbol{b}}(\tilde{\zeta})$ is the Jacobian of $\boldsymbol{b}(\tilde{\zeta})$ and the superscript $^{\mathrm{H}}$ denotes the Hermitian transpose. The Jacobian is

$$J_{\boldsymbol{b}}(\tilde{\zeta}) = \left[\frac{\partial}{\partial \tilde{\zeta}} b(\tilde{\zeta};\, \omega_1) \; \frac{\partial}{\partial \tilde{\zeta}} b(\tilde{\zeta};\, \omega_2) \; \ldots \; \frac{\partial}{\partial \tilde{\zeta}} b(\tilde{\zeta};\, \omega_N) \right]^T, \tag{13}$$

where

$$\begin{aligned} \frac{\partial}{\partial \tilde{\zeta}} b(\tilde{\zeta};\, \omega_n) &= \frac{\partial}{\partial \tilde{\zeta}} \frac{1 - j\omega_n/\tilde{\zeta}}{1 + j\omega_n/\tilde{\zeta}} \\ &= \frac{2j\omega_n}{\left(\tilde{\zeta} + j\omega_n\right)^2} \end{aligned} \tag{14}$$

With some simple algebra, it can be shown that

$$J_{\boldsymbol{b}}(\tilde{\zeta}_m)^{\mathrm{H}} J_{\boldsymbol{b}}(\tilde{\zeta}_m) = \sum_{n=1} \left| \frac{2j\omega_n}{\left(\tilde{\zeta} + j\omega_n\right)^2} \right|^2$$
$$= \sum_{n=1}^{N} 4 \left(\frac{\omega_n}{\omega_n^2 + \tilde{\zeta}_m^2} \right)^2 . \tag{15}$$

Substituting (15) into (11), (10) is obtained.

2.1.2 Linearizing The Problem

Using the sampled relaxation frequencies, (8) can be rewritten as

$$\underbrace{\begin{bmatrix} H(\omega_1) \\ H(\omega_2) \\ \vdots \\ H(\omega_N) \end{bmatrix}}_{\boldsymbol{b}} = \underbrace{\begin{bmatrix} 1 & \frac{1-j\omega_1/\tilde{\zeta}_1}{1+j\omega_1/\tilde{\zeta}_1} & \frac{1-j\omega_1/\tilde{\zeta}_2}{1+j\omega_1/\tilde{\zeta}_2} & \cdots & \frac{1-j\omega_1/\tilde{\zeta}_M}{1+j\omega_1/\tilde{\zeta}_M} \\ 1 & \frac{1-j\omega_2/\tilde{\zeta}_1}{1+j\omega_2/\tilde{\zeta}_1} & \frac{1-j\omega_2/\tilde{\zeta}_2}{1+j\omega_2/\tilde{\zeta}_2} & \cdots & \frac{1-j\omega_2/\tilde{\zeta}_M}{1+j\omega_2/\tilde{\zeta}_M} \\ \vdots & \vdots & \vdots & \ddots & \vdots \\ 1 & \frac{1-j\omega_N/\tilde{\zeta}_1}{1+j\omega_N/\tilde{\zeta}_1} & \frac{1-j\omega_N/\tilde{\zeta}_2}{1+j\omega_N/\tilde{\zeta}_2} & \cdots & \frac{1-j\omega_N/\tilde{\zeta}_M}{1+j\omega_N/\tilde{\zeta}_M} \end{bmatrix}}_{\boldsymbol{A}} \underbrace{\begin{bmatrix} \tilde{c}_0 \\ \tilde{c}_1 \\ \tilde{c}_2 \\ \vdots \\ \tilde{c}_M \end{bmatrix}}_{\boldsymbol{x}} + \boldsymbol{e}$$

or

$$\boldsymbol{b} = \boldsymbol{A}\boldsymbol{x} + \boldsymbol{e}, \tag{16}$$

where $\tilde{c}_m \in \mathbb{R}$ are the spectral amplitude estimates corresponding to each $\tilde{\zeta}_m$, $\boldsymbol{A} \in \mathbb{C}^{N\times(M+1)}$ the overcomplete dictionary, and $\boldsymbol{e} \in \mathbb{C}^N$ the modeling error. The solution vector $\boldsymbol{x} \in \mathbb{R}^{M+1}$ is a weighted selection vector containing the shift estimator $\tilde{c}_0$ followed by the spectral amplitude estimators. The matrices $\boldsymbol{Z}$ and $\boldsymbol{A}$ differ in that $\boldsymbol{Z}$ is constructed with the actual relaxation frequencies while $\boldsymbol{A}$ is the dictionary constructed with sampled relaxation frequencies.

Because $M \gg K$, a good solution for $\boldsymbol{x}$ will have many zero elements, i.e., $\boldsymbol{x}$ will be *sparse*. The intent is to use $\boldsymbol{x}$ to pick out the $\tilde{\zeta}_m$ that are close to the actual relaxation frequencies ζ_k. By assigning a zero value to $\tilde{c}_m$ that correspond to the $\tilde{\zeta}_m$ that are not near any ζ_k, the corresponding $\tilde{\zeta}_m$ can be made ineffective. When the zeros are properly assigned and c_k properly assigned to $\tilde{c}_m$, (8) and (16) becomes almost identical and the error is small. In this case, $\boldsymbol{x}$ is sparse, having only a few nonzero entries.

2.1.3 Sparsity-promoting Minimization

While it is true that a good solution for $\boldsymbol{x}$ produces a small error in (16), directly minimizing the error often yields solutions far from the correct answer. The challenge in obtaining the correct $\boldsymbol{x}$ is that M is much greater than N, so the system in (16) is underdetermined and there is not an unique $\boldsymbol{x}$ to minimize the error:

$$\arg\min_{\boldsymbol{x}} ||\boldsymbol{b} - \boldsymbol{A}\boldsymbol{x}||_2^2. \tag{17}$$

Any vector in the null space of $\boldsymbol{A}$ can be added to $\boldsymbol{x}$ without changing the error. There are many ways to select a least-squares (LSQ) solution. The Moore-Penrose pseudoinverse picks the LSQ solution that has the smallest ℓ_2 norm. One can also compute a LSQ solution with the fewest nonzero components. However, neither of these LSQ solutions produces the correct spectrum, as demonstrated in Fig. 6. One reason is that the error in (16) will not be zero due to modeling error because it is unlikely that all ζ_k overlap with some $\tilde{\zeta}_m$. Details about existing techniques and the difficulties of solving such a system can be found in [30, 37, 38].

Knowing that the solution vector $\boldsymbol{x}$ should be sparse, the LSQ optimization (17) can be *regularized* to promote sparsity. Sparsity-regularized least squares turn out to be an effective way to obtain good solutions for $\boldsymbol{x}$.

There are several ways to perform sparsity-regularized least squares, including basis pursuit (ℓ_1-minimization), matching pursuit, iteratively reweighted ℓ_1-minimization (IRL1), and iteratively reweighted least squares (IRLS or FOCUSS). It has been shown that the latter two nonconvex iterative reweighted algorithms, IRL1 and FOCUSS, produce solutions that are more sparse compared to the non-reweighted ones [39]. In addition, IRL1 and FOCUSS are equivalent under certain circumstances. To simplify the discussion, only IRL1 is considered here. The relationship between IRL1 and FOCUSS is discussed in detail in Chapter 3, where multiple measurements are considered.

To estimate the DSRF using sparsity-regularized least squares, the following optimization problem is solved:

$$\arg\min_{\boldsymbol{x}} ||\boldsymbol{b'} - \boldsymbol{A'}\boldsymbol{x}||_2^2 + \lambda||\boldsymbol{x}||_p^p \quad , 0 \leq p \leq 1 \tag{18}$$

$$\text{where } \boldsymbol{A}' = \begin{bmatrix} \mathfrak{Re}(\boldsymbol{A}) \\ \mathfrak{Im}(\boldsymbol{A}) \end{bmatrix}, \boldsymbol{b}' = \begin{bmatrix} \mathfrak{Re}(\boldsymbol{b}) \\ \mathfrak{Im}(\boldsymbol{b}) \end{bmatrix},$$

and λ is the regularization parameter. Separating the real and imaginary parts in $\boldsymbol{A}$ makes the whole system real. Ideally, in the optimal $\boldsymbol{x}$, only those $\tilde{c}_m$ with corresponding $\tilde{\zeta}_m$ that are near a true ζ_k will be nonzero, and they will take on the correct spectral amplitudes c_k. It follows that a DSRF can then be deduced from the nonzero estimated $\tilde{c}_m$ and their corresponding $\tilde{\zeta}_m$.

The ℓ_p-regularized least squares solution for $p < 1$ can be approximated by the iteratively reweighted ℓ_1 algorithm proposed by Candès *et al.* [40]. The weights are updated as suggested in [39], and the ϵ-regularization technique is adopted from the same paper. In summary, (18) is approximated by (see also [41]):

Algorithm 1: Approximated ℓ_p-regularized least squares

Input: $\boldsymbol{A}'$, $\boldsymbol{b}'$, p, λ, $\boldsymbol{x}^0$
1 $\boldsymbol{x}^n \leftarrow \boldsymbol{x}^0$
2 **for** $k \leftarrow 0$ **to** -8 **step** -1 **do**
3 $\epsilon \leftarrow 10^k$
4 **repeat**
5 $\boldsymbol{x}^{n-1} \leftarrow \boldsymbol{x}^n$
6 $w_i^n \leftarrow (|\tilde{c}_i^{n-1}| + \epsilon)^{p-1}$
7 $\boldsymbol{x}^n \leftarrow \arg\min ||\boldsymbol{b}' - \boldsymbol{A}'\boldsymbol{x}||_2^2 + \lambda \sum_{i=1}^{M+1} w_i^n |\tilde{c}_i|$
8 **until** $||\boldsymbol{x}^n - \boldsymbol{x}^{n-1}||_2 < \sqrt{\epsilon}/100$
9 **return** $\boldsymbol{x}^n$

The ℓ_1 minimization problem in step 7 is solved by `l1_ls`, a MATLAB optimizer proposed by Kim *et al.* [42]. It has been observed that normalizing the input data $\boldsymbol{b}$, as well as the columns of $\boldsymbol{A}'$, to have an uniform ℓ_2 norm increases the accuracy of estimation. This is why the EMI model in the form in (6) is chosen over other forms – it produces a uniform-column-norm dictionary; details are provided in Appendix A. While it is often suggested to initialize $\boldsymbol{x}^0$ using the least-squares solution [39], it is observed that setting entries of $\boldsymbol{x}^0$ to all ones also seems to be effective and converges faster. The nonzero entries of $\boldsymbol{x}$ selected by (18) along with the corresponding $\tilde{\zeta}_m$ are the relaxations needed in the estimated DSRF, $\hat{S} = \{(\hat{\zeta}_k, \hat{c}_k) : k = 1 \ldots \hat{K}\}$.

2.2 Estimation Results With Synthetic Data

The proposed estimation method is tested against synthetic and laboratory data to show its functionality, accuracy, and stability. The hardware system used in laboratory and field measurements is a wideband EMI sensor operating at 21 frequencies approximately logarithmically distributed over the range 300 Hz–90 kHz, which is a span of 2.5 decades [8]. The synthetic data is generated in accordance with the hardware specification.

The range of ζ for estimation is chosen such that $\log(\tilde{\zeta}_{\min})$ and $\log(\tilde{\zeta}_{\max})$ are 2.45 and 6.62, respectively, i.e., a span of 4.17 decades. All estimations are performed with $M = 100$, and all presented spectra are normalized such that $\sum |c_i| = 1$. Spectral amplitudes less than 10^{-5} are not displayed. All frequency responses are normalized such that $\|\boldsymbol{b}\|_2 = 1$. Unless specified, $p = 0.5$ is chosen as a representative case. In assessing the signal strength, the signal-to-noise ratio (SNR) is used. The signal power is computed by $\sum_{i=1}^{N} |H(\omega_i)|^2/N$. The noise power in synthesized data is equal to the variance of the noise.

The regularization parameter λ is chosen based on the method described in Section 2.5. Results presented in this section may achieve higher accuracy with a more sophisticated λ selection rule. The purpose of this section is to demonstrate the usability of the proposed algorithm using a simple λ selection rule.

Notation: ζ and c are the true/theoretical relaxation frequencies and spectral amplitudes; $\hat{\zeta}$ and $\hat{c}$ are the estimates.

2.2.1 Dissimilarity Measure Between Two DSRFs

To evaluate the goodness of estimation, it is necessary to define a measure to quantify the similarity between two DSRFs. It is not straight forward, however, to compare two sparse spectra because 1) the number of relaxations can be different and 2) small misalignments of two relaxation frequencies often occur. For these two reasons, the standard Euclidean distance is not an ideal distance measure between two DSRFs. For example, in Fig. 10(a) the estimate and the correct solution are very similar but with a large Euclidean distance of 0.71 units of c because of one small misalignment in the ζ axis. This issue is further complicated when the number of relaxations in two spectra are not the same. If two DSRFs

S and $\hat{S}$ have the same model order, the Euclidean distance between the two is

$$\left[\sum_{k=1}^{\hat{K}} (c_k - \hat{c_k})^2\right]^{-2}. \tag{19}$$

The Earth Mover's Distance (EMD) is a measure that takes into account misalignments and mismatching model orders [35, 43]. The EMD measures how much "work" it takes to morph one spectrum into another. The metaphor is that one spectrum represents piles of earth with volume $\hat{c_k}$ located at the associated $\hat{\zeta_k}$. The other spectrum represents holes in the ground with capacity c_k located at ζ_k. The EMD is proportional to the least amount of work needed to move as much earth as possible into the holes. Work is defined to be the amount of earth moved times the distance traveled. Intuitively, the distance would simply be the difference between $\hat{\zeta_k}$ and ζ_k in log-space. This is true when c_k and $\hat{c_k}$ have the same sign. To accommodate opposite signs, the distance function d_{ij} between two relaxations (ζ_i, c_i) and ($\hat{\zeta_j}$, $\hat{c}_j$) is defined to be

$$d_{ij} = \begin{cases} |\log \zeta_i - \log \hat{\zeta_j}| & , c_i \hat{c}_j \geq 0 \\ 1 + |\log \zeta_i - \log \hat{\zeta_j}| & , c_i \hat{c}_j < 0 \end{cases},$$

which penalizes relaxations with different signs by adding a constant to the distance. This constant can be replaced by other quantities, such as $\exp(-\alpha|\log \zeta_i - \log \hat{\zeta_j}|)$, where α determines the decaying rate. Spectra are made nonnegative and normalized prior to the EMD computation. The EMD is measured in decades because it is examined in log-ζ space.

The EMD compares two spectra as a whole, so the effect of very small amplitude relaxations is tiny in the EMD, and neglecting these small components amounts to assuming they are near the noise level of the measured frequency response. See Appendix C for details about the EMD. For simplicity, it is sufficient to say that EMD quantifies the similarity between two DSRFs.

Some examples of the EMD are shown in Fig. 10. It is observed that the EMD reflects the similarity between two DSRFs. On the other hand, the ℓ_2 Euclidean distance returns a similar number regardless of how similar two DSRFs are to each other.

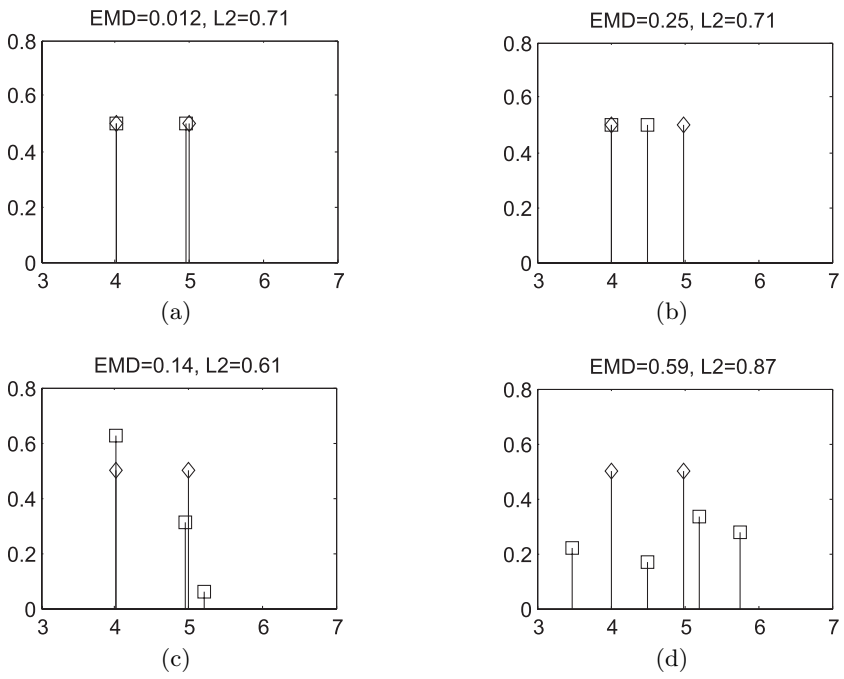

Figure 10: Examples of the ℓ_2 Euclidean distance and the EMD between two DSRFs, labeled by the diamonds and the squares. (a) The two spectra are very similar but the ℓ_2 distance is large while the EMD is small. (b) The spectra are less similar compared to (a), which is reflected in the higher EMD, but the ℓ_2 distance remains the same. (c) Spectra with different model orders. (d) Two very different spectra.

2.2.2 Synthetic Six-relaxation DSRF

The proposed sparsity-promoting estimation method is tested on a six-relaxation DSRF synthesized at 70 dB SNR with additive white Gaussian noise (Fig. 11). This is a case that cannot be handled by traditional nonlinear parameter optimization [30], or the nonnegative linear method [33]. The actual DSRF and the frequency response, along with their fits, are shown in Fig. 11. All six relaxation frequencies are recovered by solving (18) with $p = 0.5$. The estimation is nearly perfect, because the estimated model parameters are real, and the deviation from the true answer is small; the EMD is 0.09 decade, for $p = 0.5$.

When this spectrum is estimated with $p = 1$ using `l1_ls` many extra relaxations are introduced by the fitting process; for $p = 1$, the EMD is 0.10 decades. Real targets are not likely to have a spectrum with so many small relaxations around a strong relaxation. In fact, Baum argues that physical relaxation frequencies are discrete [12]. However, the several small relaxations when using $p = 1$ give a denser distribution of relaxations, resembling a

continuous spectrum. In this sense, $p < 1$ gives a sparser solution that more accurately resembles a physical spectrum even though this may not always be reflected in the EMD measure. The fits of the frequency response is also displayed in Fig. 11(a), and it is seen that both $p = 0.5$ and $p = 1$ produce a good fit to the frequency response.

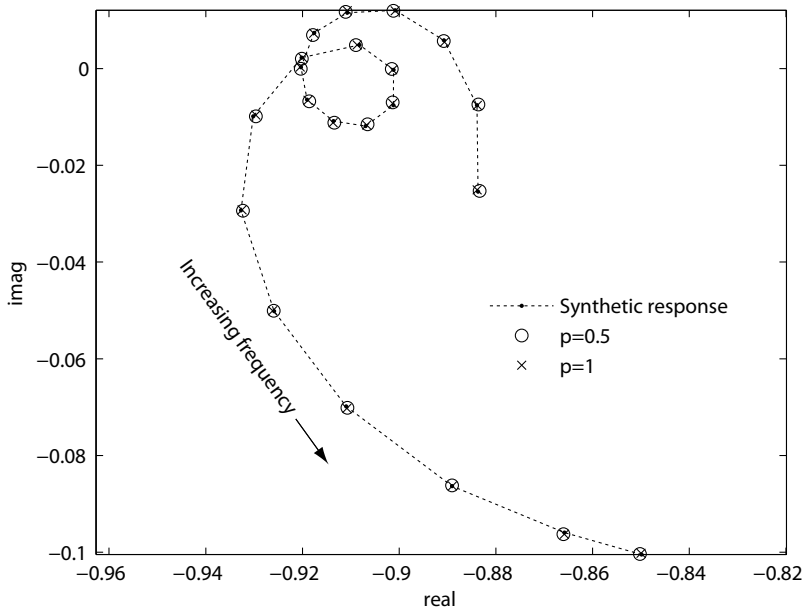

(a)

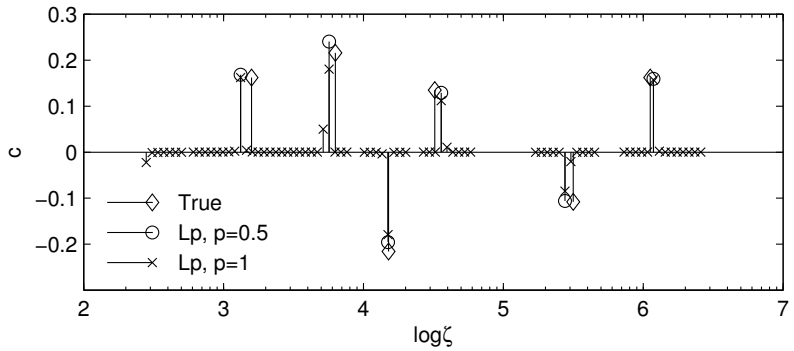

(b)

Figure 11: Estimation of a synthetic six-relaxation DSRF with $p = 0.5$ and $p = 1$. (a) The synthesized frequency response and two model fits. (b) The actual DSRF and its estimates.

2.2.3 Signal-to-Noise Ratio

To see how the proposed method performs in noise, a Monte Carlo simulation of the goodness of estimation versus SNR is performed. For each SNR, 100 samples are generated, and each sample has a DSRF with four relaxations. The relaxation frequencies are uniformly

distributed at random over $[\zeta_{\min}, \zeta_{\max}]$, and the spectral amplitudes are generated similarly over $[-1, 1]$. For each DSRF estimate, the goodness of estimation is measured by the EMD between the estimate and truth.

The simulation result, in Fig. 12, shows the robustness of the estimation method at different SNRs. The EMD between the estimate and the truth increases as the SNR decreases. This suggests that the proposed method is usable in a range of SNR where the EMD is below some threshold. Visually, spectra with an EMD below 0.1 are considered similar, those with an EMD above 0.2 exhibit noticeable differences, but may still resemble each other. In our laboratory measurements, a typical SNR for loop targets is 70 dB.

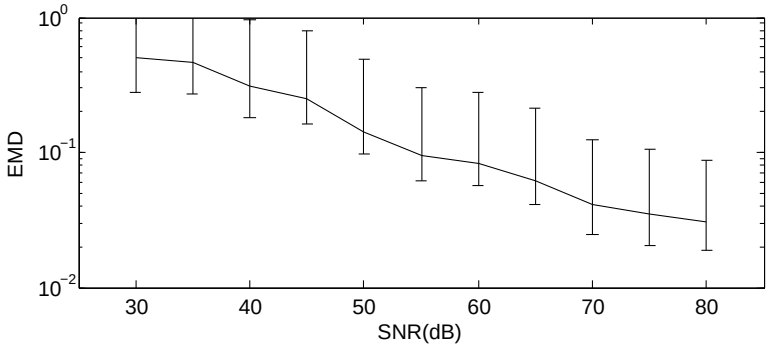

Figure 12: Monte Carlo simulation of goodness of estimation (EMD) vs. SNR performed using a four-relaxation DSRF. The error bars indicate the range of EMD between the 10th and 90th percentiles. Sample size is 100 per SNR.

2.3 Laboratory Data

To verify the functionality of the algorithm, the proposed method is applied to the laboratory measurement of a target where the theoretical DSRF is known [44]. The target consists of three mutually-orthogonal copper loops. The loop diameters and thicknesses are 3/20, 4/30, and 5/36, respectively in cm/AWG[1]. The orientation and position relative to the EMI sensor are chosen to demonstrate the positive and negative spectral amplitudes. The measured frequency response of this configuration is shown in Fig. 13(a), and the SNR is about 38 dB. The estimated DSRF is displayed in Fig. 13(b). The estimate and theory agree well, and the EMD between the theoretical and estimated DSRF is 0.10 decades.

[1] American Wire Gauge

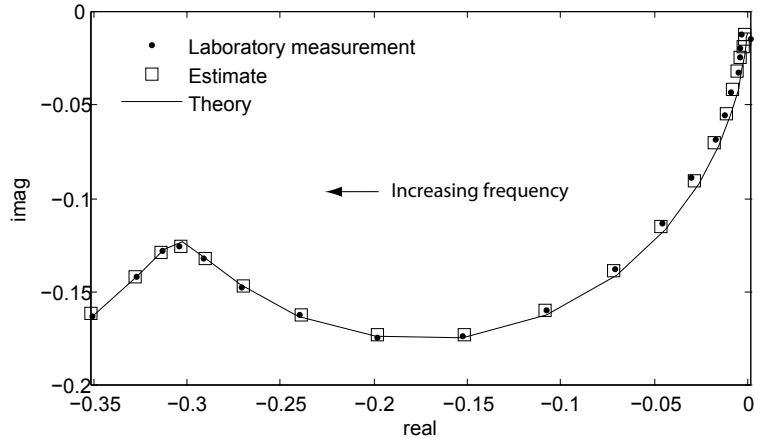

(a)

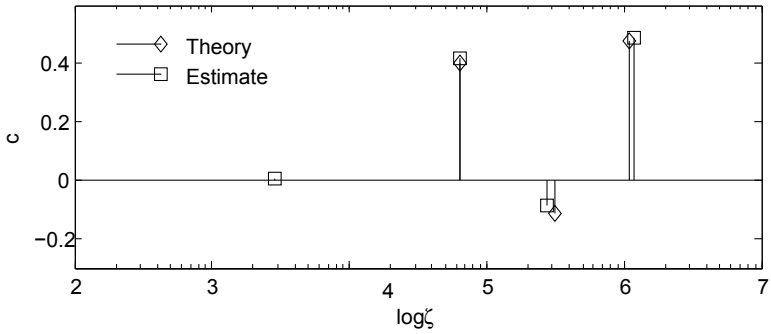

(b)

Figure 13: (a) Measured frequency response of three mutually orthogonal loops, its fit, and the theoretical response. (b) Theoretical and estimated DSRFs of the response in (a).

Next, changes in the DSRF as the target moves relative to the EMI sensor are studied. The same target configured at a fixed orientation is displaced at different positions along a horizontal axis, denoted x. The vertical distance between the target and sensor is 6 cm. The EMI sensor is located at $x = 0$. Samples of the measured target responses are shown in Fig. 14(a); their corresponding spectra are in Fig. 14(b). Theoretical results are also shown. Overall, the theory and measurement agree. The disagreement at $x = -0.5$ may be because of approximations in the model and/or inaccuracies in the positions measured in the experiment.

As expected from the theory, while the frequency response changes dramatically as the target moves along the x axis, the corresponding change in the spectral domain only occurs in the spectral amplitudes. The three dominant relaxation frequencies remain unchanged. The proposed method successfully estimates the spectra that agree with this phenomenon.

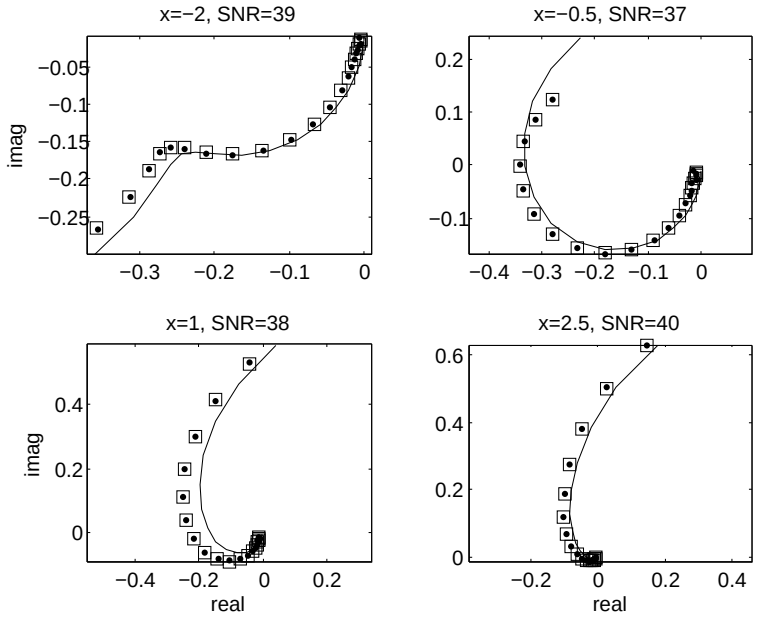

(a)

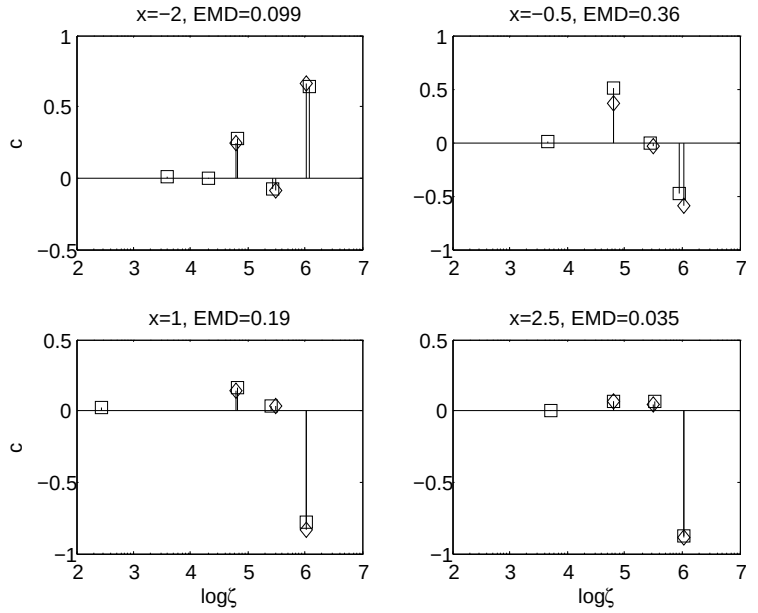

(b)

Figure 14: The plots share the same annotation as Fig. 13. (a) Frequency responses of the three mutually orthogonal copper loops at different locations. (b) Theoretical and estimated DSRFs of the corresponding responses in (a). The SNR is measured in dB, x positions in cm, and EMD in decades.

All three relaxation frequencies are consistently estimated. The extra relaxations all have small amplitudes that can be safely ignored. This invariant property of the relaxation frequencies makes the DSRF valuable especially for target discrimination.

2.4 Field Data

The proposed method is applied to a data set, acquired during a field test, which contains 62 types of targets, including 26 types of landmines as well as various types of metallic and nonmetallic clutter. The testing field is divided into 11 lanes, each lane containing 20 grid cells, so there are 220 grid cells total. About 145 measurements are collected per grid.

The primary objective of estimating the DSRF from field measurements is to verify the functionality of the proposed method for realistic field data, and to study the *consistency* of DSRFs from targets of the same type. Because targets of the same type should have the same physical composition, their DSRFs are expected to be the same. It is demonstrated in the following section that targets from the same type do have very similar estimated DSRFs. Targets of different types are also observed to have very different DSRFs, in general.

The field measurements are collected by an EMI measurement cart, shown in Fig. 1 in Chapter 1. The EMI acquisition hardware used has the same specification as described in Section 2.2, and details are found in [8]. As the cart is pushed over a target, the frequency response of the target is collected sequentially, as illustrated in Fig. 2. A segment of collected responses (magnitude only) at 21 frequencies is shown in Fig. 15. Although multiple measurements are available per target, in this chapter only one measurement is considered per target. The one measurement selected has the largest response magnitude in the grid cell. In Fig. 15, this corresponds to the peak of the strongest lobe in a grid cell, which usually occurs when the EMI sensor is directly above or nearly above the target. The multiple lobes seen in Fig. 15 are a result of filtering the measurements [8]. For field measurements, the SNR is estimated by the signal-to-background ratio, where the background is considered to be primarily due to the soil. The field measurements used in this work have a background signal power of about $-130\,\mathrm{dB}$, as shown in grid 70 in Fig. 15.

In field measurements, the soil response is also measured in addition to the target response and noise. In Section 2.4.2, the frequency response of soil and its effect on the DSRF are examined. An "augmented dictionary" that includes the DSRF model *and* a soil model is proposed to simultaneously model the target response and the soil response. From preliminary results, it is observed that including the soil model in the DSRF estimation

process produces estimates very similar to those obtained when ignoring the soil response. This observation suggests that it is safe to ignore the soil response when estimating the DSRF of targets from field measurements. However, more simulations and tests should be done to study the effect of soil on target responses. The results presented in the following section are obtained ignoring the effect of soil.

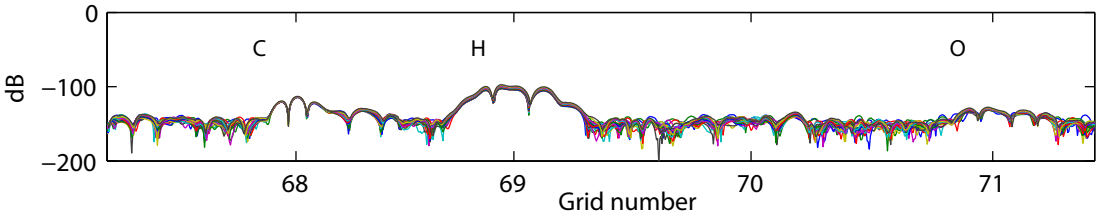

Figure 15: A short segment of the field measurements acquired by the EMI cart. Shown are the magnitude of the frequency responses; each curve represents one frequency. The letters denote the type of target buried in the grid cell.

2.4.1 Estimating the DSRF of Various Targets

Several types of landmines are examined to study the performance of the proposed method when applied to field measurements and to investigate the consistency of DSRF from landmines of the same type. Each type of landmine has multiple instances buried at different depths in different grid cells. The buried depth affects the strength of the measured response. One sample of the measurements is used per instance, and the DSRF of each sample is estimated and then plotted together with others of the same type. The spectral amplitudes are represented by the color intensity. The DC magnetization of targets is also examined at the end of this section.

Eight Type-A mines, a low-metal content, nonmagnetic, and moderate EMI response antipersonnel mine, are examined. The SNR ranges from about 45 to 60 dB. The frequency response of the eight instances are shown in Fig. 16(a) and the estimated DSRFs in Fig. 16(b). All eight Type-A mines exhibit consistency in the relaxation frequencies and the spectral amplitudes. The DSRFs are very similar, and the average EMD between pairs of mines is 0.052 decades. The estimated DSRFs also generate good curve fits in the frequency domain, shown in Fig. 16(a).

Eight Type-B mines, a medium-metal content, magnetic, strong EMI response antipersonnel mine, are examined. The SNR ranges from about 55 to 70 dB. The frequency responses are shown in Fig. 16(c) and the estimated DSRFs in Fig. 16(d). The samples exhibit consistency in the relaxation frequencies and the spectral amplitudes. Samples #1 and #3 differ from other samples slightly near 3.7 decades where two relaxations are combined into one, but the difference is small. The average EMD between pairs of mines is 0.1 decades. The estimated DSRFs generate good curve fits in the frequency domain.

To demonstrate the advantage of the sparsity-promoting DSRF estimation method over the NNLSQ, four samples of the Type-K mine, a medium-metal content, magnetic, moderate EMI response antipersonnel mine, are fitted using both methods. The SNR ranges from about 52 to 60 dB. The frequency responses and the estimated DSRFs are shown in Fig. 17. From the frequency response plots, it is observed that sample #4 has a relaxation with a *negative* c_k because the real part of the response is *non-monotonic*. This property was discovered during an early phase of this research [34] and is used as the basis for using the NNLSQ because most filtered field target responses exhibit a monotonic real part [33]. However, sample #4 does not follow this trend and has a negative component. The NNLSQ method returns a DSRF estimate for #4 that is quite different from other samples, and the fit in the frequency response is also not very good. The low frequency part, where the real part is non-monotonic, is not fitted by NNLSQ. On the other hand, the sparsity-promoting method property recovers the negative relaxations in #4 and the estimated DSRF agrees with other samples.

More examples of estimated DSRFs from field targets are shown in Fig. 18 and Fig. 19. Here is a list of description for the example targets:

- Type-H and -I: low-metal content, magnetic, moderate response antitank mines.
- Type-V and -W: low-metal content, magnetic, moderate response antipersonnel mines.
- Type-C: a low-metal content, magnetic, weak response antipersonnel mine.
- Type-D: a low-metal content, slightly magnetic, strong response antipersonnel mine.
- Type-E: a low-metal content, magnetic, weak response antipersonnel mine.
- Type-L: a medium-metal content, magnetic, strong response antipersonnel mine.

Consistent DSRFs within a target type are generally observed. Deviations do occur, but mostly in relaxations with a small spectral amplitude, e.g., Type-E mines in Fig. 19(c). A small spectral amplitude contributes only a small amount to the EMD. Another observation is the combining or splitting of relaxations, such as the Type-W mines in Fig. 18(d). Often the combining of relaxations happens at lower SNRs, where there is not enough resolution to separate the two relaxations. This is reflected in the λ selection, where a lower SNR gives a higher λ, encouraging a sparser solution, as discussed in Section 2.5. Nevertheless, the impact of combining and splitting is inherently reduced in the EMD. Targets with a weak EMI response, such as Type-C mines in Fig. 19(a), are also observed to have more variations in the estimated DSRF and higher EMDs.

On the other hand, targets of different types tend to have very distinct DSRFs. For example, when comparing Type-A and Type-B mines, Type-A mines only have two relaxations and Type-B mines have six relaxations. Even if the number of relaxations are the same, the spectral amplitudes can be different. For example, Type-H and Type-V mines both have four relaxations but Type-H has its stronger relaxations around 6 decades, whereas Type-V has its strongest relaxation near 5 decades. There are mines from the same family that do have similar DSRFs, such as Type-V and Type-W mines. The characteristics of each target type observed in the DSRF suggest a DSRF-based target discrimination, which is discussed in Chapter 4.

Estimates of $H(0) = \sum_{k=0} \hat{c_k}$ for several mine types are shown normalized in Fig. 20. This constant is due to the DC magnetization of the target. For example, Type-A mines are nonmagnetic and the estimated $H(0)$ is close to zero, as shown in Fig. 20(a). In contrast, Type-V and -W mines are strongly magnetic and have a relatively large $H(0)$. Type-I and -B are magnetic but have a weaker magnetic response than Type-V and -W. Shown in Fig. 20(b) are some cases with poor $H(0)$ estimates. For example, sample #3 of the Type-H mine has a weak target response and an out-of-band relaxation that is not fitted well, making $\sum_{k=0} \hat{c_k}$ a poor estimate for $H(0)$. Sample #5 of the Type-C mine also has a very weak target response at 18 dB SNR, and $H(0)$ is likely corrupted by the soil.

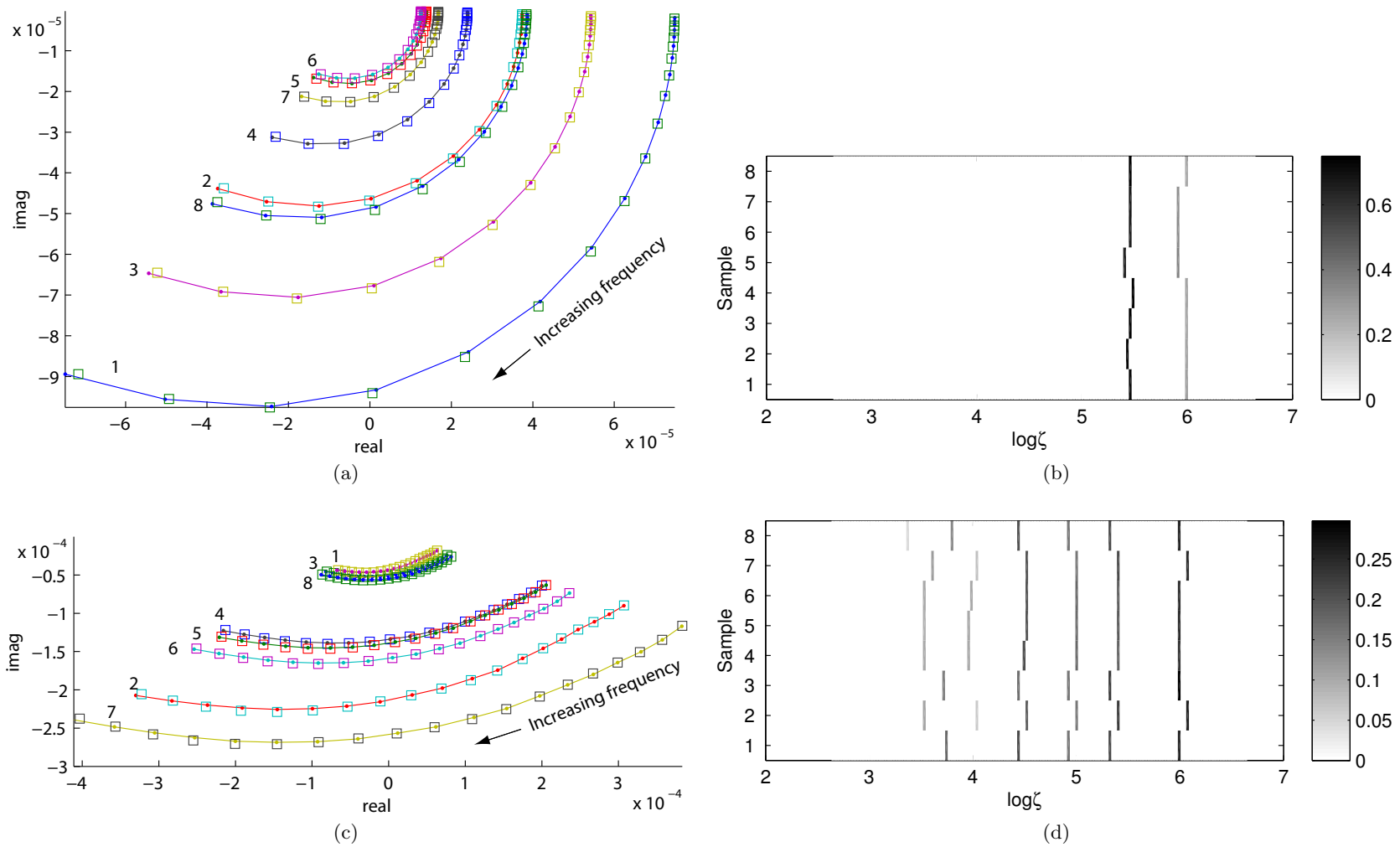

Figure 16: Frequency response and estimated DSRF of Type-A (a,b) and Type-B (c,d) mines measured in the field. (a) The frequency response of eight Type-A mines (solid lines) and their fits (square markers). (b) Estimated DSRFs from the eight frequency responses. (c) The frequency response of eight Type-B mines and their fits. (d) Estimated DSRFs.

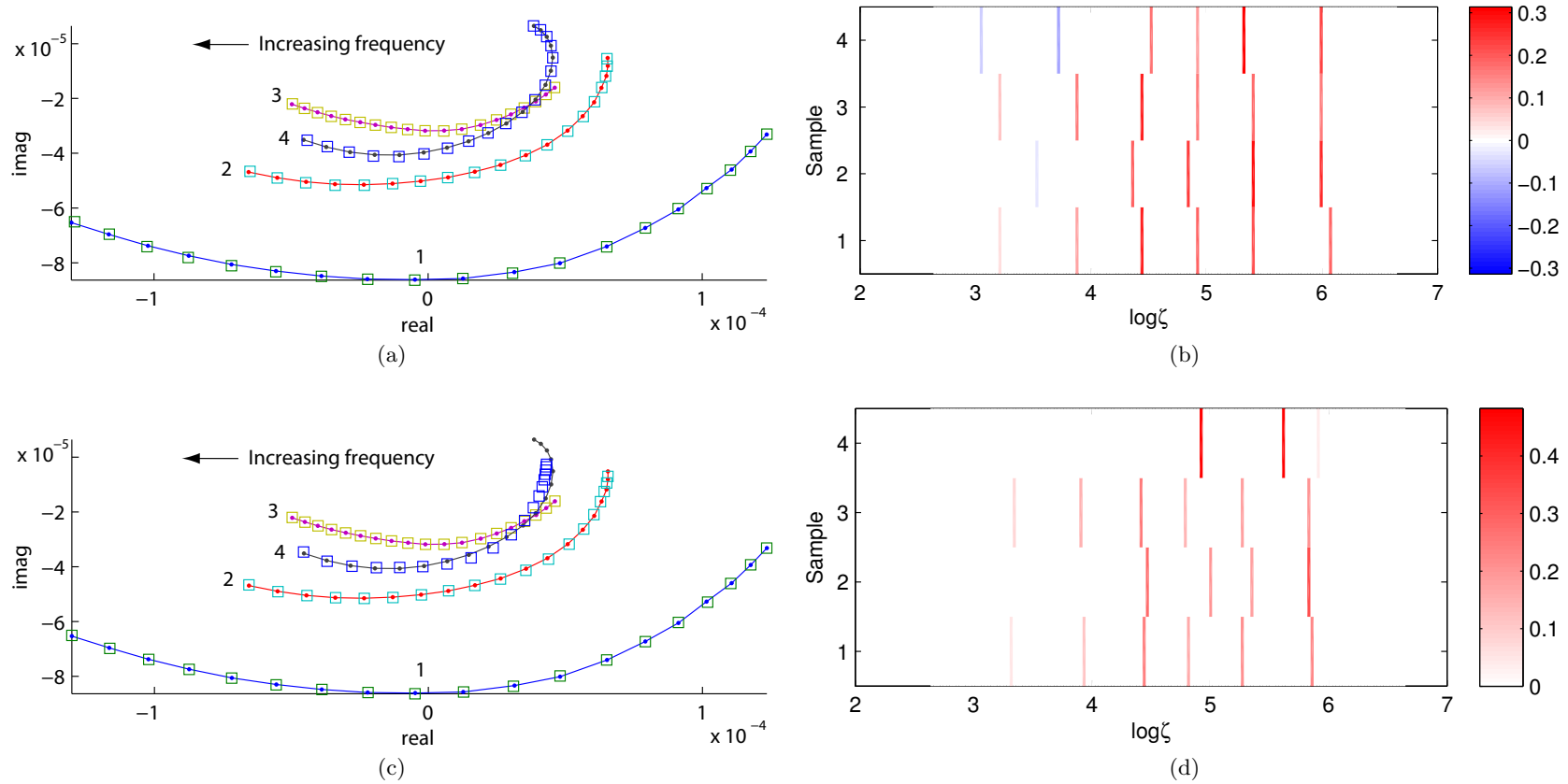

Figure 17: Comparison of the proposed sparsity method (a,b) and the NNLSQ (c,d). The measured frequency responses (solid lines) and their fits (square markers) are shown in (a) and (c), and the estimated DSRF in (b) and (d). Colors red and blue are used to represent positive and negative spectral amplitudes, respectively.

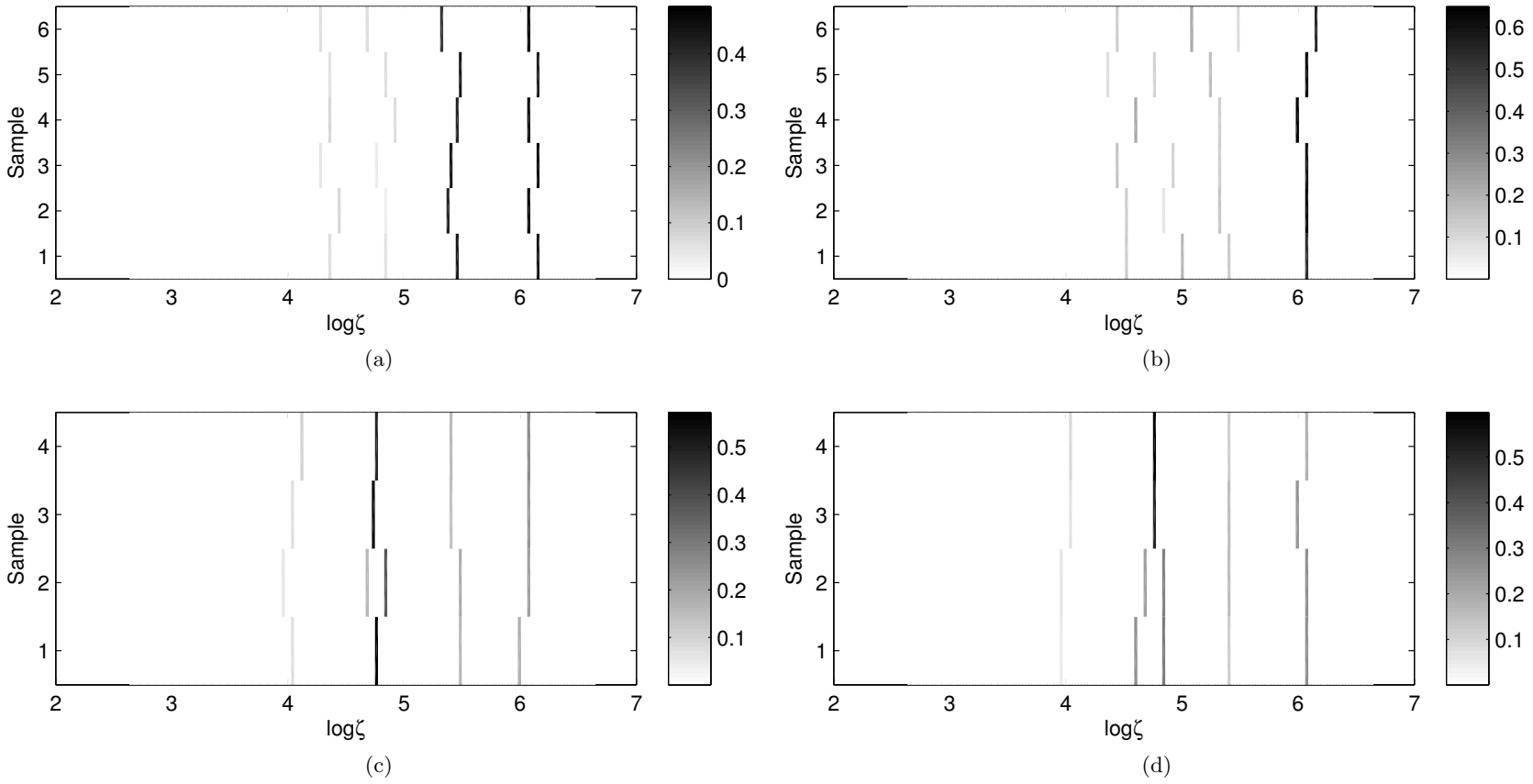

Figure 18: Examples of estimated DSRFs from field targets. The average EMD listed below are in decades and SNR in dB. (a) Six Type-H mines; EMD=0.093, SNR=47. (b) Six Type-I mines; EMD=0.13, SNR=39. (c) Four Type-V mines; EMD=0.11, SNR=42. (d) Four Type-W mines; EMD=0.13, SNR=44.

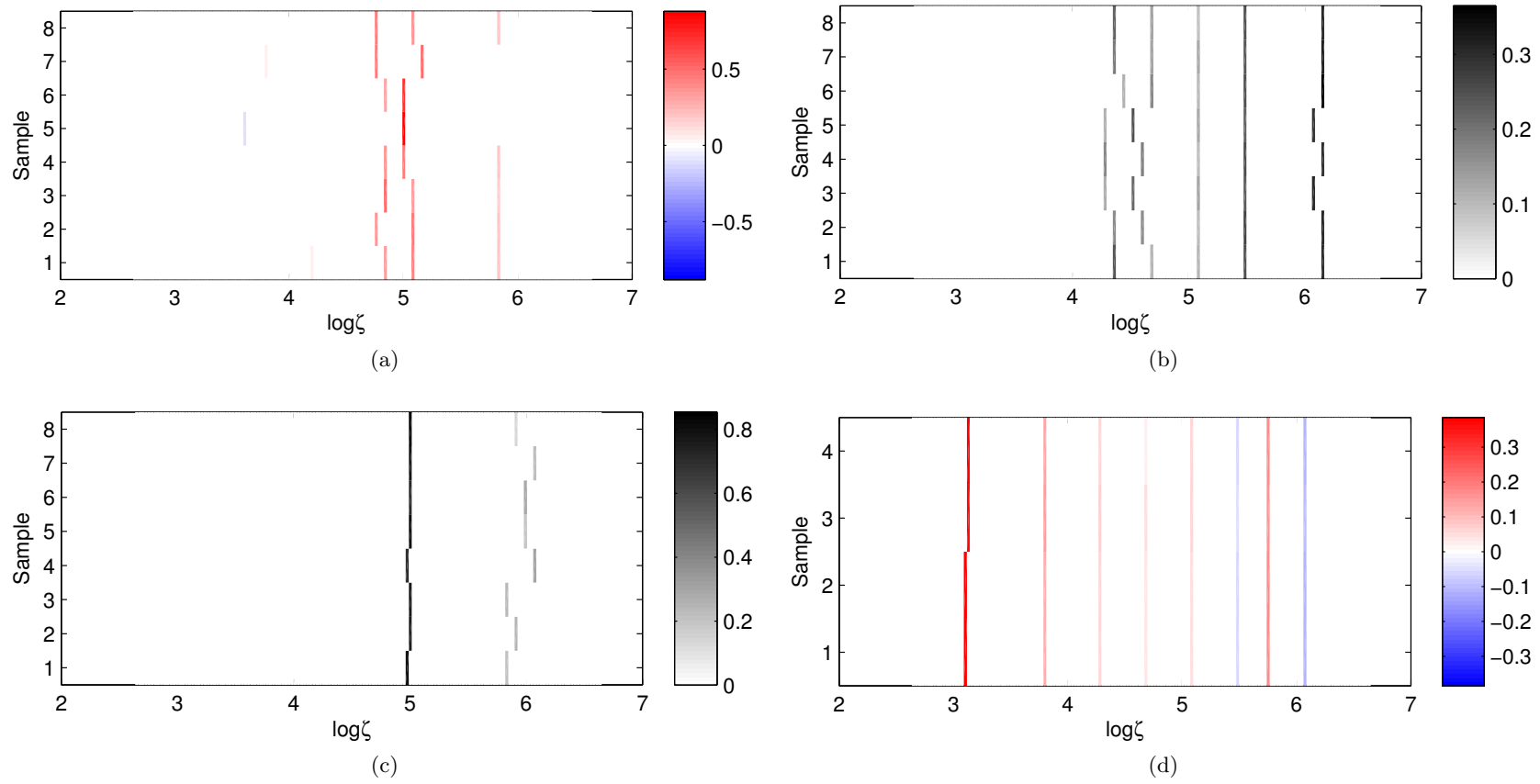

Figure 19: Examples of estimated DSRFs from field targets. The average EMD listed below are in decades and SNR in dB. (a) Eight Type-C mines; EMD=0.2, SNR=26. (b) Eight Type-D mines; EMD=0.085, SNR=82. (c) Eight Type-E mines; EMD=0.093, SNR=26. (d) Four Type-L mines; EMD=0.043, SNR=85.

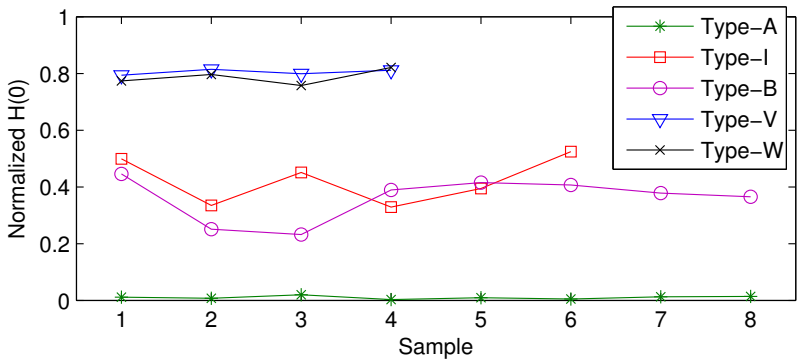

(a)

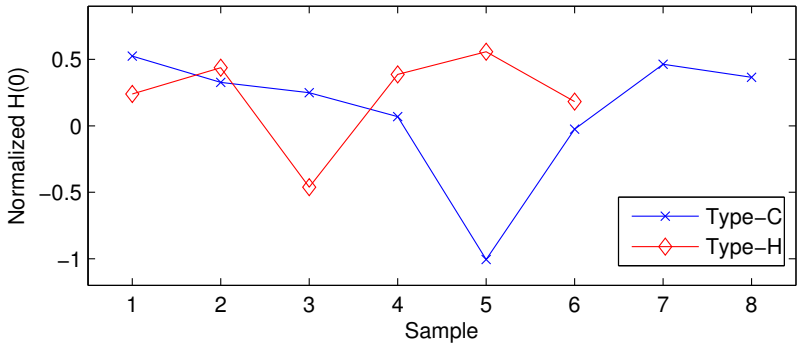

(b)

Figure 20: Normalized estimated $H(0)$ for several mine types. The normalization factor is $\sum 2\hat{c}_k$. (a) Good and consistent $H(0)$ estimates. (b) Mine types with instances of poor $H(0)$ estimates due to low SNR and out-of-band relaxations.

2.4.2 Soil Response and Soil Model

To study the frequency response of soil and its effect on the DSRF, soil responses from the field are collected and examined. These measured frequency responses are collected at grid cells reported to have no objects buried, such as grid 70 in Fig. 15. The frequency response of a subset of these soil responses are plotted in Fig. 21. It is observed that the frequency dependence of the soil responses share a similar trend. The real part has a linear trend with respect to the log-frequency, and the imaginary part tends to be a constant [8, 45].

From these observations, the following soil model is suggested:

$$H_{\mathrm{G}}(\omega) = \gamma \left(\ln \frac{\omega}{\omega_0} + j \frac{\pi}{2} \right), \tag{20}$$

where γ and ω_0 are model parameters. More details about this model can be found in [46].

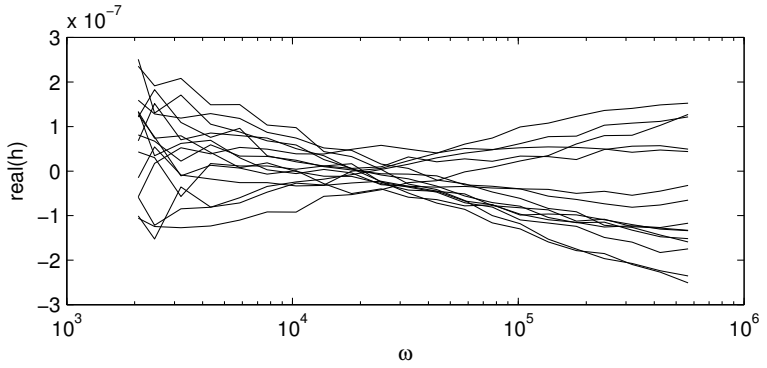

(a)

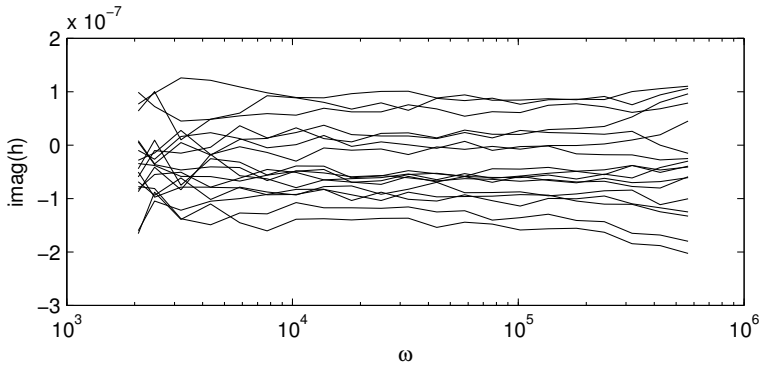

(b)

Figure 21: Instances of measured EMI response of soil. (a) The real part has a linear trend with respect to the log-frequency, and (b) the imaginary part tends to be a constant.

To fit a measured response to the soil model, (20) is rewritten as

$$H_{\mathrm{G}}(\omega) = p_1 + p_2 \left(\ln \omega + j \frac{\pi}{2} \right), \tag{21}$$

where $p1 = -\gamma \ln \omega_0$ and $p2 = \gamma$ are model parameters. For a soil response $\boldsymbol{b}_{\mathrm{G}}$ measured at N frequencies,

$$\boldsymbol{b}_{\mathrm{G}} = \mathbf{G}\mathbf{p} + \mathbf{noise} \qquad , \tag{22}$$

where

$$\mathbf{G} = \begin{bmatrix} 1 & \ln \omega_1 + j\pi/2 \\ 1 & \ln \omega_2 + j\pi/2 \\ \vdots & \vdots \\ 1 & \ln \omega_N + j\pi/2 \end{bmatrix} \qquad \text{and} \qquad \mathbf{p} = \begin{bmatrix} p_1 \\ p_2 \end{bmatrix}.$$

To consider the target response in the presence of soil, as described in Section 1.1, the

total response $\boldsymbol{b}_{\text{Total}}$ can be modeled as

$$\boldsymbol{b}_{\text{Total}} = \boldsymbol{b} + \boldsymbol{b}_{\text{G}} + \mathbf{noise}, \tag{23}$$

where $\boldsymbol{b}$ is the target response. Combining the DSRF model (16) and the soil model (22), the model (23) can be written as a set of linear equations:

$$\boldsymbol{b}_{\text{Total}} = \boldsymbol{A}\boldsymbol{x} + \mathbf{G}\mathbf{p} + \boldsymbol{e}, \tag{24}$$

where $\boldsymbol{e}$ accounts for the modeling error as well as the measurement noise. The two matrices $\boldsymbol{A}$ and $\mathbf{G}$ can then be consolidated into an augmented coefficient matrix $\boldsymbol{\Phi}$. That is,

$$\boldsymbol{b}_{\text{Total}} = \boldsymbol{\Phi}\boldsymbol{\phi} + \boldsymbol{e}, \tag{25}$$

where

$$\boldsymbol{\Phi} = \begin{bmatrix} 1 & \ln\omega_1 + j\pi/2 & \frac{1-j\omega_1/\tilde{\zeta}_1}{1+j\omega_1/\tilde{\zeta}_1} & \frac{1-j\omega_1/\tilde{\zeta}_2}{1+j\omega_1/\tilde{\zeta}_2} & \cdots & \frac{1-j\omega_1/\tilde{\zeta}_M}{1+j\omega_1/\tilde{\zeta}_M} \\ 1 & \ln\omega_2 + j\pi/2 & \frac{1-j\omega_2/\tilde{\zeta}_1}{1+j\omega_2/\tilde{\zeta}_1} & \frac{1-j\omega_2/\tilde{\zeta}_2}{1+j\omega_2/\tilde{\zeta}_2} & \cdots & \frac{1-j\omega_2/\tilde{\zeta}_M}{1+j\omega_2/\tilde{\zeta}_M} \\ \vdots & \vdots & \vdots & \ddots & \vdots & \vdots \\ 1 & \ln\omega_N + j\pi/2 & \frac{1-j\omega_N/\tilde{\zeta}_1}{1+j\omega_N/\tilde{\zeta}_1} & \frac{1-j\omega_N/\tilde{\zeta}_2}{1+j\omega_N/\tilde{\zeta}_2} & \cdots & \frac{1-j\omega_N/\tilde{\zeta}_M}{1+j\omega_N/\tilde{\zeta}_M} \end{bmatrix} \text{ and } \boldsymbol{\phi} = \begin{bmatrix} \tilde{c}_0 + p_1 \\ p_2 \\ \tilde{c}_1 \\ \tilde{c}_2 \\ \vdots \\ \tilde{c}_M \end{bmatrix}. \tag{26}$$

The shift coefficient in the DSRF model $\tilde{c}_0$ and the soil model p_1 are combined in the augmented form, represented by the first entry of $\boldsymbol{\phi}$.

Using the augmented model (25), the target response and the soil response can be modeled simultaneously. The approach to solving (25) is identical to that of solving the DSRF modeling problem (18), that is, minimize the squared error $||\boldsymbol{b}_{\text{Total}} - \boldsymbol{\Phi}\boldsymbol{\phi}||_2^2$ subject to a sparsity regularization $||\boldsymbol{\phi}||_p^p$. The sparsity regularization works for the augmented problem because the sparsity of the solution increases only by one, to account for the second column of $\boldsymbol{\Phi}$, which corresponds to the soil model. Therefore, the solution $\boldsymbol{\phi}$ should still be sparse. In short, the target response and the soil response can be modeled simultaneously by solving the sparsity-regularized least-squares (18) with the dictionary $\boldsymbol{A}$ replaced by the augmented matrix $\boldsymbol{\Phi}$.

The effect of the soil on the field target response is considered here. This is done by comparing DSRF estimates obtained with the soil model via the augmented form (25) and without the soil model (16). Several landmines are examined, and it is found that the two approaches give very similar and sometimes identical estimates. Four examples are given in Fig. 22 and Fig. 23.

In Fig. 22, eight Type-A and eight Type-B mines are examined. For Type-A mines, including the soil model does not produce different DSRF estimates. For Type-B mines, including the soil model produces DSRF estimates that are very similar to those obtained when not using the soil model. Only slight shifts in the relaxation frequencies are observed. The averaged EMD between the two sets is 0.023 decades, which is computed by averaging over the instances the EMD between the DSRFs obtained with and without the soil model.

In Fig. 23, eight Type-C and eight Type-D mines are examined. For Type-C mines, including the soil model produces almost identical DSRF estimates. The average EMD between the two sets is 0.0082 decades. For Type-D mines, including the soil model produces DSRF estimates that are very similar to those obtained not using the soil model. A slight difference is observed in relaxation frequencies near 3.5 and 6 decades. The averaged EMD between the two sets is 0.027 decades.

The four types of mines shown in Fig. 22 and 23 cover a wide range of SNR, from 18 dB to 71 dB, and the consistency between the DSRFs estimated with or without the soil model is observed in all cases. The results show that estimating the DSRF without the soil model (16) produces a DSRF that is very similar to that obtained with the soil model (25). An explanation for this observation is that the soil model does not fit well to a *sparse* DSRF model, so it is, in a sense, orthogonal to the DSRF terms. Therefore, not including the soil term in the modeling does not result in the soil response "leaking" into the DSRF terms. Another reason is simply that the soil response is negligible when the target response is much stronger than the soil response. In either case, the results suggest that it is safe to ignore the soil in estimating the DSRF from field measurements. However, further simulations should be performed to study and quantify the range of SNR over which the soil can be ignored.

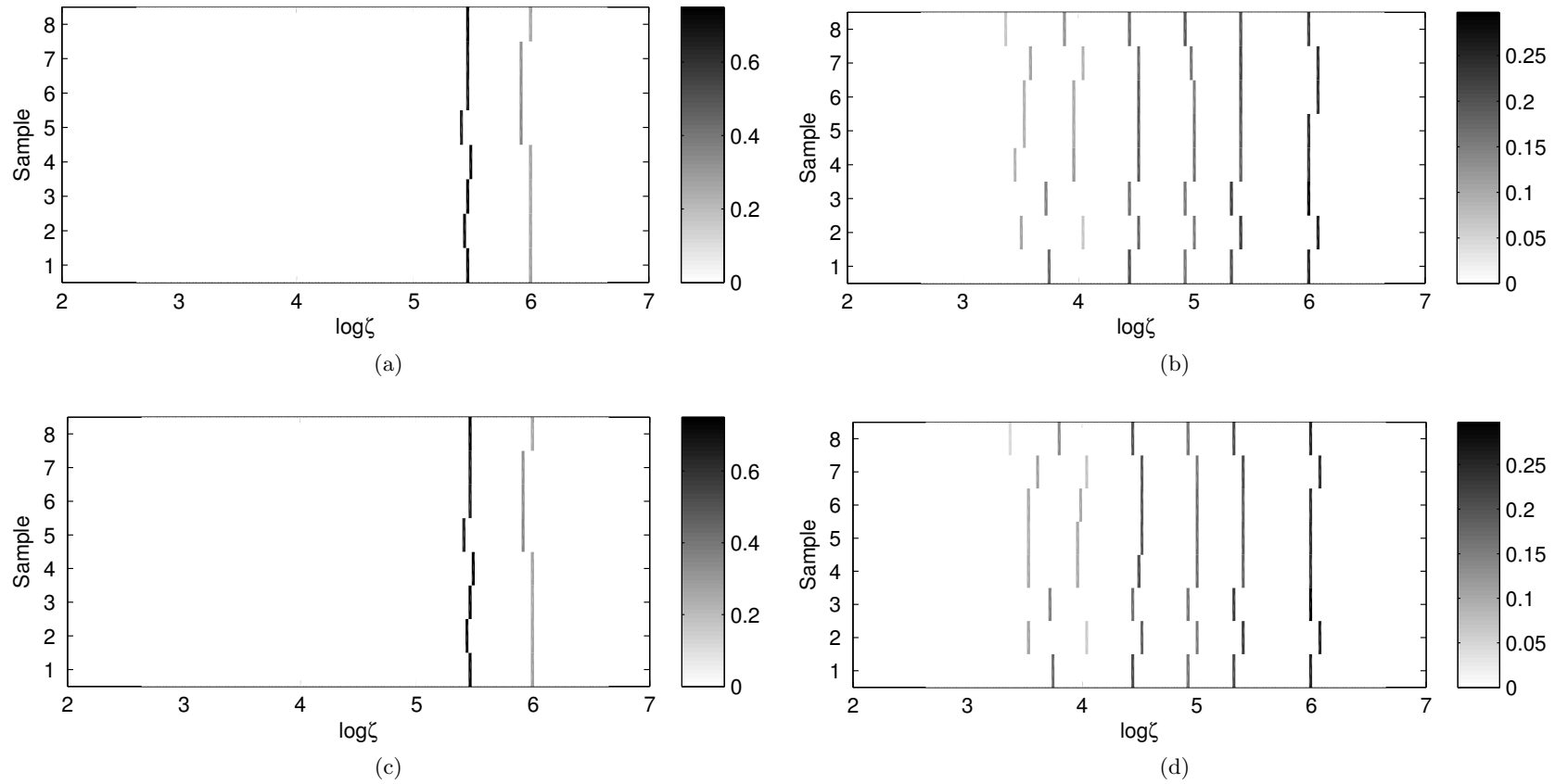

Figure 22: Comparisons of the estimated DSRF when including the soil model (a,b) and not including the soil model (c,d). Shown in (a) and (c) are Type-A mines, and the two sets are identical. Shown in (b) and (d) are Type-B mines, and the average EMD is 0.023 decades between the two sets.

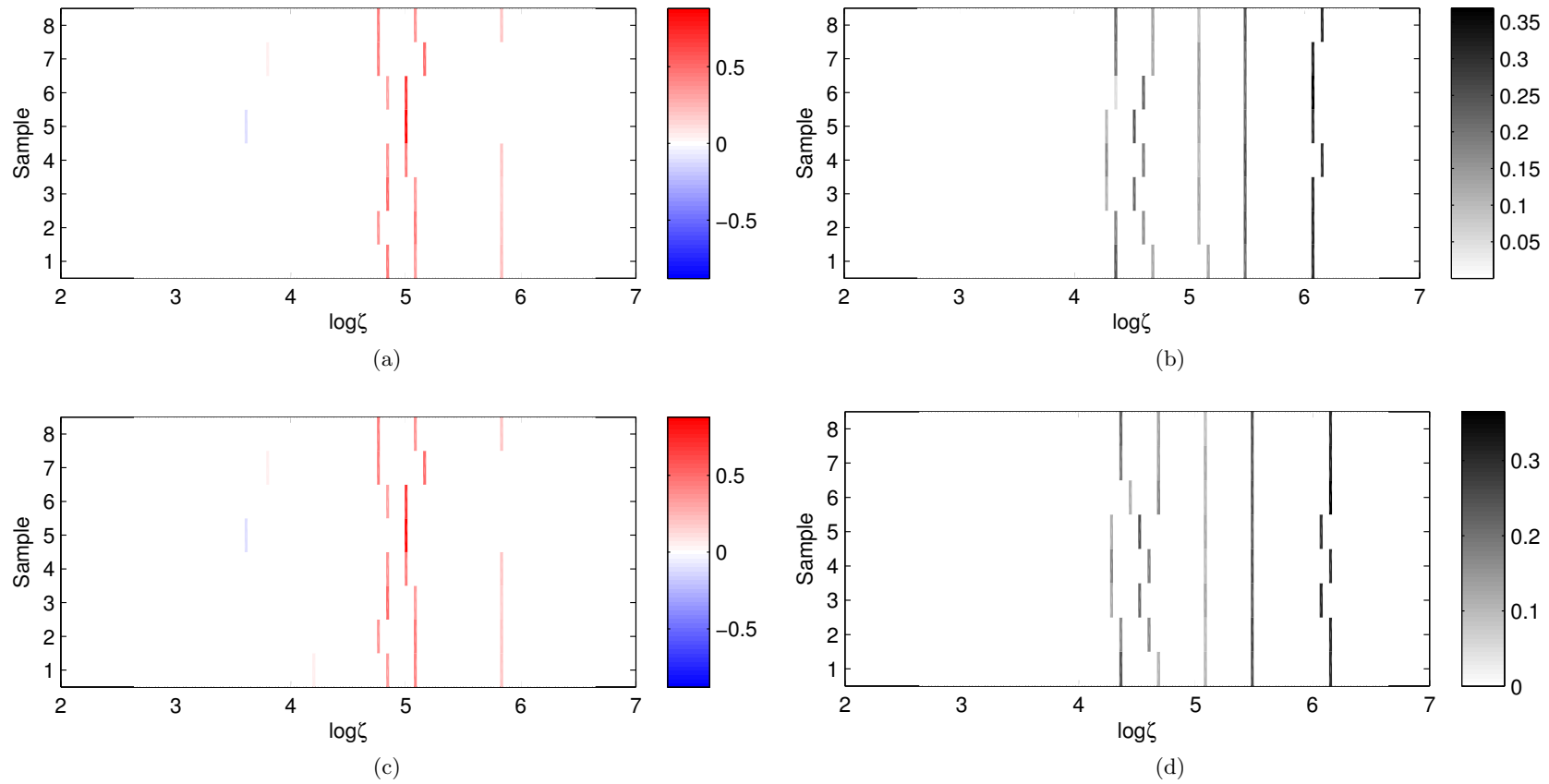

Figure 23: Comparisons of the estimated DSRF when including the soil model (a,b) and not including the soil model (c,d). Shown in (a) and (c) are Type-C mines, and the average EMD is 0.082 decades between the two sets. Shown in (b) and (d) are Type-D mines, and the average EMD is 0.027 decades between the two sets.

2.5 Choosing the Regularization Parameter λ

In this section, it is first examined the behavior of the proposed method in relation to the regularization parameter λ, and then a simple λ selection rule is proposed exploiting the observed properties of λ. All discussions and figures presented here assume $p = 0.5$ unless otherwise specified.

To understand how the goodness of fit changes with λ and SNR, a cross-validation-like simulation is conducted. First, a collection of synthetic spectra are built with different model orders and a variety of distributions of relaxations. For each spectrum at a fixed SNR, the spectrum is estimated 100 times for each λ within a range, and the average goodness of fit, measured by the EMD between the available truth and the estimate, is recorded. This is done for a range of SNRs. The simulation result for a four-relaxation spectrum, as an example, is shown in Fig. 24. Not only is the EMD surface well-behaved (i.e., smooth) with respect to the SNR and λ, but more importantly the surface itself is convex-shaped. Thus, at each SNR, the minimum EMD is achievable by a unique λ. The wide valley of the surface also shows that the goodness of fit is not very sensitive near the optimal λ that gives the minimum EMD per SNR.

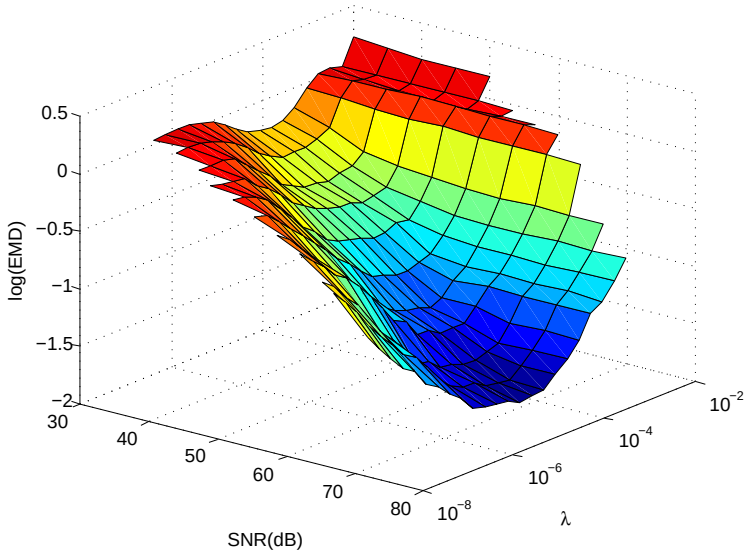

Figure 24: Monte Carlo simulation of the goodness of estimation (EMD) of a four-relaxation spectrum at different SNR's and λ's.

Simulations of spectra for other model orders and distributions also exhibit the same property (Fig. 25). Moreover, the valleys of the EMD surface all occur in nearly the same SNR-λ region. In other words, the λ that produces the minimum EMD at a given SNR is quasi-independent of the model order. Figure 26 shows the averaged EMD of different model orders in Fig. 25. The resulting surface still exhibits the properties described above. This allows us to pick a near-optimal λ based solely on the SNR.

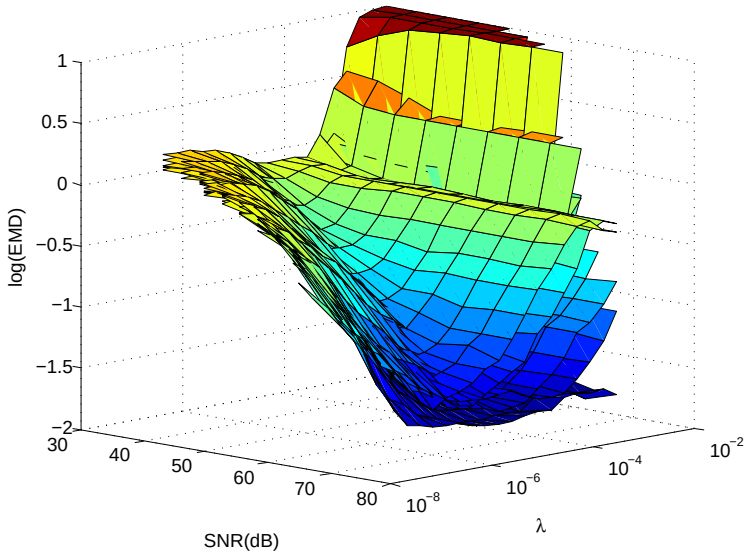

Figure 25: Same simulation as in Fig. 24, but for spectra of different model orders (1 to 6). Each spectrum constitutes one surface in the figure. All surfaces have their minimum in the same SNR-λ region.

In Fig. 26, the optimal λ at each SNR which is also plotted. Using the wide-valley property, the near-minimum EMD can be achieved by choosing λ's that are near the optimal λ in the valley. Here the optimal λ is approximated with a semilog function of SNR. This is done by fitting the optimal log-λ curve with a linear function. Weights may be added to promote certain SNR's that are more important. For our problem setup, the λ is chosen by (also shown in Fig. 26)

$$\log \lambda = -0.05 \cdot \mathrm{SNR} - 2.2 \tag{27}$$

In practice, this log-λ selection rule that is linear in SNR allows the regularization parameter to be determined with negligible computation time. When processing the laboratory data, (27) is used along with an estimate of the SNR to determine λ for use in **Algorithm 1**.

The same empirical method can be repeated for other p's, and the result is also a linear relationship between $\log \lambda$ and SNR.

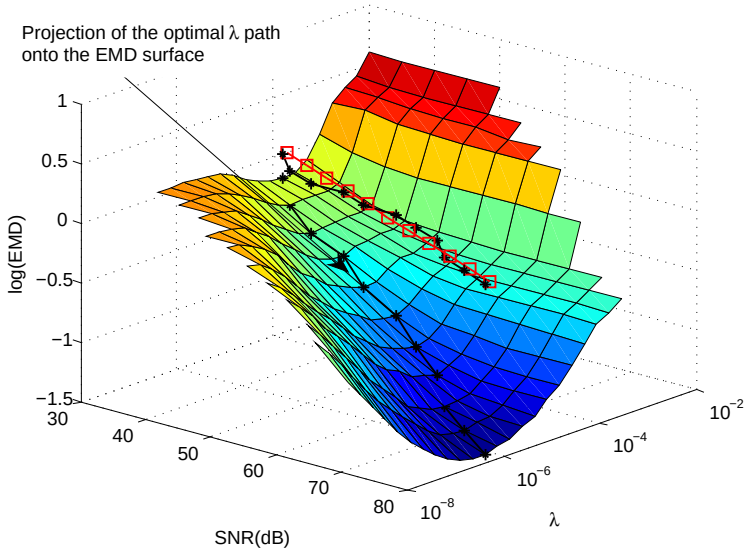

Figure 26: Average of EMD surfaces in Fig. 25. The curve with asterisk markers traces out the optimal λ's. The line with square markers is the approximated optimal λ curve used to select λ in practical estimation.

Figure 27 compares the goodness of estimation of a four-relaxation target using the linear log-λ selection rule and the optimal λ which uses the true spectrum that is not available in practice. There is a slight increase in the EMD when the linear log-λ selection rule is used, which is reasonable and expected. The increase is acceptable and hence the linear log-λ selection rule is an appropriate λ selector.

Also shown in Fig. 27 are the performances of other p values. It is seen that $p < 1$ gives more accurate results than $p = 1$ when the optimal λ is used, but this advantage is significantly diminished when the linear log-λ selection rule is used. While this lessens the advantages of using $p < 1$, it is emphasized that $p = 1$ tends to give estimates with many relaxation frequencies while $p < 1$ gives sparser spectra which are more physically accurate (see Section 2.2.2). It is possible that both the accuracy and the sparsity advantages for $p < 1$ could be obtained with a better λ selection rule. Lastly, since the performance of a certain p value is dependent on the λ selection rule used, different optimum p values would be determined if the λ selection rule is changed.

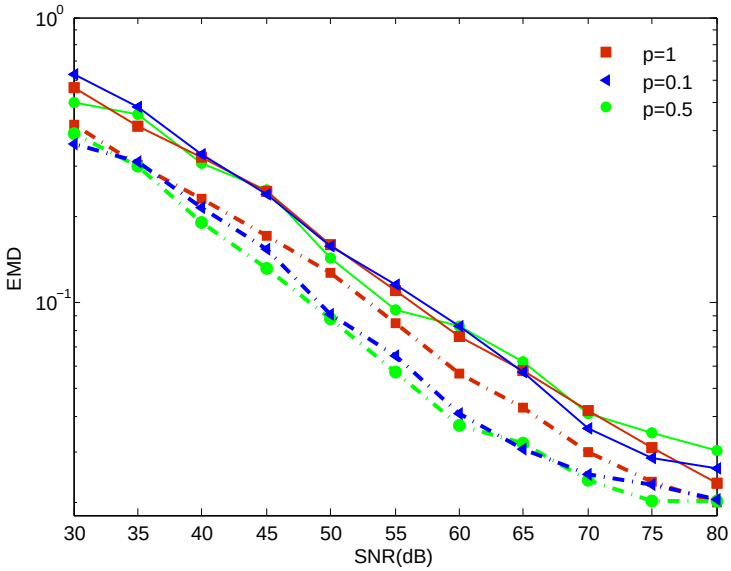

Figure 27: Goodness of fit using the linear log-λ selection rule for several p's. The true spectrum is the same as in Fig. 24. Dash-dot curves denote the optimal λ, solid lines denote the linear log-λ selection rule.

CHAPTER III

SPECTRUM ESTIMATION FROM MULTIPLE MEASUREMENTS

In the process of acquiring the EMI response of a target, often the target response is measured at different target-to-sensor orientations and locations. For example, this happens when an EMI sensor collects data while moving over a target, resulting measurement views of the target from different angles, as illustrated in Fig. 2 in Chapter 1. It seems reasonable that more accurate estimates of the DSRF can be obtained with more views or snapshots of the target, for two reasons: 1) the relaxation frequencies are constant in different views and 2) a relaxation that vanishes ($c_k = 0$) in one view can appear in a different view, as illustrated in Fig. 13 in Chapter 2.

To utilize the multiple measurements often available for a target, a multiple-measurement vector (MMV) DSRF estimation method is developed in this chapter. The MMV method exploits the property of orientation and position invariance of the relaxation frequencies, and obtains more accurate estimates by encouraging different measurements (views of a target) that share a common set of relaxation frequencies. The proposed MMV method is applied to synthetic, laboratory, and field data, and the performance is demonstrated to be robust and better than the SMV approach.

The MMV DSRF estimation is a generalization of the single-measurement vector (SMV) approach (Chapter 2), but the MMV generalization does more because the SMV does not exploit the invariance of the relaxation frequencies. The MMV has an advantage over the SMV by taking into account this physical invariance property.

A "row-sparsity measure" for matrices is introduced to encourage DSRF estimates for the same target to share the same relaxation frequencies. This measure formulates the MMV problem in a form similar to the SMV, allowing SMV techniques to be extended to the MMV case in a straightforward manner.

The MMV method follows the same framework as the SMV: 1) sample the relaxation frequency domain, 2) construct an overcomplete dictionary, 3) perform a sparsity-promoting optimization, and 4) interpolate. Because steps 1) and 2) are identical to the SMV approach, the discussion here is focused on the MMV sparsity-promoting optimization and interpolation.

3.1 Method Formulation

A single EMI response measured at N frequencies can be modeled by a set of sampled relaxation frequencies using the following matrix equation

$$\underbrace{\begin{bmatrix} H(\omega_1) \\ H(\omega_2) \\ \vdots \\ H(\omega_N) \end{bmatrix}}_{\boldsymbol{b}} = \underbrace{\begin{bmatrix} 1 & \frac{1-j\omega_1/\tilde{\zeta}_1}{1+j\omega_1/\tilde{\zeta}_1} & \frac{1-j\omega_1/\tilde{\zeta}_2}{1+j\omega_1/\tilde{\zeta}_2} & \cdots & \frac{1-j\omega_1/\tilde{\zeta}_M}{1+j\omega_1/\tilde{\zeta}_M} \\ 1 & \frac{1-j\omega_2/\tilde{\zeta}_1}{1+j\omega_2/\tilde{\zeta}_1} & \frac{1-j\omega_2/\tilde{\zeta}_2}{1+j\omega_2/\tilde{\zeta}_2} & \cdots & \frac{1-j\omega_2/\tilde{\zeta}_M}{1+j\omega_2/\tilde{\zeta}_M} \\ \vdots & \vdots & \vdots & \ddots & \vdots \\ 1 & \frac{1-j\omega_N/\tilde{\zeta}_1}{1+j\omega_N/\tilde{\zeta}_1} & \frac{1-j\omega_N/\tilde{\zeta}_2}{1+j\omega_N/\tilde{\zeta}_2} & \cdots & \frac{1-j\omega_N/\tilde{\zeta}_M}{1+j\omega_N/\tilde{\zeta}_M} \end{bmatrix}}_{\boldsymbol{A}} \underbrace{\begin{bmatrix} \tilde{c}_0 \\ \tilde{c}_1 \\ \tilde{c}_2 \\ \vdots \\ \tilde{c}_M \end{bmatrix}}_{\boldsymbol{x}} + \boldsymbol{e},$$

or

$$\boldsymbol{b} = \boldsymbol{A}\boldsymbol{x} + \boldsymbol{e}, \tag{28}$$

as described in Section 2.1.3. For multiple measurements $\boldsymbol{b}_1, \ldots, \boldsymbol{b}_L$, one can form a system of equations

$$\left[\boldsymbol{b}_1, \boldsymbol{b}_2, \ldots, \boldsymbol{b}_L\right] = \boldsymbol{A}\left[\boldsymbol{x}_1, \boldsymbol{x}_2, \ldots, \boldsymbol{x}_L\right] + \left[\boldsymbol{e}_1, \boldsymbol{e}_2, \ldots, \boldsymbol{e}_L\right] \text{ , or} \tag{29}$$

$$\boldsymbol{B} = \boldsymbol{A}\boldsymbol{X} + \boldsymbol{E}, \tag{30}$$

where $\boldsymbol{B} \in \mathbb{C}^{N\times L}$ has columns of $\boldsymbol{b}_1, \ldots, \boldsymbol{b}_L$, and similarly for $\boldsymbol{X} \in \mathbb{R}^{(M+1)\times L}$ and $\boldsymbol{E} \in \mathbb{C}^{N\times L}$. If the L measurements come from the same target, then $\boldsymbol{x}_1, \ldots, \boldsymbol{x}_L$ share the *same location of nonzero entries* because $\boldsymbol{b}_1, \ldots, \boldsymbol{b}_L$ share the same relaxation frequencies, as a consequence of the orientation and location invariance. This means the matrix $\boldsymbol{X}$ should be *row sparse*, having only nonzero entries on certain rows.

In other words, the invariance property of the relaxation frequencies translates to the row-sparse property of the matrix $\boldsymbol{X}$. Row sparsity is precisely the property one can exploit

in an algorithm that estimates the DSRF of a target from multiple measurements.

3.1.1 Row-Sparsity Measure

To promote solutions that are row-sparse, a measure is needed to quantify the degree of row sparsity. One straightforward measure is to collapse the matrix $\boldsymbol{X}$ row-wise by the vector norm $||\cdot||_q$ [47], resulting in a *sparse vector*. This can be done via the function $\mathcal{R}_{\ell_q} : \mathbb{R}^{M+1\times L} \to \mathbb{R}^{M+1}$ defined by

$$\mathcal{R}_{\ell_q}(\boldsymbol{X}) = \begin{bmatrix} ||x_{1,1} & x_{1,2} & \dots & x_{1,L}||_q \\ ||x_{2,1} & x_{2,2} & \dots & x_{2,L}||_q \\ & \vdots & \vdots & \\ ||x_{M+1,1} & x_{M+1,2} & \dots & x_{M+1,L}||_q \end{bmatrix} = \begin{bmatrix} ||\mathbf{x}_1||_q \\ ||\mathbf{x}_2||_q \\ \vdots \\ ||\mathbf{x}_{\mathrm{M+1}}||_q \end{bmatrix}, \tag{31}$$

$$\text{where} \quad ||\mathbf{x}_{\mathrm{m}}||_q = \left(\sum_{l=1}^{L} |x_{m,l}|^q \right)^{1/q}, \tag{32}$$

$\mathbf{x}_{\mathrm{m}} \in \mathbb{R}^L$ is the m^{th} row of $\boldsymbol{X}$, and $x_{m,l}$ are the entries of the matrix $\boldsymbol{X}$.

The vector $\mathcal{R}_{\ell_q}(\boldsymbol{X})$ should be a sparse vector, and familiar sparsity measures for single measurements, such as the ℓ_1 norm [48] or the diversity measure [49], can be applied to $\mathcal{R}_{\ell_q}(\boldsymbol{X})$. This composite row-sparsity measure of a matrix is denoted $J^{(p,q)}(\boldsymbol{X})$ and is defined by [39, 40, 49]

$$J^{(p,q)}(\boldsymbol{X}) = \begin{cases} \sum_{m=1}^{M+1} \log\left(||\mathbf{x}_{\mathrm{m}}||_q + \epsilon\right) & , p = 0 \\ ||\mathcal{R}_{\ell_q}(\boldsymbol{X})||_p^p = \sum_{m=1}^{M+1} ||\mathbf{x}_{\mathrm{m}}||_q^p & , 0 < p \leq 1 \end{cases}, \tag{33}$$

where $\epsilon > 0$ is a small positive real number introduced for stability.

The purpose of the log-sum function and the ℓ_p quasi-norms in (33) is to *approximate* the ℓ_0 quasi-norm ($||\cdot||_0$), which is the number of nonzero entries in a vector. Fig. 28 gives the contour plots of the different ℓ_p quasi-norms as well the log-sum function. The log-sum function is a closer approximation to the ℓ_0 quasi-norm than the ℓ_1 norm and other $p < 1$ quasi-norms. The log-sum function has a slope that vanishes near the axes like $||\cdot||_0$ does. On the other hand, the ℓ_1 norm is less similar to $||\cdot||_0$. Other functions have also been suggested to better approximate the ℓ_0 quasi-norm [39, 40, 50].

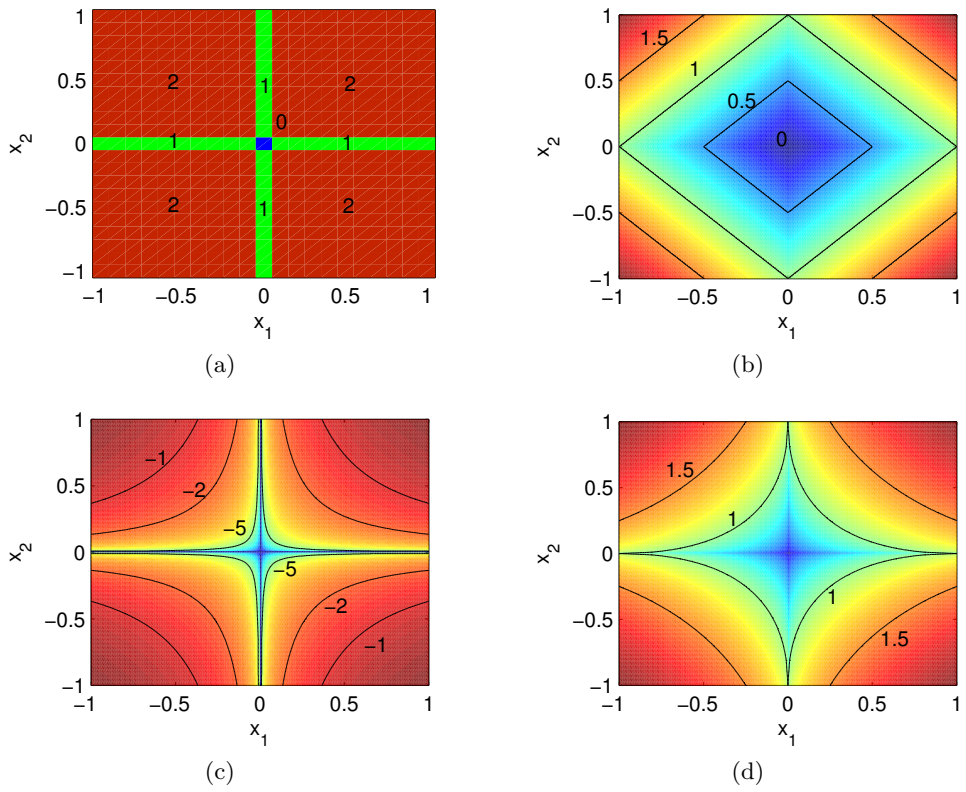

Figure 28: Surface plots of various (quasi-)norms in $\mathbb{R}^2$. (a) ℓ_0 quasi-norm. (b) ℓ_1 norm. (c) $\sum \log(|x_i| + \epsilon)$. (d) $\ell_{1/2}$ quasi-norm.

While there are conditions that guarantee minimizing the ℓ_1 norm is equivalent to finding the minimum ℓ_0 quasi-norm [51,52], these conditions are not practical for DSRF estimation when there is measurement noise and/or an imperfect model (dictionary). On the other hand, it can be shown that minimizing the ℓ_p quasi-norm for $p < 1$ or the log-sum function via reweighted algorithms, gives sparser solutions and more robust performance [39,40].

3.1.2 MMV Optimization

Using the row-sparsity measure $J^{(p,q)}(\boldsymbol{X})$, the invariance of the relaxation frequencies can be exploited to effectively model an EMI signal. To estimate the model parameters, one optimizes the problem

$$\arg\min_{\boldsymbol{X}} ||\boldsymbol{A'X} - \boldsymbol{B'}||_F + \lambda J^{(p,q)}(\boldsymbol{X}), \tag{34}$$

$$\text{where } \boldsymbol{A'} = \begin{bmatrix} \mathfrak{Re}(\boldsymbol{A}) \\ \mathfrak{Im}(\boldsymbol{A}) \end{bmatrix}, \boldsymbol{B'} = \begin{bmatrix} \mathfrak{Re}(\boldsymbol{B}) \\ \mathfrak{Im}(\boldsymbol{B}) \end{bmatrix},$$

$||\cdot||_F$ is the Frobenius norm and λ is a regularization parameter that controls the trade-off between sparsity and the modeling residual.

This optimization (34) for MMV is similar to that of the SMV (Section 2.1.3) but with the vectors replaced by matrices, the vector norm replaced by the Frobenius norm, and the ℓ_p norm replaced by $J^{(p,q)}(\boldsymbol{X})$. The real and imaginary parts are again separated to ensure real-valued solutions.

Equation (34) is in the form of a regularized MMV problem, and can be solved by iteratively reweighted MMV techniques, such as M-FOCUSS or M-IRL1 [53,54]. Algorithms to solve this problem are examined in Section 3.2, and their performance is compared in Section 3.3, where M-FOCUSS is chosen as the default solver for its robustness.

The above optimization requires selecting the regularization parameter λ, as explained in Section 2.5, which is nonintuitive. An alternative optimization is to use a threshold, $\boldsymbol{\theta} \in \mathbb{R}^L$, to specify the difference between the modeled signals and the measurements, which usually contains unwanted signals such as noise or soil response. The alternative threshold MMV method is

$$\underset{\boldsymbol{X}}{\arg\min}\ J^{(p,q)}(\boldsymbol{X}) \quad \text{subject to} \quad \mathcal{C}_{\ell_q}(\boldsymbol{B} - \boldsymbol{A}\boldsymbol{X}) < \boldsymbol{\theta}, \tag{35}$$

where $\mathcal{C}_{\ell_q} : \mathbb{C}^{N\times L} \to \mathbb{R}^L$ is a function like $\mathcal{R}_{\ell_q}$ but operates along the columns of a matrix. That is,

$$\mathcal{C}_{\ell_q}(\boldsymbol{E}) = [||\boldsymbol{e}_1||_q, \ldots, ||\boldsymbol{e}_L||_q]^T, \tag{36}$$

$$\text{where} \quad ||\boldsymbol{e}_l||_q = \left(\sum_{n=1}^{N} |e_{n,l}|^q\right)^{1/q}. \tag{37}$$

This form provides more physical intuition such as limiting the measurement noise. However, the solution to (35) is more sensitive to $\boldsymbol{\theta}$ than the regularized approach. This threshold MMV can be iteratively solved similar to the implementation of the regularized M-IRL1 [54].

3.1.3 Interpolation of Relaxation Frequencies

Sampling in the relaxation frequency domain always introduces the issue of an actual relaxation ζ occurring between two consecutive sampled relaxation frequencies $\tilde{\zeta}_a$ and $\tilde{\zeta}_b$:

$$\tilde{\zeta}_a < \zeta < \tilde{\zeta}_b. \tag{38}$$

When this happens, solutions to (34) tend to return nonzero values in the rows corresponding to $\tilde{\zeta}_a$ and $\tilde{\zeta}_b$. In addition, the magnitudes of these two entries reflect how close ζ is to a sample point. For example, as ζ move closer to $\tilde{\zeta}_a$ from $\tilde{\zeta}_b$, $||\mathbf{x}_\mathrm{a}||$ increases while $||\mathbf{x}_\mathrm{b}||$ decreases. The interpolation scheme for the single measurement case [33] can be extended to the MMV:

$$\log \hat{\zeta} = \frac{1}{L} \sum_{l=1}^{L} \frac{\sum_{m=a}^{b} |x_{m,l}| \log \tilde{\zeta}_m}{\sum_{m=a}^{b} |x_{m,l}|}, \tag{39}$$

where $\hat{\zeta}$ is the estimated ζ. This interpolation also applies to more than two consecutive nonzero rows, i.e., $b > a + 1$.

An alternative way to interpolate the estimated ζ is

$$\log \hat{\zeta} = \frac{\sum_{m=a}^{b} ||\mathbf{x}_\mathrm{m}|| \log \tilde{\zeta}_m}{\sum_{m=a}^{b} ||\mathbf{x}_\mathrm{m}||}, \tag{40}$$

which is similar to (39). But (39) is preferred because the interpolation is done *per measurement* (the l-dependence) and then the average across l is taken, which reduces variance in the estimates. On the other hand, interpolation based on the row norm $||\mathbf{x}_\mathrm{m}||$ loses information in each measurement and can be overwhelmed by one measurement that is much stronger than others.

3.1.4 Estimation of Spectral Amplitudes

Once the relaxation frequencies have been identified, the spectral amplitudes can be found via a standard linear least-squares minimization using the estimated relaxation frequencies $\hat{\zeta}$. The estimated (interpolated) relaxation frequencies are denoted by $\hat{\zeta}_1, \hat{\zeta}_2, \ldots, \hat{\zeta}_{\hat{K}}$, where $\hat{K}$ is the estimated number of relaxation frequencies. Because X is row-sparse, $\hat{K} \ll M$. When the estimate is accurate, $\hat{K} \approx K$, if not $\hat{K} = K$.

First, a coefficient matrix $\hat{\boldsymbol{Z}} \in \mathbb{C}^{N \times \hat{K}}$ is constructed:

$$\hat{\boldsymbol{Z}} = \begin{bmatrix} 1 & \frac{1-j\omega_1/\hat{\zeta}_1}{1+j\omega_1/\hat{\zeta}_1} & \frac{1-j\omega_1/\hat{\zeta}_2}{1+j\omega_1/\hat{\zeta}_2} & \cdots & \frac{1-j\omega_1/\hat{\zeta}_{\hat{K}}}{1+j\omega_1/\hat{\zeta}_{\hat{K}}} \\ 1 & \frac{1-j\omega_2/\hat{\zeta}_1}{1+j\omega_2/\hat{\zeta}_1} & \frac{1-j\omega_2/\hat{\zeta}_2}{1+j\omega_2/\hat{\zeta}_2} & \cdots & \frac{1-j\omega_2/\hat{\zeta}_{\hat{K}}}{1+j\omega_2/\hat{\zeta}_{\hat{K}}} \\ \vdots & \vdots & \vdots & \ddots & \vdots \\ 1 & \frac{1-j\omega_N/\hat{\zeta}_1}{1+j\omega_N/\hat{\zeta}_1} & \frac{1-j\omega_N/\hat{\zeta}_2}{1+j\omega_N/\hat{\zeta}_2} & \cdots & \frac{1-j\omega_N/\hat{\zeta}_{\hat{K}}}{1+j\omega_N/\hat{\zeta}_{\hat{K}}} \end{bmatrix}. \tag{41}$$

Unlike the dictionary $\boldsymbol{A}$ that is underdetermined, $\hat{\boldsymbol{Z}}$ is likely overdetermined, i.e., $N > \hat{K}$. Therefore, the residual from the linear least-squares minimization

$$\min_{\hat{\boldsymbol{c}}_l} ||\boldsymbol{b}_l - \hat{\boldsymbol{Z}}\hat{\boldsymbol{c}}_l||_2^2 \tag{42}$$

is unlikely to be zero. This residual, which is perpendicular to the column space of $\hat{\boldsymbol{Z}}$, is regarded as the noise/unwanted signal rejected by the EMI model. In addition, because the estimated ζ are sparse and adjacent $\tilde{\zeta}$ are interpolated, $\hat{\zeta_k}$ are spaced-out, implying the columns of $\hat{\boldsymbol{Z}}$ are linearly independent. Because $\hat{\boldsymbol{Z}}$ is overdetermined and has linearly independent columns, there is a *unique* solution to the linear least squares (42), which can be obtained via the pseudoinverse.

To ensure only real-valued spectral amplitudes, a real-valued matrix $\hat{\boldsymbol{Z}}' \in \mathbb{R}^{2N\times\hat{K}}$ is constructed similar to that of $\boldsymbol{A}'$ in (18). The same arguments for $\hat{\boldsymbol{Z}}$ being overdetermined and having linearly independent columns transfer to $\hat{\boldsymbol{Z}}'$. Therefore, the spectral amplitudes can be estimated using the pseudoinverse $\hat{\boldsymbol{Z}}'^{+}$:

$$\hat{\boldsymbol{c}}_l = \hat{\boldsymbol{Z}}'^{+}\boldsymbol{b}' \quad l = 1\ldots L, \text{ or} \tag{43}$$

$$\hat{\boldsymbol{C}} = \hat{\boldsymbol{Z}}'^{+}\boldsymbol{B}'. \tag{44}$$

For each measurement $\boldsymbol{b}_l$, the estimated DSRF is $\hat{S}_l = \{(\hat{\zeta_k}, \hat{c}_{k,l}) : k = 1\ldots\hat{K}\}$. The estimated relaxation frequencies $\hat{\zeta_k}$ are l-independent, invariant from measurement to measurement.

3.2 MMV Optimizers

Several algorithms have been proposed to solve the MMV problem. In this section, these solvers are examined to select the ones that are best suited for the DSRF estimation. Five algorithms are considered: M-BP [47, 55], M-OMP [47], M-FOCUSS [53], ReMBo (with BP) [56], and M-IRL1 [54].

A set of noiseless simulations were performed to evaluate these algorithms. The simulation results suggest that the non-convex optimizations, M-FOCUSS ($p = 0$) and M-IRL1, deliver the most robust performance. These two methods are further examined. Regularization is introduced to accommodate noisy measurements. When regularized, the simulation

result using noisy measurements suggest that M-FOCUSS is slightly better than M-IRL1. In addition, because M-FOCUSS takes less computation time, it is chosen to be the default solver for DSRF estimation in this work.

3.2.1 Algorithms

Most of the MMV algorithms are extensions of existing SMV recovery methods. Extension of the Basis Pursuit to the MMV problem (M-BP) is considered in [47, 55], where the objective is to minimize the number of rows containing nonzero entries while satisfying $\boldsymbol{B} = \boldsymbol{A}\boldsymbol{X}$. The problem is formulated as

$$\min ||\mathcal{R}_{\ell_q}(\boldsymbol{X})||_0 \quad \text{subject to} \quad \boldsymbol{B} = \boldsymbol{A}\boldsymbol{X}, \tag{45}$$

where $||\cdot||_0$ is number of nonzero entries in a given vector. As in the SMV problem, (45) is NP-hard but can be made convex as an ℓ_1 minimization problem:

$$\min ||\mathcal{R}_{\ell_q}(\boldsymbol{X})||_1 \quad \text{subject to} \quad \boldsymbol{B} = \boldsymbol{A}\boldsymbol{X}. \tag{46}$$

When the nonzero rows in $\boldsymbol{X}$ are sparse enough, (46) recovers the same solution as (45). The condition for which (45) and (46) are equivalent can be found in [47, 55]. It was also shown that an exact recovery does not depend on the ℓ_q norm chosen for $\mathcal{R}_{\ell_q}$.

On the other hand, greedy algorithms have also been extended to accommodate MMV problems [53, 57, 58]. Various MMV methods based on Matching Pursuit (MP) have been proposed, such as the MMV orthogonal matching pursuit (M-OMP). The condition for exact recovery was also established [47, 53].

From a slightly different approach, the ReMBo method proposed in [56] solves a MMV problem by recasting it into a series of SMV problems. The method can incorporate both convex relaxation and greedy algorithms, and is shown to be robust.

Sparsity could be further enhanced through iteratively reweighting. In particular, it was shown in [39, 49] that sparse solutions for a SMV problem can be found via iterative reweighted least-squares (IRLS), with which the FOCUSS algorithm [59] is identified. A M-FOCUSS algorithm that extends FOCUSS to the MMV problem was introduced in [49].

The M-FOCUSS algorithm solves the problem

$$\min J^{(p,2)}(\boldsymbol{X}) \quad \text{subject to} \quad \boldsymbol{B} = \boldsymbol{A}\boldsymbol{X}. \tag{47}$$

In addition, it was also shown in [40] that sparse solutions can be obtained via an iterative reweighted ℓ_1 algorithm (IRL1), when minimizing a log-sum objective function. As a part of this research, the IRL1 algorithm is extended to the MMV case (M-IRL1) [54], which *iteratively* reweights the M-BP algorithm. The M-IRL1 algorithm solves the problem

$$\min J^{(0,1)}(\boldsymbol{X}) \quad \text{subject to} \quad \boldsymbol{B} = \boldsymbol{A}\boldsymbol{X}. \tag{48}$$

The following section examines the performance of these MMV algorithms.

3.2.2 Algorithm Performance – Noiseless

To assess the performance of each MMV algorithm, a simulation using *noiseless* measurements is conducted. Noisy simulations are considered in later sections that follow. Let $N = 20$, $M = 30$, and $L = 5$. The entries of the real-valued matrix $\boldsymbol{A}$ are independent and identically distributed standard Gaussian random variables. The multiple-measurement vectors are constructed by $\boldsymbol{B} = \boldsymbol{A}\boldsymbol{X}_0$ where $\boldsymbol{X}_0$ has K rows with nonzero entries. The locations of the K rows are selected uniformly at random, and the nonzero entries of $\boldsymbol{X}_0$ are drawn as in $\boldsymbol{A}$. An exact recovery is obtained when $\boldsymbol{X} \equiv \boldsymbol{X}_0$. The above simulation is repeated 500 times per MMV method. From the simulation result (Fig. 29), it is observed that M-FOCUSS ($p = 0$) and M-IRL1 have the highest empirical rate of exact recovery at different K. These two methods are further examined for estimating the DSRF.

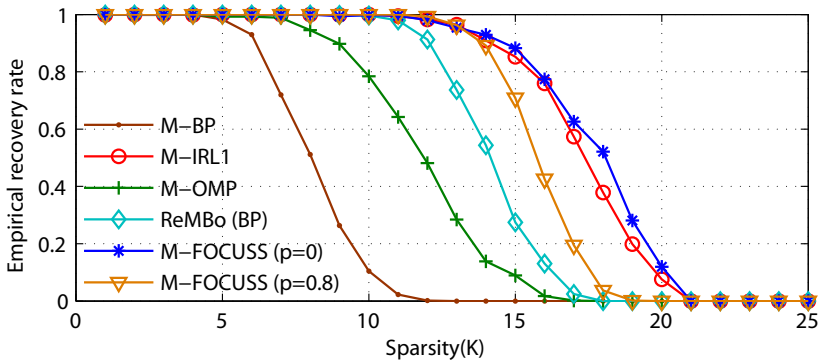

Figure 29: Performance of MMV methods for noiseless data.

3.2.3 M-IRL1 and M-FOCUSS

It is shown here for noiseless measurements, the special case of M-FOCUSS with $p = 0$ and M-IRL1 solve almost the same problem. The slight difference is in the choice of the row-norm $\mathcal{R}_{\ell_q}$, where M-FOCUSS uses an ℓ_2 row-norm and M-IRL1 uses an ℓ_1 row-norm.

The M-IRL1 algorithm [54] minimizes the log-sum objective

$$J^{(0,1)}(\boldsymbol{X}) = \sum_{m=1} \log\left(||\mathbf{x}_{\mathrm{m}}||_1 + \epsilon\right) \tag{49}$$

through an iteratively reweighted ℓ_1 algorithm. The formulation of the algorithm is developed in Appendix B. In short, the algorithm performs a series of ℓ_1 minimizations:

$$\begin{aligned} \boldsymbol{X}^{(i)} = \arg\min_{\boldsymbol{X}} ||\mathbf{W}^{(i)}\mathcal{R}_{\ell_1}(\boldsymbol{X})||_1 \quad \text{subject to} \quad \boldsymbol{B} = \boldsymbol{A}\boldsymbol{X}, \\ \text{where } \mathbf{W}^{(i)} = \mathrm{diag}[w_1^{(i)}, w_2^{(i)}, \ldots, w_{M+1}^{(i)}]. \end{aligned} \tag{50}$$

The weights are updated by

$$w_m^{(i+1)} = \frac{1}{||\mathbf{x}_{\mathrm{m}}{}^{(i)}||_1 + \epsilon}, \quad m = 1, \ldots, M+1. \tag{51}$$

On the other hand, the M-FOCUSS algorithm [53] minimizes the diversity measure

$$J^{(p,2)}(\boldsymbol{X}) = ||\mathcal{R}_{\ell_2}(\boldsymbol{X})||_p^p = \sum_{m=1} ||\mathbf{x}_{\mathrm{m}}||_2^p, \quad 0 \le p \le 1 \tag{52}$$

subject to $\boldsymbol{B} = \boldsymbol{A}\boldsymbol{X}$. By solving the Lagrangian derived from (52), an iterative reweighted *least squares* is obtained [53]:

$$\boldsymbol{X}^{(i)} = \tilde{\mathbf{W}}^{(i)}\boldsymbol{A}^{\mathrm{H}}(\boldsymbol{A}\tilde{\mathbf{W}}^{(i)}\boldsymbol{A}^{\mathrm{H}})^{-1}\boldsymbol{B}, \tag{53}$$

where $\tilde{\mathbf{W}}^{(i)}$ =diag$[\tilde{w}_1^{(i)}, \ldots, \tilde{w}_{M+1}^{(i)}]$, the superscript $^{\mathrm{H}}$ denotes the Hermitian transpose, and the weights are updated by

$$\tilde{w}_m^{(i+1)} = \left(||\mathbf{x}_{\mathrm{m}}{}^{(i)}||_2\right)^{p-2}. \tag{54}$$

When $p = 0$, the weight is $\left(||\mathbf{x}_{\mathrm{m}}{}^{(i)}||_2\right)^{-2}$, and M-FOCUSS is, in effect, minimizing

$$J^{(0,2)}(\boldsymbol{X}) = \sum_{m=1} \log ||\mathbf{x}_{\mathrm{m}}||_2, \tag{55}$$

which is very similar to the objective of M-IRL1, $J^{(0,1)}(\boldsymbol{X})$. This is true because, it can be readily shown, the partial derivative of $J^{(0,2)}(\boldsymbol{X})$ with respect to $x_{m,l}$ is

$$\begin{aligned}\frac{\partial J^{(0,2)}(\boldsymbol{X})}{\partial x_{m,l}} &= \frac{\partial}{\partial x_{m,l}} \sum_{m=1} \log \left(\sum_{l=1}^{L} x_{m,l}^2 \right)^{1/2} \\ &= ||\mathbf{x}_{\mathrm{m}}||_2^{-2} \, x_{m,l},\end{aligned}$$

and when substituted into the derivation of M-FOCUSS in [53], the coefficient of $x_{m,l}$, $||\mathbf{x}_{\mathrm{m}}||_2^{-2}$, is identified with the update weight, which is the same as the weight in (54) with $p = 0$. That is, by iterating (53) using the update equation (54) with $p = 0$, the M-FOCUSS algorithm effectively minimizes a log-sum objective.

The M-FOCUSS algorithm with $p = 0$ and M-IRL1 are *almost* equivalent except that M-FOCUSS uses $\mathcal{R}_{\ell_2}$ ($q = 2$), whereas M-IRL1 is derived using $\mathcal{R}_{\ell_1}$. However, the choice of q for the row-norm should not make a significant difference because the log-sum behaves similar to the ℓ_0 quasi-norm, which counts the number of nonzero elements regardless of the magnitude. Indeed, Chen and Huo [47] showed that under certain conditions, the row-norm can be *any arbitrary vector norm*, and the problem min $||\mathcal{R}_{\ell_q}(\boldsymbol{X})||_0$ (45) can be solved exactly by solving the problem min $||\mathcal{R}_{\ell_q}(\boldsymbol{X})||_1$ (46).

3.2.4 Regularization

To account for noise in the measurements and modeling error, regularized versions of M-FOCUSS and M-IRL1 are used. To regularize M-IRL1, the iterated minimization with an equality constraint in (77) is replaced with the following relaxed problem:

$$\boldsymbol{X}^{(i)} = \arg\min_{\boldsymbol{X}} ||\boldsymbol{A}\boldsymbol{X} - \boldsymbol{B}||_F + \lambda ||\mathbf{W}^{(i)} \mathcal{R}_{\ell_1}(\boldsymbol{X})||_1. \tag{56}$$

The regularization parameter λ balances the emphasis between the modeling error and the sparsity.

The regularized M-FOCUSS iteratively computes

$$\boldsymbol{X}^{(i)} = \tilde{\mathbf{W}}^{(i)} \boldsymbol{A}^{\mathrm{H}} (\boldsymbol{A} \tilde{\mathbf{W}}^{(i)} \boldsymbol{A}^{\mathrm{H}} + \lambda \mathbf{I})^{-1} \boldsymbol{B}, \tag{57}$$

where $\mathbf{I} \in \mathbb{R}^{N \times N}$ is the identity matrix [53].

Since regularization effectively loosens the equality constraints, the regularized algorithms can accommodate actual relaxation frequencies that are *not* in the dictionary. Simulations are performed to assess the performance of each regularized algorithm in the presence of noise. Comparisons between the two algorithms are shown in Section 3.3.3 along with other numerical simulations.

3.3 MMV Simulations with Synthetic Data

Simulations are conducted to verify the validity of the proposed MMV method and to gain understanding of its behavior under various conditions. Simulations demonstrated here include a four-relaxation target (Section 3.3.1), the performance of MMV vs. SMV (Section 3.3.2), performance comparison between different solvers (Section 3.3.3), and performance comparison for various number of measurements L (Section 3.3.4).

In Section 3.3.3, M-FOCUSS ($p = 0$) is found to be robust and fast to solve the regularized MMV optimization problem (34). Thus, for the rest of the work, unless otherwise specified, M-FOCUSS ($p = 0$) is assumed to be the MMV solver. The regularization parameter λ chosen by a simple function of SNR is described in Section 3.6.

3.3.1 Synthetic Four-relaxation DSRF

The proposed MMV method is tested using a four-relaxation DSRF synthesized at 60 dB SNR with additive white Gaussian noise. The spectral amplitudes are assigned according to an uniform distribution between -1 and 1. Ten measurements ($L = 10$) are used. The estimation result using M-FOCUSS is shown in Fig. 30. The relaxation frequencies ζ as well as the spectral amplitudes are correctly recovered. All samples share the same estimated ζ because of the sparsity-promoting term $J^{(p)}(X)$. The average estimation error (EMD) is 0.014 decades.

The same set of data is also processed using one measurement per estimate (SMV). The result is shown in Fig. 31 where the SMV estimates are seen to have more variation in the estimated ζ. The averaged EMD is 0.035 decades, which is still quite low.

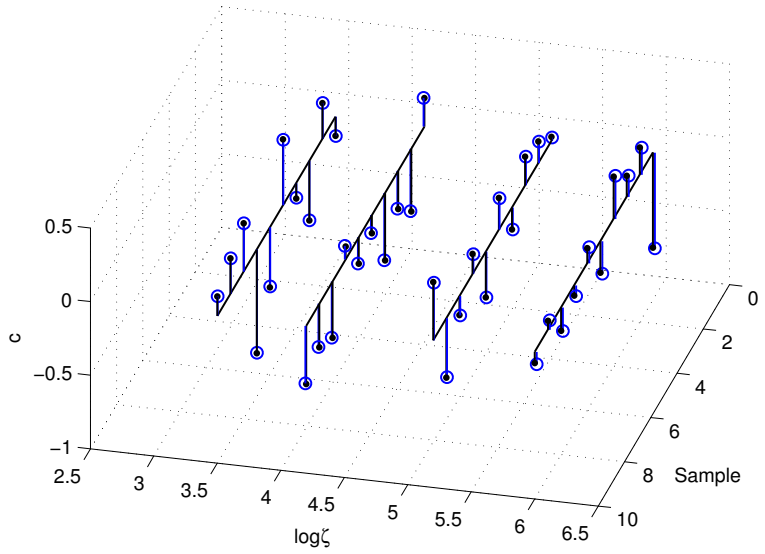

Figure 30: Theoretical and MMV-estimated DSRF of a four-relaxation target. The solid lines indicate the true relaxation frequencies. The stems with solid dots are the actual spectra; stems with hollow circle markers are the estimates.

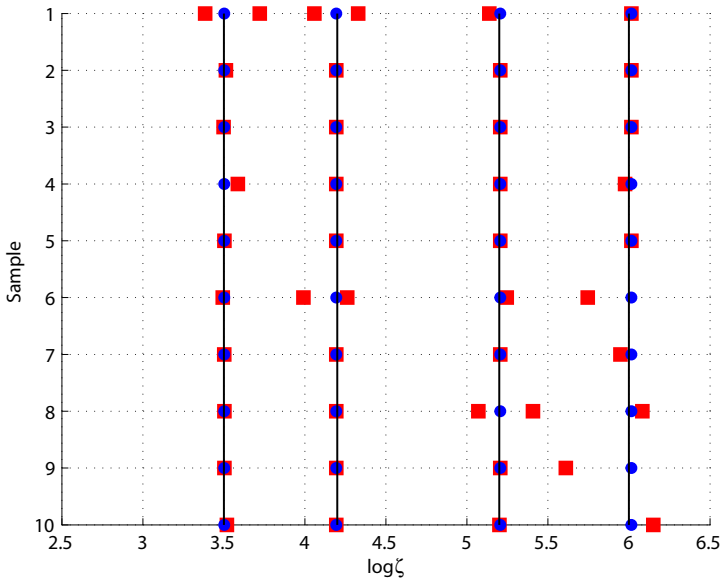

Figure 31: Theoretical and estimated DSRF of a four-relaxation target. Blue circles are the MMV estimates; red squares the SMV estimates.

3.3.2 Performance vs. Signal to Noise Ratio

To study how the proposed method performs in noise, a Monte Carlo simulation is performed. The true spectrum is from a target with a four-relaxation DSRF including negative relaxation coefficients c_k. A set of L measurements is synthesized using the same four

relaxation frequencies randomly distributed in $[\omega_1,\ \omega_N]$. The spectral amplitudes are randomly generated but constrained to have the same sign per relaxation frequency ζ_k. This sign constraint improves the results for the SMV method, because the L measurements are averaged together to get the SMV data which increases its SNR.

Figure 32 shows the performance of the MMV and SMV methods using the synthesized measurements. The simulation is set up with L=10 measurements per trial and 1000 trials per SNR. The simulation result suggests that the MMV method has a significant advantage over the SMV approach even though the simulation is setup to favor the SMV method. Compared to the performance of the SMV method, the MMV gives a smaller EMD error by about half a decade at a given SNR.

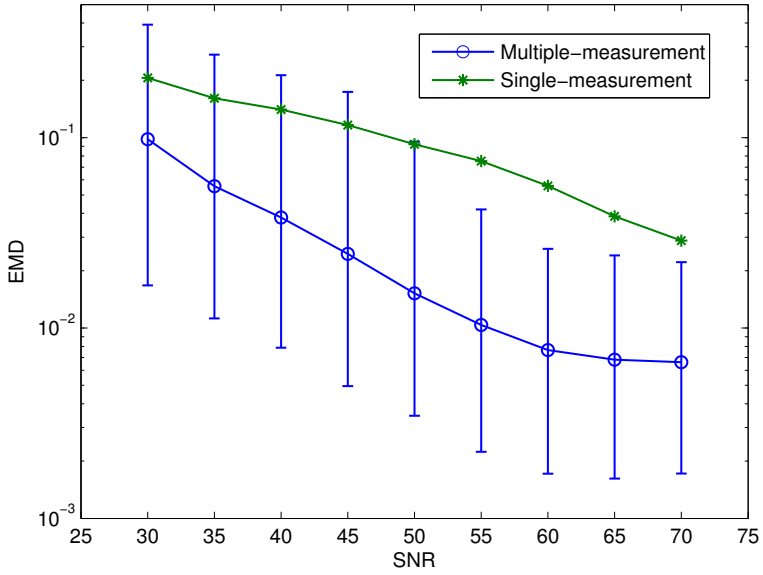

Figure 32: Monte Carlo simulation on goodness of estimation vs. SNR. The error bar indicates the 10th and 90th percentile.

3.3.3 Solver Performance Comparison

A simulation is conducted to examine the performance of two algorithms for solving the MMV problem: regularized M-FOCUSS and M-IRL1. The simulation is similar to the one in Section 3.3.2 but with $L = 20$ and $K = 4$. The Monte Carlo sample size is 1000 per SNR. The simulation result shows that M-FOCUSS on average delivers a lower estimation error than M-IRL1 (Fig. 33). In addition, from the recorded computation time (Fig. 34),

M-FOCUSS runs about 1000 times faster than M-IRL1. The computation time of both methods is observed to be independent of the SNR.

The M-IRL1 algorithm is implemented using the `CVX` package which implements convex optimization under MATLAB [60]. Because `CVX` implements a general convex optimization method, further speedup for M-IRL1 can be achieved via a customized implementation.

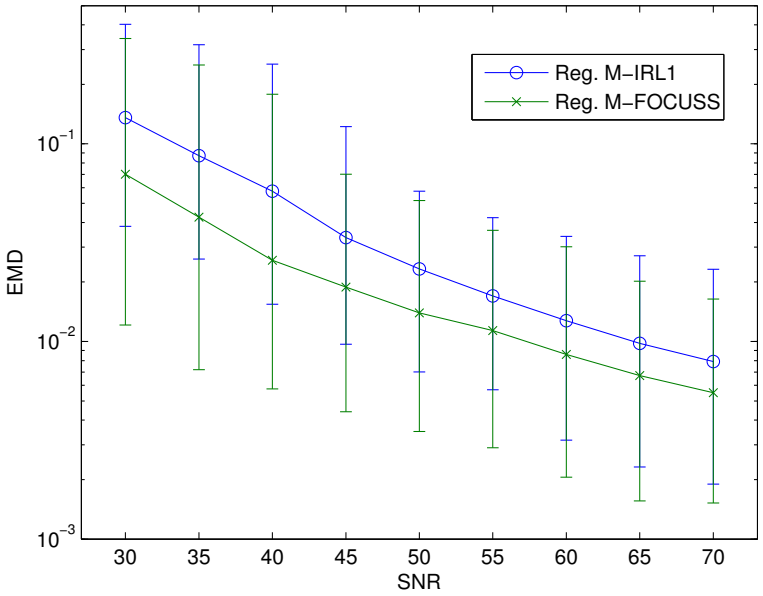

Figure 33: Monte Carlo simulation on goodness of estimation vs. SNR. $L = 20$ and $K = 4$. Sample size is 1000 per SNR.

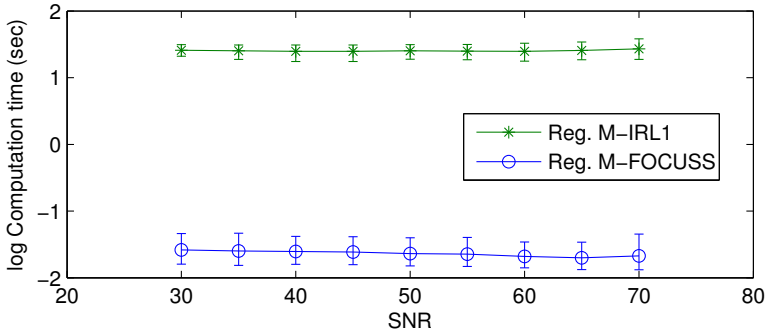

Figure 34: Monte Carlo simulation on computation time per estimation vs. SNR. $L = 20$ and $K = 4$. Sample size is 1000 per SNR.

In an earlier investigation of this research [54], a simulation similar to the one in Section 3.3.2 is performed, but the optimization problem is complex-valued, and the simulation uses relaxation frequencies that must be in the dictionary. That is, for any actual ζ_k there

exists a $\tilde{\zeta}_m$ such that $\zeta_k = \tilde{\zeta}_m$. Because the relaxation frequencies are in the dictionary, it is possible to exactly recover them even under noise. In this case, the performance is measured by the exact recovery rate. In [54] M-IRL1 is observed to have a higher probability than M-FOCUSS to exactly recover the relaxation frequencies. This is because in [54], M-FOCUSS is not constrained to consider only real-valued answers, which degrades its performance. On the other hand, M-IRL1 returns only real-valued solutions as a consequence of its implementation. In the simulation presented here, both methods are constraint to real-valued solutions by separating the real and imaginary part, as in (34).

3.3.4 Performance vs. Number of Measurements

When the estimation accuracy versus the number of measurements L is examined, it is observed that the estimation accuracy increases as L increases, which agrees with intuition (Fig. 35). The simulation performed here is similar to the one in Section 3.3.2, but the optimal regularization parameter is used instead of the near-optimum λ described later in Section 3.6. The intent is to examine the best possible performance for a given L. Because the differences in performance are small, the optimal λ is used to help differentiate the performance curves.

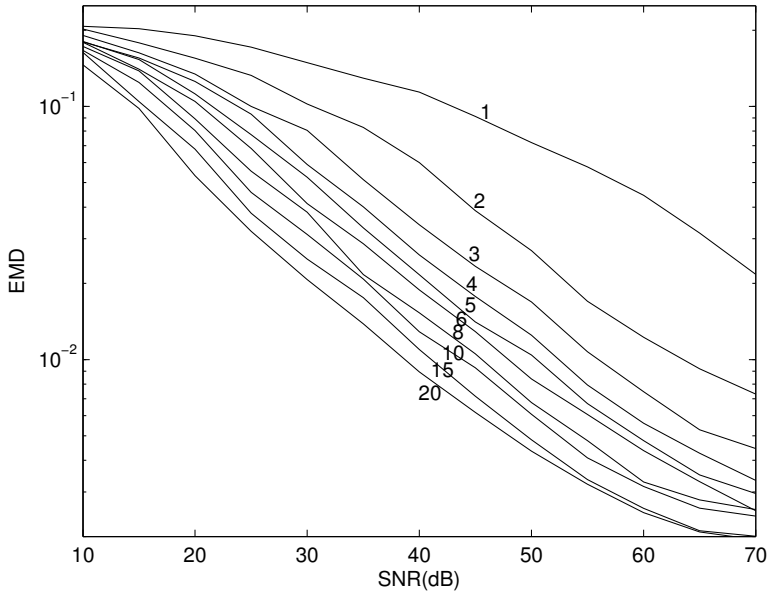

Figure 35: Monte Carlo simulation on estimation accuracy vs. SNR for different L, as annotated. The number of relaxations is $K = 4$. Sample size is 1000 per SNR.

3.3.5 Performance vs. p

A simulation is conducted to examine the estimation accuracy versus SNR for different choices of p, a parameter used in the cost function $J^{(p,q)}(\boldsymbol{X})$. From the simulation result (Fig. 36), it is observed that there is a significant performance difference between $p = 1$ and $p < 1$. This is different from the single-measurement case, where the performance of $p < 1$ is somewhat similar to that of $p = 1$ (Fig. 27). On the other hand, the performance of MMV improves significantly once p is less than 1.

The computation time versus SNR for different values of p are also recorded (Fig 37). It is interesting to note that the computation time is lower for lower values of p.

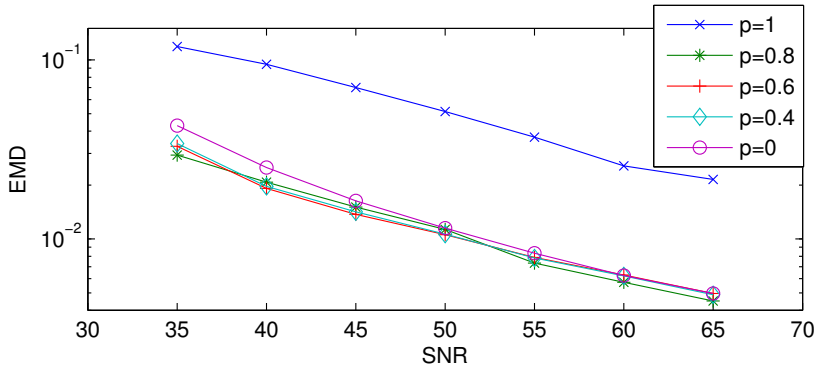

Figure 36: Monte Carlo simulation on estimation accuracy vs. SNR for different p values, as annotated. $K = 4$. Sample size is 1000 per SNR.

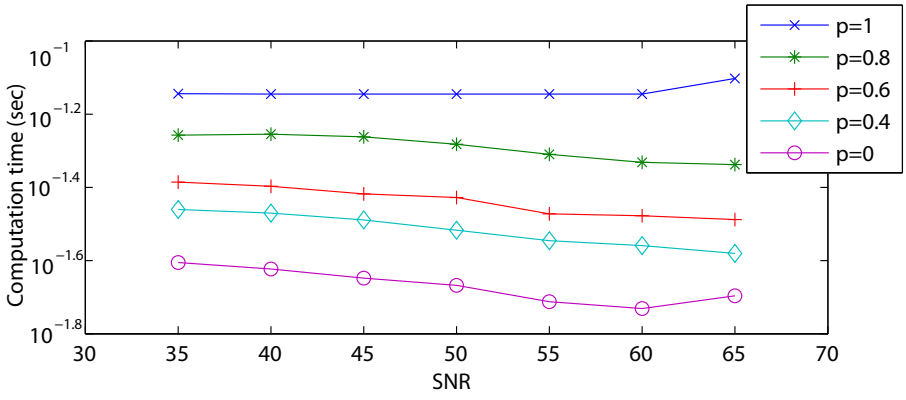

Figure 37: Monte Carlo simulation on computation time per estimation vs. SNR for different p values.

3.4 Laboratory Data

The functionality of the MMV estimation method is verified using laboratory data where the theoretical DSRF is available. An automated, non-metallic measurement facility is used to measure the EMI responses of a target at various positions and orientations relative to the sensor [44]. The proposed MMV method is observed to produce accurate estimates and is more robust than the single-measurement counterpart.

A target that consists of three mutually orthogonal copper loops is examined. The loop diameters and thicknesses are 3/20, 4/30, and 5/36, respectively in cm/AWG(American Wire Gauge). The target is configured at a fixed orientation and is displaced at different positions along a horizontal axis (x). The vertical distance between the target and the sensor is 5 cm. The EMI sensor is located at $x = 0$. The response of the target is measured at nine different x locations.

For the MMV method, these nine responses ($L = 9$) are used simultaneously to obtain an estimate of the DSRF. For the SMV method, a DSRF is estimated at each location. Improving the SNR by averaging the nine responses is not as effective for the laboratory data as it is for the synthetic data, because the spectral amplitudes are not constrained to be of the same sign and can cancel when averaged, lowering the SNR.

The estimates from these two methods are shown in Fig. 38. Both methods produce satisfactory estimates. However, the MMV method gives a more accurate estimate of the relaxation frequencies than the SMV. The estimates from the SMV have more variation in the relaxation frequencies and sometimes extra relaxations are introduced. The estimation error of the two methods is recorded in Table 1. The MMV method has a smaller averaged EMD of 0.127 decades than that of the SMV, 0.157 decades.

Table 1: Estimation error (EMD) of the three-loop target

x (cm)	-2	-1.5	-1	-0.5	0	0.5	1	1.5	2
SMV	0.1329	0.0741	0.3902	0.3762	0.1718	0.0948	0.0564	0.0724	0.0437
MMV	0.0750	0.0461	0.1716	0.3231	0.1915	0.1231	0.0886	0.0704	0.0505

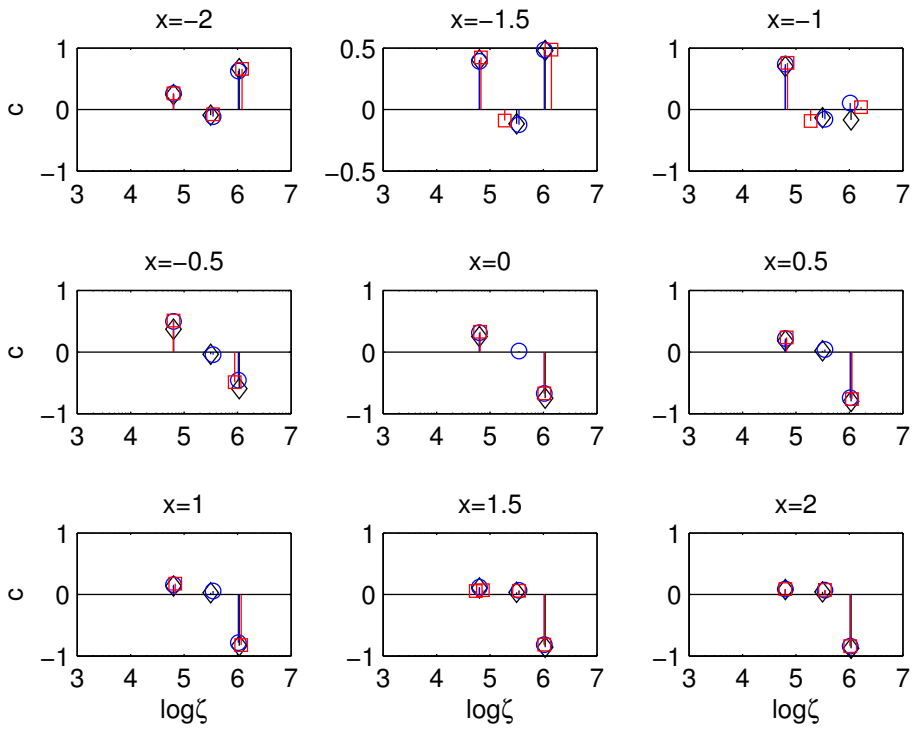

(a)

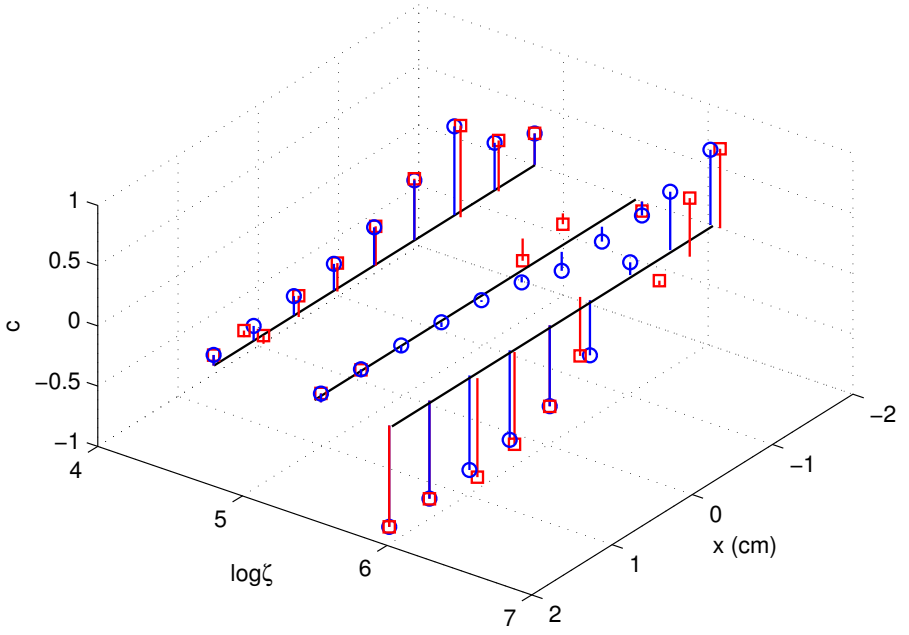

(b)

Figure 38: Estimation of the DSRF of the three mutually orthogonal copper loops at nine different x locations. (a) Black diamonds are the theoretical DSRF, blue circles the MMV estimates, and red squares the SMV estimates. (b) A 3D view of the estimated DSRFs that shows the consistent and accurate relaxation frequencies estimated by the MMV.

3.5 Field Data

The MMV method has also been applied to the field data where measurements are corrupted by various factors, including the soil and thermal perturbations. The field measurements used in this section are the same set of data used in Section 2.4, where targets are buried at various depths in grid cells. For DSRF estimation using multiple measurements, the ten strongest measurements in a grid cell are used ($L = 10$). Consistent DSRFs are observed for targets of the same type, indicating the functionality of the proposed MMV method. Ten types of targets are examined, and the DSRFs are estimated using the M-FOCUSS algorithm. For two types of targets, the M-IRL1 is also used for comparison.

Type-A and Type-B mines are modeled using both M-FOCUSS and M-IRL1. The description of the mines can be found in Section 2.4. These mines have moderate to strong EMI responses. The results of the estimated DSRF using these two solvers are shown in Fig. 39. Both methods provide stable DSRF estimates, but the estimates are slightly different. Because the actual DSRF is unknown for the field targets, it is not clear which solver returns more accurate estimates. Nevertheless, both solvers return self-consistent DSRFs that can be used as a feature for target discrimination. For Type-A mines, the average distance among the estimates are 0.047 decades for M-FOCUSS and 0.079 decades for M-IRL1. For Type-B mines, the average EMDs are 0.088 decades for M-FOCUSS and 0.091 decades for M-IRL1.

More results of the MMV DSRF estimation are shown in Fig. 40 and Fig. 41. As with the SMV case, the DSRFs obtained using the MMV method are, in general, consistent within a type. Some of the MMV-estimated DSRFs are the same as those obtained using the SMV method, such as the Type-W mines in Fig. 18(d) and Fig. 40(d). For some mines, such as the Type-V mines in Fig. 40(c), the MMV method seems to have a higher resolution and recovers more relaxations, which are observed in the SMV only when the SNR is higher. On the other hand, for targets like the Type-H mines, the MMV returns DSRFs that are slightly less consistent when compared to the SMV, even though the average EMDs are similar.

From the field data, the MMV method does not seem to show a significant improvement

in the consistency of the estimated DSRF when compared to the SMV method. This result is different from what is observed in the synthetic and laboratory data, where the MMV achieves a higher accuracy in the estimated DSRF compared to the SMV. Overall, in the field measurements the MMV does not produce more consistent DSRFs, nor does it produce less consistent DSRFs. The lack of the expected performance gain in the field measurements might be caused by the nonuniform SNRs across the measurements, which affects how the regularization parameter λ is chosen. In the following section, a more sophisticated λ selection scheme is proposed. For this section, it is sufficient to demonstrate the functionality and stability of the MMV DSRF estimation method.

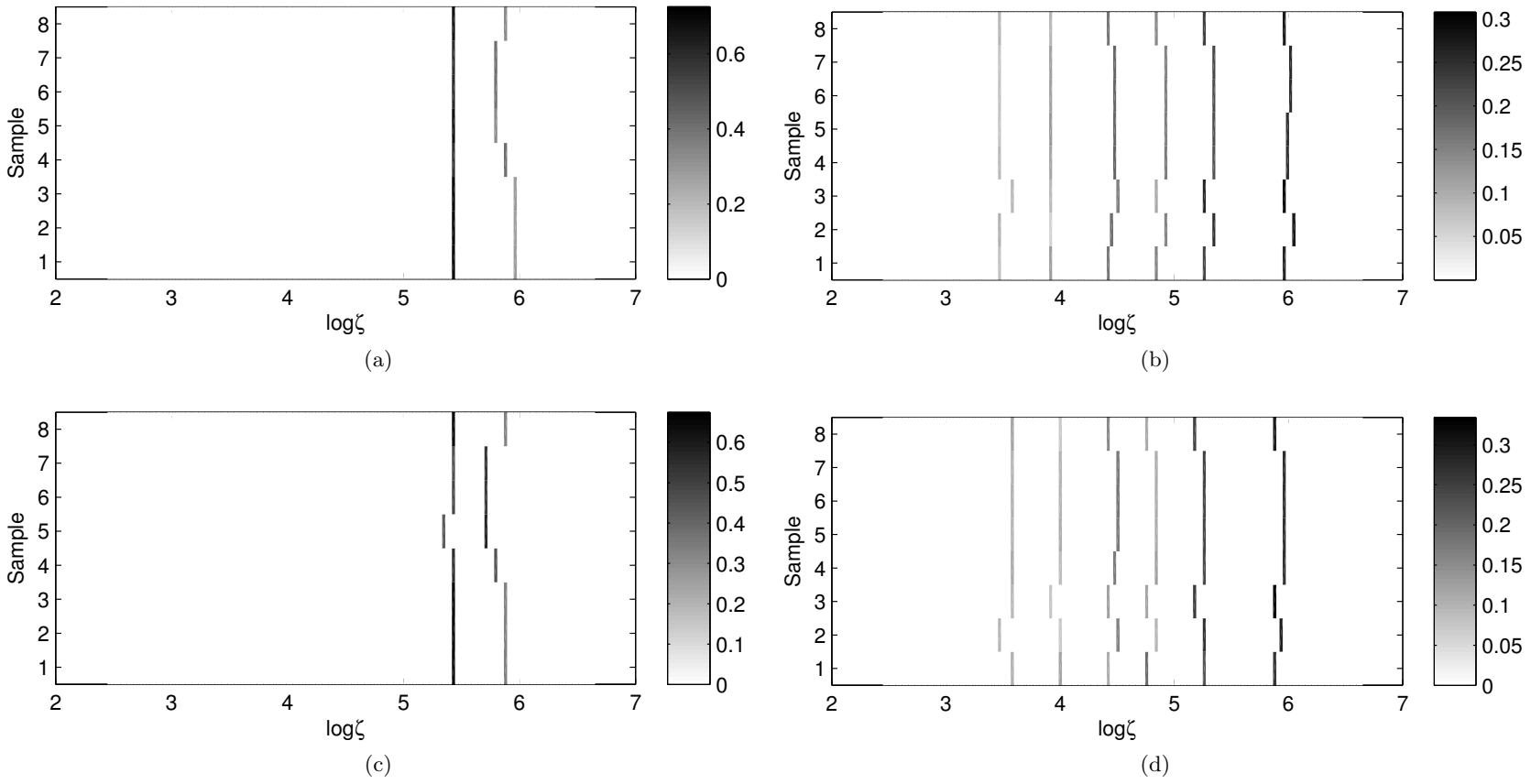

Figure 39: Estimated DSRFs of eight Type-A mines using (a) M-FOCUSS and (c) M-IRL1. The SNR ranges from about 45 dB to 60 dB. Estimated DSRFs of eight Type-B mines using (b) M-FOCUSS and (d) M-IRL1. The SNR ranges from about 55 dB to 70 dB.

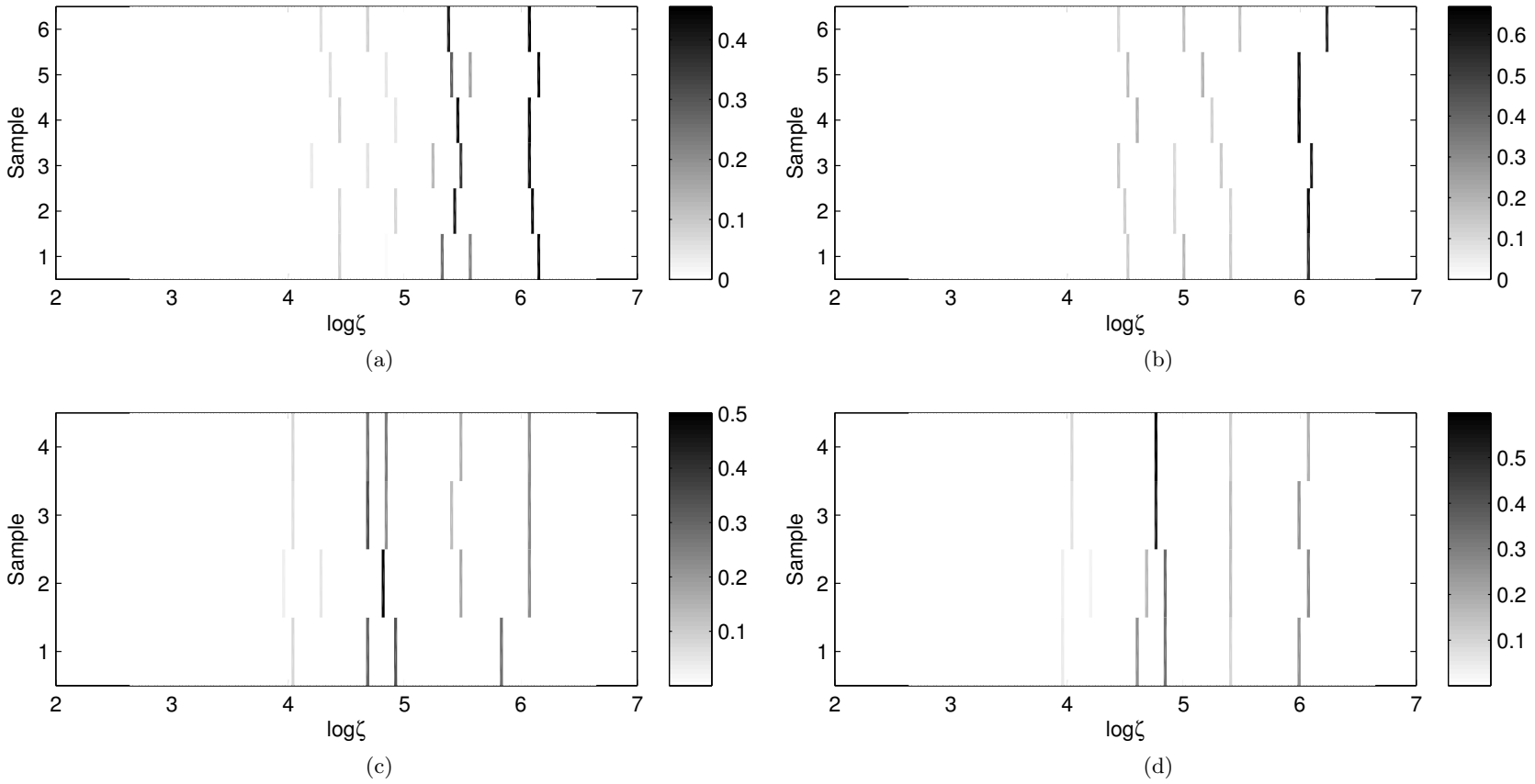

Figure 40: Examples of estimated DSRFs from field targets using MMV. The average EMD listed below are in decades and SNR in dB. (a) Six Type-H mines; EMD=0.098, SNR=47. (b) Six Type-I mines; EMD=0.16, SNR=39. (c) Four Type-V mines; EMD=0.13, SNR=42. (d) Four Type-W mines; EMD=0.14, SNR=44.

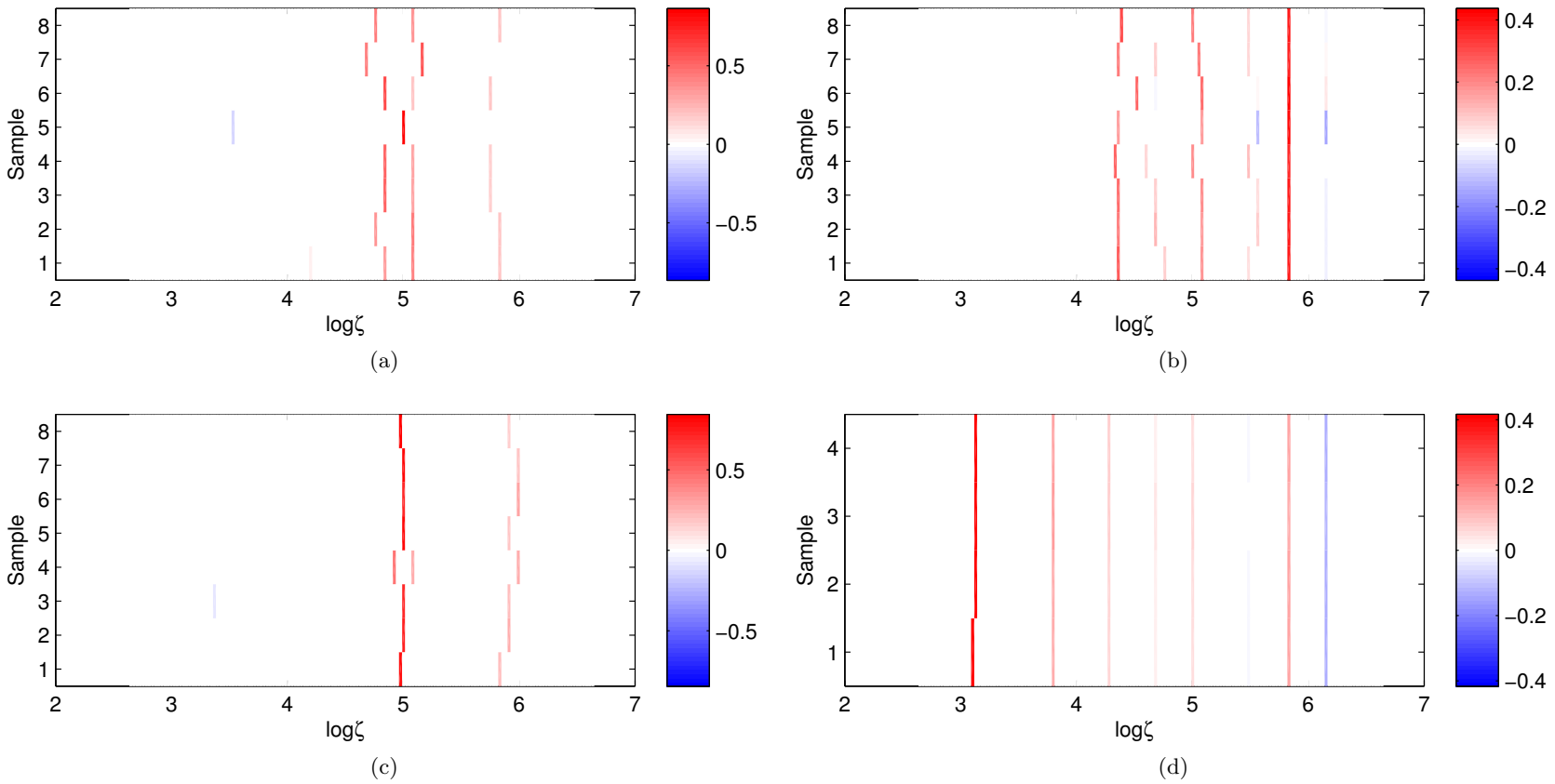

Figure 41: Examples of estimated DSRFs from field targets using MMV. The average EMD listed below are in decades and SNR in dB. (a) Eight Type-C mines; EMD=0.19, SNR=26. (b) Eight Type-D mines; EMD=0.13, SNR=82. (c) Eight Type-E mines; EMD=0.12, SNR=26. (d) Four Type-L mines; EMD=0.048, SNR=85.

3.6 Choosing the Regularization Parameter λ

A simulation is performed to optimally select λ via the trade-off between the modeling error and sparsity. The λ-SNR simulation for the MMV is similar to that of the SMV (Section 2.5), except that there is an additional parameter L to consider. For each L, the simulation is identical to the SMV.

As in the SMV case, it is observed that the optimal λ that gives the minimum estimation error is quasi-independent of the model order (Fig. 42). In addition, the EMD (estimation error) surfaces are well-behaved and smooth with respect to the SNR and λ. To obtain a λ-SNR relation independent of the model order, an average of the EMD surface across different model orders is taken (Fig. 43). The averaged surface is smooth and has a "wide valley" – indicating the estimation error is not sensitive near the optimal λ.

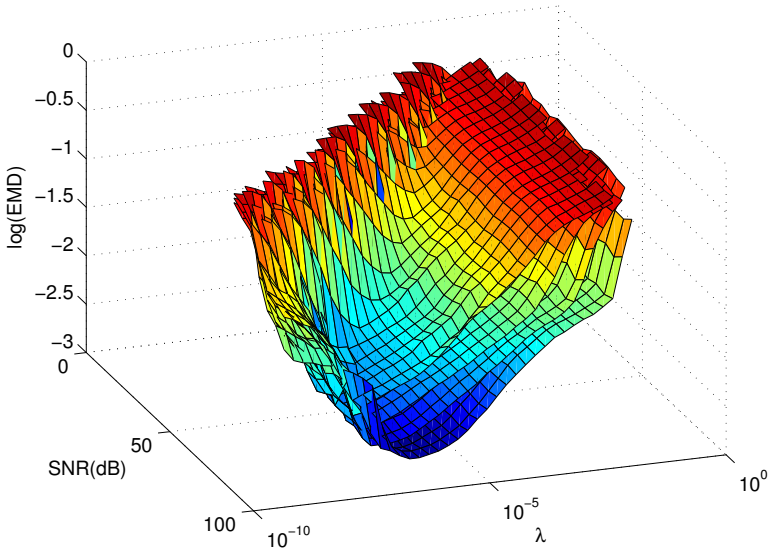

Figure 42: Monte Carlo simulation of the goodness of estimation (EMD) of spectra of different model orders. $L = 10$.

For the averaged surface, the λ at each SNR that gives the minimum EMD is roughly linear. For $L = 10$, a linear approximation of the optimal λ curve is

$$\log \lambda = -0.059 \cdot \mathrm{SNR} - 2.44 \tag{58}$$

Better approximations can be achieved through higher order polynomials or splines.

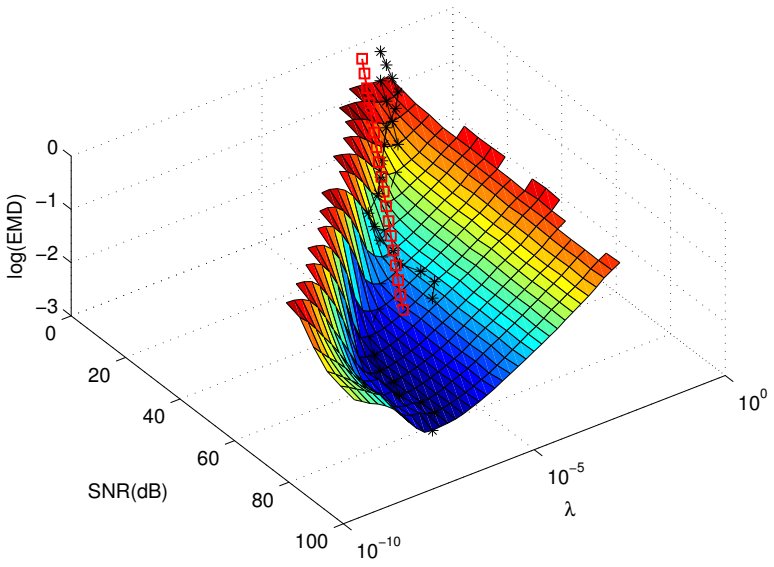

Figure 43: The average of EMD surfaces of various model orders, i.e., the average of the surfaces in Fig. 42. The curve with asterisk markers traces out the optimal λ's. The line with square markers approximates the optimal λ's. The number of measurements is $L = 10$.

The MMV λ selection is in fact more complicated than that of the SMV because measurements can have different SNRs. The simulation suggested above, however, assumes a uniform SNR across measurements. To bridge the gap between the uniform SNR simulation and the nonuniform SNR which occurs in practice, a simple mean-regularization-parameter $\bar{\lambda}$ can be used. That is,

$$\log \bar{\lambda} = \frac{1}{L} \sum_{l=1}^{L} \log \lambda_l = \frac{1}{L} \log \prod_{l=1}^{L} \lambda_l, \tag{59}$$

where λ_l is the regularization parameter for l^{th} measurement. This mean-λ works well when the SNRs do not vary drastically, and it is demonstrated in the field data the functionality of this method.

A more comprehensive λ-SNR simulation can be performed to account for the varying SNRs, which may lead to more consistent field DSRF estimates. Two factors can be included in the current simulation setup. The first is to assign the multiple measurements with a nonuniform distribution of signal power while keeping the noise power constant. A reasonable distribution could be parabolic-shaped, which resembles the signal power distribution in the recorded field measurements (e.g., Fig. 15). The second factor is the soil response in the simulation. Either synthesized or field-measured soil responses can be considered.

CHAPTER IV

TARGET DISCRIMINATION

The concept of discriminating targets based on the relaxations of a target is well known [5, 12], but the inability to obtain good DSRF estimates has been a limiting factor [30]. Using the DSRF estimation methods developed in this work, it is now possible to discriminate targets based on the DSRF.

Recall that the EMI response of a target can be modeled by the expression

$$H(\omega) = c_0 + \sum_{k=1}^{K} c_k \frac{1 - j\omega/\zeta_k}{1 + j\omega/\zeta_k}, \tag{60}$$

where the relaxation frequencies ζ_k are intrinsic to the target and are invariant with respect to orientation and location. The relaxation frequencies naturally serve as a good signature or fingerprint for a target. The spectral amplitudes c_k change with respect to orientation and location, so the c_k are usually not a ideal signature. However, in the case of landmine targets, most landmines are buried at fixed orientations so the changes in c_k are consistent.

In this work, the strategy is to use both the relaxation frequencies and the spectral amplitudes for target discrimination, i.e., use the DSRF $S = \{(\zeta_k, c_k) : k = 1 \dots K\}$. The methods developed in this chapter can be readily adjusted to discriminate targets using only the relaxation frequencies by replacing the spectral amplitudes with a constant. This constant should be normalized such that $\sum_{k=1} c_k = 1$.

To visualize how target discrimination based on the DSRF is possible, consider the plots shown in Fig. 44 for several instances from two types of landmine. It is clear the two mine types have very different DSRF fingerprints – Mine Type-A has two relaxations and Mine Type-B has six relaxations. In addition, the spectral amplitudes for each type of mine are self-consistent. Therefore, it is possible to differentiate the types of targets based on the DSRF. More examples of targets exhibiting different DSRFs can be found in Section 2.4 and 3.5. While multi-class classification is possible, in this chapter only two classes, landmine and non-landmine, are considered to give a working example of DSRF-based discrimination.

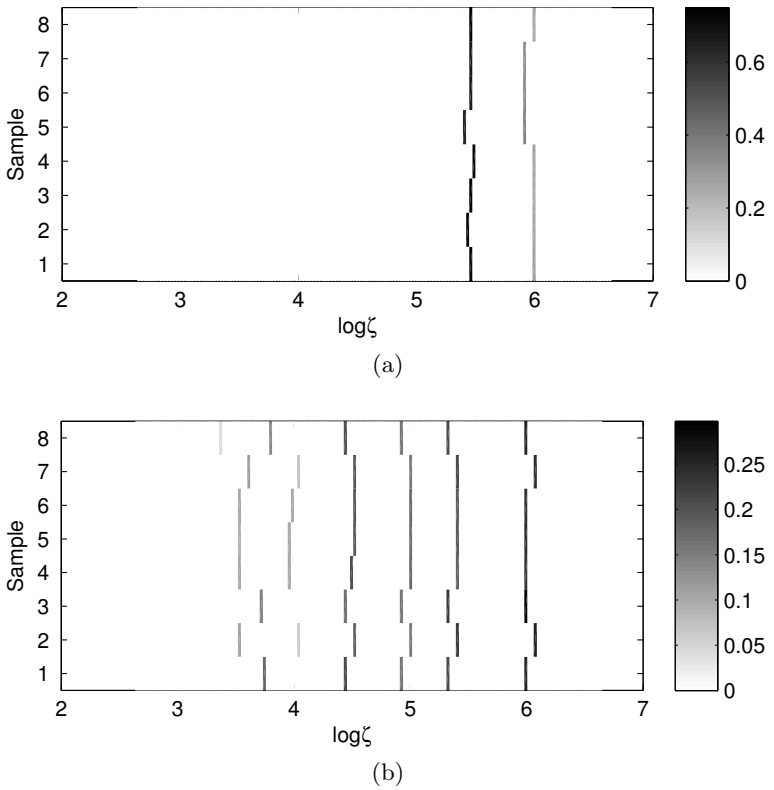

Figure 44: Estimated DSRF of real landmines. The spectral amplitude is represented by the intensity: darker the gray, larger the amplitude. (a) Eight Type-A mines: low metal content, nonmagnetic, and moderate EMI response antipersonnel mines. (b) Eight Type-B mines: medium metal content, magnetic, and strong EMI response antipersonnel mines.

To quantify the dissimilarity between two spectra, the Earth Mover's Distance (EMD) is used. For example, the EMD can be used to quantify the distance between Type-A and Type-B mines by averaging the distance between all pairs of DSRF from the two types. This can be done for instances from all types of mine available as well as clutter objects. By doing so, a similarity map is obtained (Fig. 45). The similarity map is a symmetric matrix of EMD between all pairs of DSRFs. The diagonal is zero because that is the EMD between a DSRF and itself which is zero.

The map shows that, in general, mines of the same type are similar to each other, as indicated by the dark blocks on the diagonal. On the other hand, targets of different types are dissimilar, indicated by the white color off-the-diagonal. More importantly, landmines are, overall, different from the clutter, and this suggests that landmine and clutter discrimination is possible using the DSRF.

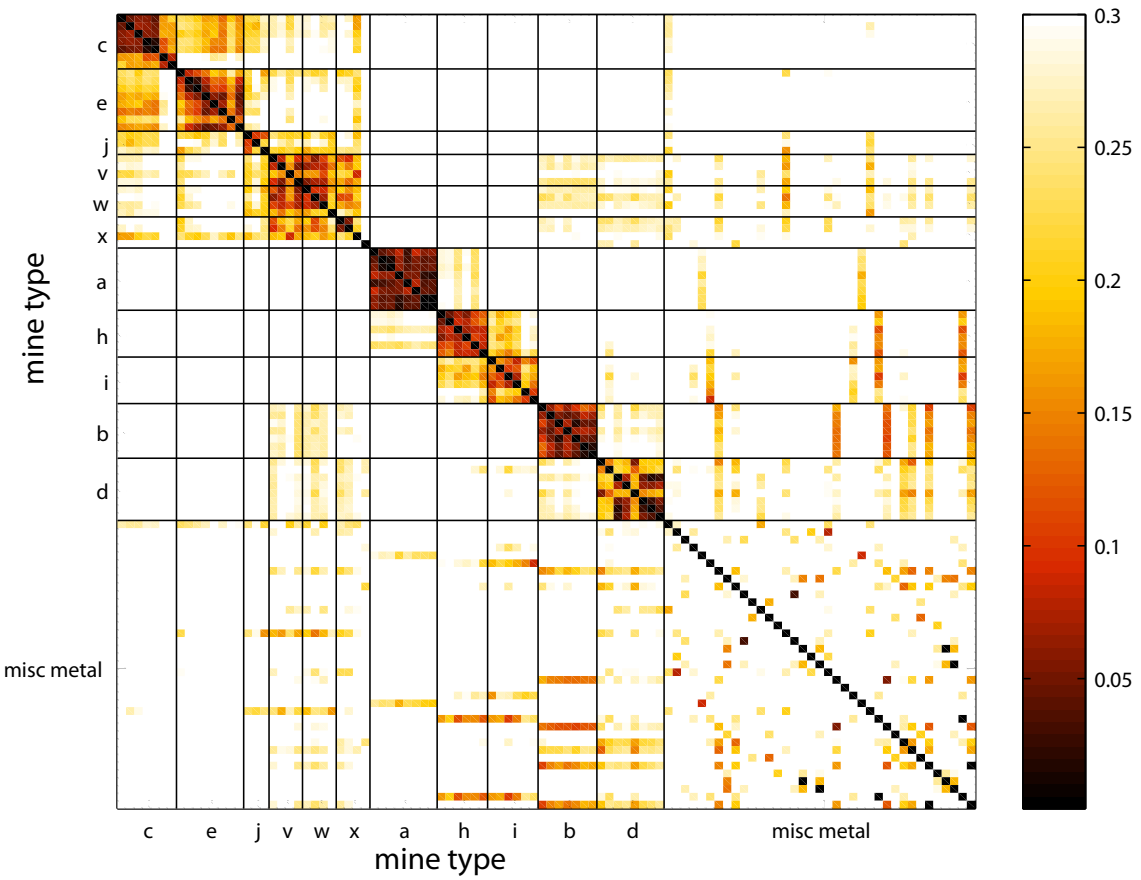

Figure 45: The EMD between samples from about one hundred independently measured field landmines of eleven types and various metal clutter. Darker colors denote smaller distances which indicate that two samples are more similar.

To discriminate targets using the DSRF, the k-nearest neighbor (kNN) algorithm and the support vector machine (SVM) are considered to classify targets. The EMD plays a key role in formulating these DSRF classifiers. These classifiers are presented in Section 4.1.1.

To aid real-time, on-the-field, target discrimination, a model-based soil prescreener is introduced to identify the presence of metallic objects. The DSRF estimation and classification are only performed when a target is present. The soil prescreener is discussed in Section 2.4.2.

The classifier and soil prescreener are incorporated in a landmine detection framework developed in Section 4.1.3. Lastly, the performance of the framework, utilizing the DSRF classifiers and the prescreener, is examined and compared to existing detection techniques in Section 4.2.

4.1 Detection Methods

4.1.1 Target Classifiers

Two DSRF-based target discrimination techniques using the kNN and the SVM are developed here. With only two classes, landmine and not-landmine, the classification problem reduces to a detection problem.

The kNN predicts the class of a target based on the labels of its closest k neighbors. In the case of the kNN, the distance measure used to quantify the similarity between two DSRFs is the EMD. The Euclidean distance is a poor measure of the similarity between the two DSRF because the relaxations of two DSRFs are usually sparse and not aligned, as discussed in Section 2.2.1.

In the case of the SVM, given a target's DSRF parameter set S, the target is classified/labeled using the decision function

$$f(S) = \text{sign}\left(\sum_{i=1} \alpha_i y_i \mathbf{K}(S_T^i, S) + \beta\right), \tag{61}$$

where $\mathbf{K}$ is the kernel (explained shortly), S_T^i the training data, $y_i \in \{-1, +1\}$ the training class labels, α_i the trained weights, and β the trained threshold. Only a few α's are nonzero, i.e., the α's are sparse. The S_T^i that correspond to the nonzero α_i are called the *support vectors*.

For the kernel, a generalized radial basis function based on the EMD is used [61]:

$$\mathbf{K}_{\text{EMD}}(S_1, S_2) = \exp(-\rho\,\text{EMD}(S_1, S_2)), \tag{62}$$

where ρ is a scaling parameter. For brevity, (62) is called the EMD kernel [62]. While it has not been possible to prove that the EMD kernel satisfies Mercer's condition, i.e., $\mathbf{K}_{\text{EMD}}$ is positive semi-definite, it is observed that the EMD kernel is positive semi-definite in practice [62]. Furthermore, it should be noted that kernels that do not satisfy Mercer's condition can still perform well [61].

4.1.2 Soil Prescreener

A soil prescreener based on the soil model (21) is presented here. The prescreener filters out responses that are like those due to the magnetic properties of the soil. This reduces the

computation cost in unnecessary DSRF estimation. The prescreening process is performed very efficiently via a linear least-squares minimization.

In Section 2.4.2, a soil model is proposed based on the log-linear trend in the soil frequency response:

$$H_G(\omega) = p_1 + p_2 \left(\ln \omega + j \frac{\pi}{2} \right), \tag{63}$$

where p_1 and p_2 are model parameters. The real part has a linear trend with respect to the log-frequency, and the imaginary part is a constant. Recall that for a soil response $\boldsymbol{b}_G$ measured at N frequencies,

$$\boldsymbol{b}_G = \mathbf{G}\mathbf{p} + \mathbf{noise} \qquad , \tag{64}$$

where

$$\mathbf{G} = \begin{bmatrix} 1 & \ln \omega_1 + j\pi/2 \\ 1 & \ln \omega_2 + j\pi/2 \\ \vdots & \vdots \\ 1 & \ln \omega_N + j\pi/2 \end{bmatrix} \qquad \text{and} \qquad \mathbf{p} = \begin{bmatrix} p_1 \\ p_2 \end{bmatrix}.$$

Using the system of equations (64), a measured soil response can be fitted efficiently via a least-squares minimization:

$$\boldsymbol{b}_{G,\mathbf{fit}} = \boldsymbol{G}(\boldsymbol{G}^{\mathrm{H}}\boldsymbol{G})^{-1}\boldsymbol{G}^{\mathrm{H}}\boldsymbol{b}_{\mathbf{G}}. \tag{65}$$

The magnitude and residual of soil responses for 6000 samples collected at locations that are reported to have no metal content are shown in Fig. 46. Some magnitudes are strong ($> -125\,\mathrm{dB}$) because metal targets were actually present nearby. For most samples, the magnitude of the modeling residual is noticeably smaller than the response, indicating that the samples fit the soil model well. Ground responses that do not fit well, i.e., have high residuals, often occur when strong metallic objects are near by.

Because the model describes a behavior very specific to the soil, the model can be used as a prescreener to determine whether a target is present based on the fitting residual. Given a frequency response, the response is fitted to (63) using (65) and the fitting residual ϵ is compared with a threshold θ to determine whether a metallic object is present:

$$\text{target present} = \begin{cases} \text{true} & \text{if } \epsilon > \theta \\ \text{false} & \text{otherwise.} \end{cases} \tag{66}$$

A reasonable choice of θ for our measurement is $-135\,\mathrm{dB}$, as suggested by Fig. 46.

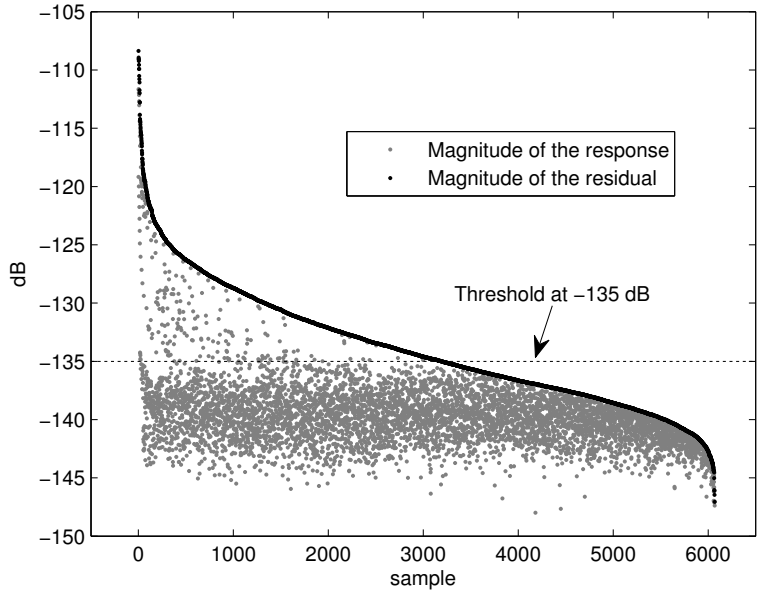

Figure 46: Samples of blank responses fitted to the soil model (21). The samples are ordered so that response decreases with increasing sample number.

4.1.3 Detection Framework

A detection framework that incorporates the soil prescreener and the target classifier is presented here. The framework is designed to be suitable for practical applications where measurements are acquired sequentially in real-time. It is designed according to the scenario where a detection vehicle carrying the EMI sensors is driven forward and EMI responses $\boldsymbol{b}_n$ are collected sequentially.

The prescreener first screens out the responses that are absent of metallic objects. Responses that pass the prescreener, indicating a target is present, are then processed to estimate their DSRFs. Based on the estimated DSRF, the classifier then labels the responses as landmine or not-landmine. The use of the prescreener significantly reduces the amount of data processed by the DSRF estimator and the target classifier. Because the prescreener takes very little computation time compared to the estimator and the classifier, the average computation time is also greatly reduced by using the prescreener.

A simple voting mechanism is employed to discourage temporary mislabeling of landmines by taking advantage of the sequential measurements. As the detection vehicle passes

over the target, often multiple measurement are collected consecutively for that target. In this case, multiple labels x_i are produced, and a more confident decision can be made based on the recent labels. A landmine is determined to be present only when p out of the past q labels are marked as landmine. The voting rule reduces the false-alarm rate and increases the confidence level.

The proposed framework is summarized below and a flow chart is shown in Fig 47.

Detection Framework

Input: $\boldsymbol{b}_n$, θ , p, $x_{n-q+1} \dots x_{n-1}$
Output: decision$_n$

Fit $\boldsymbol{b}_n$ to soil model (21) and obtain residual ϵ.
if $\epsilon < \theta$ **then**
    $x_n = 0$
else
    $\hat{S}$ = estimated DSRF of $\boldsymbol{b}_n$
    x_n = classify($\hat{S}$) (0 or 1)
if $\sum_{i=n-q+1}^{n} x_i > p$ **then**
    decision$_n = 1$
else
    decision$_n = 0$
return decision$_n$

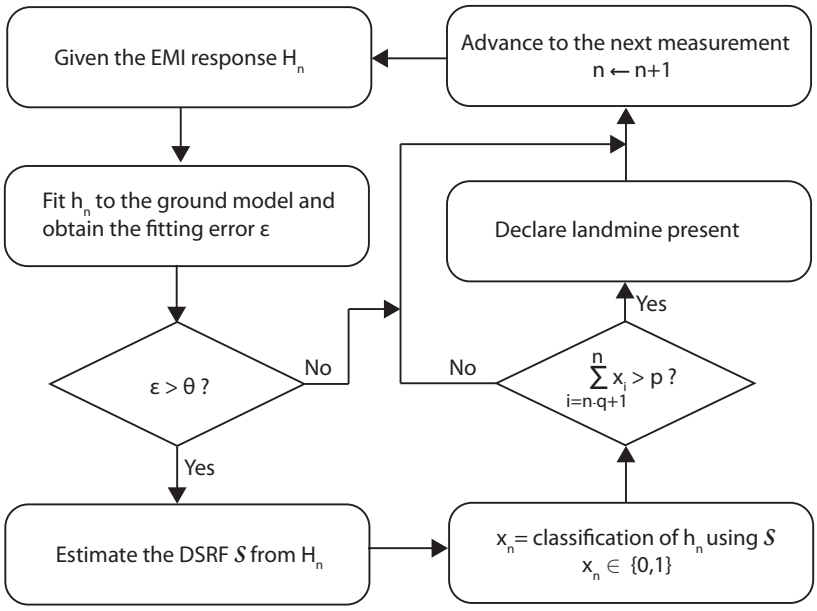

Figure 47: Flow chart of the detection framework.

4.2 Performance

The proposed method is applied to a data set acquired from a testing field that contains 26 types of landmines and various types of metallic and nonmetallic clutter. The field is divided into 220 grid cells where targets are buried. This is the same testing field described in Section 2.4. About 145 EMI responses are collected per grid cell. In total, 32,148 responses are collected for the whole field. The acquisition hardware used is described in [8].

The EMI responses are collected sequentially as the detection vehicle is driven down the lane, and the responses are fed into the detection framework described earlier. The parameters are chosen such that $p = 10$, $q = 20$, and $\theta = -135\,\text{dB}$. A snapshot of the output of the framework is shown in Fig. 48. Because the responses are filtered [8], a target response has multiple lobes,e.g., grid 71 to 74.

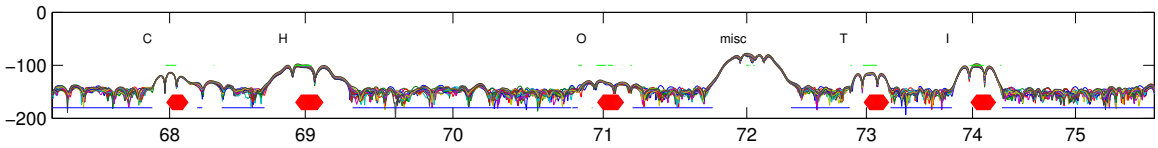

Figure 48: A snapshot of the output of the detection framework. The labels on the horizontal axis indicate the grid numbers, and the vertical axis is the response magnitude in dB. The curved lines are the strength of the responses measured at 21 frequencies. The target types are noted above the grid number. The blue lines (near -200 dB) indicate points that are marked as soil; black dots (at -100 dB) indicate points that are labeled as landmines; red diamonds indicate a declaration of landmine.

In Fig. 48, it is seen that the soil prescreener is quite effective and the voting rule reduces false alarms. In grid 72, a miscellaneous clutter is labeled as a landmine for a few times, but because the number of mislabels is small ($< p$), a landmine is not declared and a false alarm is avoided.

More output of the detection framework is shown in Fig. 49, where multiple lanes are displayed. In general, landmines are correctly detected, labeled by the red diamonds, the soil-only responses are correctly identified, indicated by the blue lines, and the metallic clutters are correctly classified. In grid 66, the target is weak and is screened out by the soil prescreener. Upon close examination, this target has a soil-like frequency response.

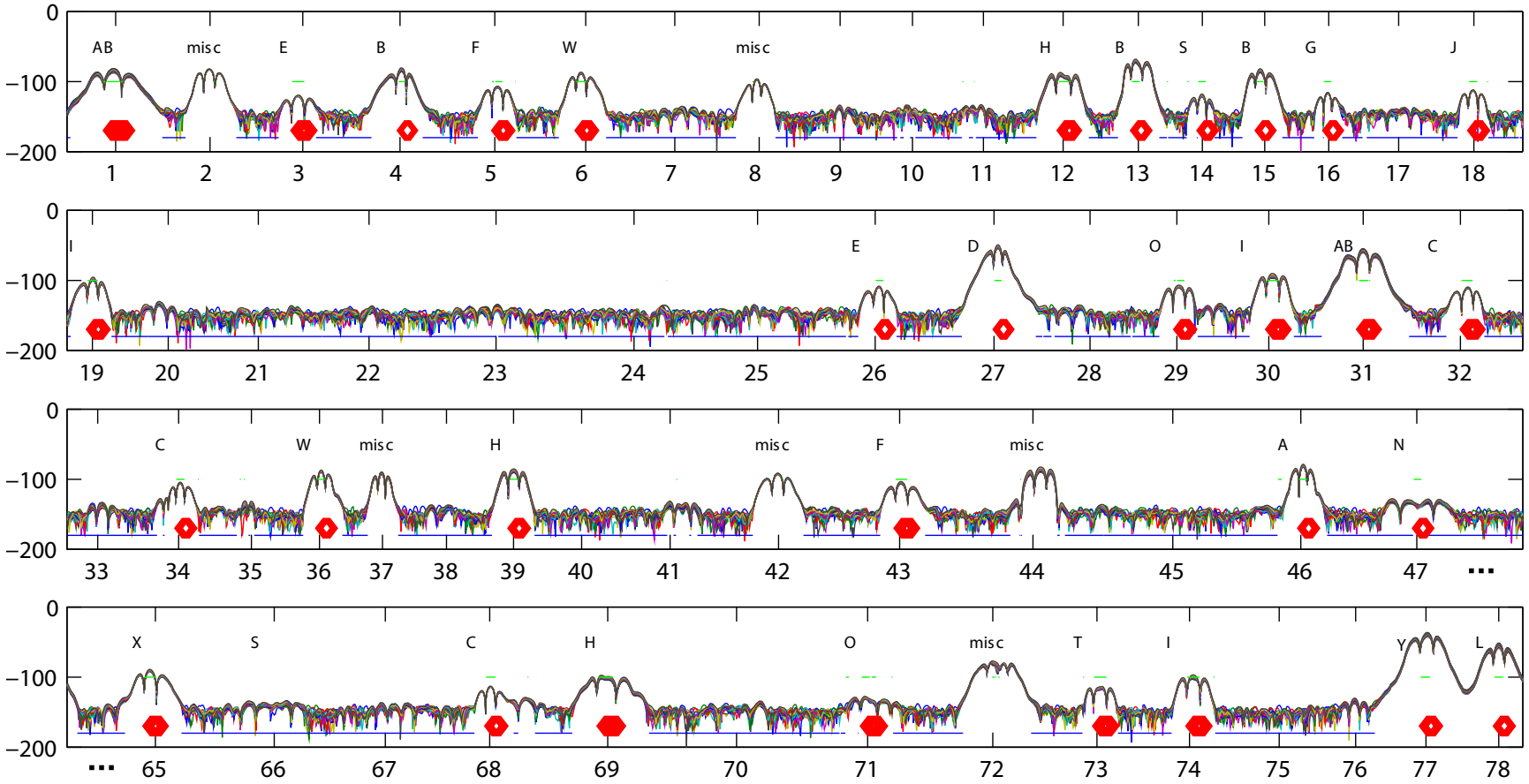

Figure 49: Output of the detection framework when applied to multiple lanes. The notation is the same as in Fig. 48.

The performance of the detection framework using the SVM is summarized in Fig. 50. The receiver operating characteristic (ROC) curve achieves a high detection rate of 0.96 at a low false-alarm rate of 0.10. Other operating points also provide satisfactory performances.

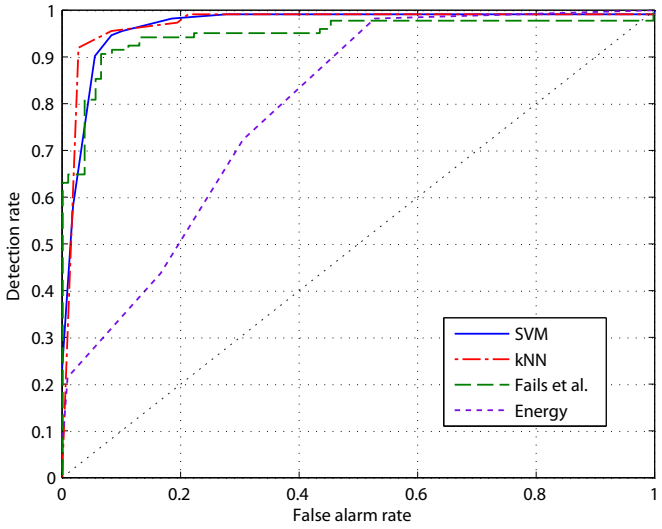

Figure 50: ROC curves of the proposed method and that of Fails *et al.*. For the kNN ROC curve, $k = 7$.

The detection process does not take much computer time. With a single pre-trained SVM, the whole test field (32,148 responses) can be classified using the above process, including estimating the DSRF, in 30 seconds on a 2.66 GHz CPU with 960 MB RAM.

The performance of the detection framework using the kNN is also shown in Fig. 50. The performance is comparable to that of the SVM. However, the processing time is much longer (10+ minutes) due to the many distance computations required to find the nearest neighbor per measurement. While the kNN may not be suitable for real-time application, it is quite robust when sufficient training data are available, as is the case here. When training data are scarce, the SVM is likely to have smaller generalization error.

The classifiers are trained per grid cell using a leave-one-out cross-validation (LOOCV), i.e., the classifiers are trained at each grid cell using responses from other grids cells. Only the strongest responses in a grid cell are used for training. Grid cells containing only soil are excluded in the training process.

The performances of the DSRF-SVM and DSRF-kNN are compared to the detection performance of a simple energy detector, also shown in Fig. 50. The energy detector does

not require training and declares a landmine present if the energy of the response is greater than a threshold. To avoid bias in the real part of the response, which is due to the DC magnetization of the soil, the energy is computed using the mean of the imaginary part of the response. Compared to other methods, the energy-detection performance is rather poor.

Figure 50 also includes the ROC curve for the method of Fails *et al.* [6] where the performance is evaluated on the same data set using LOOCV. While the proposed method is slightly better, the simulation done by Fails *et al.* does not utilize sequential measurements.

All the ROC curves in Fig. 50 saturate at 0.99 detection rate. This is due to the misclassification of one particular landmine. Upon close examination, it is found that the response of this landmine is very weak and is indistinguishable from the soil response. In the proposed framework, this target is filtered out by the soil prescreener. Other features, such as the soil response and the magnetic property of targets, may be included to provide even more robust performance. The study presented here only demonstrates the strong potential of using the DSRF for landmine detection.

CHAPTER V

CONCLUSIONS

In this thesis, two effective modeling techniques for EMI signals are developed: one for a single measurement vector and one for multiple measurement vectors. These techniques overcome several long-standing obstacles in estimating the discrete spectrum of an EMI response. This is achieved by first linearizing the problem through enumeration and then exploiting the notion of sparsity. The multiple-measurement technique exploits the invariance of the relaxation frequencies to further improve the estimation performance. The two techniques provide robust features for a DSRF-based classification that was developed to demonstrate the strong potential of DSRF-based subsurface target detection.

The main contribution of this research is a new technique in estimating the DSRF of a target from its EMI response, which enables DSRF-based subsurface target detection. Discriminating targets based on DSRF-like models has been studied for decades, but the inability to estimate the DSRF reliably has been the primary limiting factor until advances made by this research. The developed methods fall in the domain of detecting and discriminating subsurface targets using broadband EMI sensors. The contribution of this research has been to first characterize the EMI response of a target through modeling and then discriminate targets based on the characterizations using classification algorithms.

In Chapter 1, the motivation and background of subsurface target discrimination using broadband EMI sensors are provided. Two classes of broadband EMI model are introduced – continuous and discrete. It is argued that the discrete model is valuable for target discrimination due to the position and orientation invariance of the discrete relaxation frequencies. In this chapter, the difficulties in extracting the parameters of the discrete model, i.e., estimating the DSRF, are addressed. Previous works and their shortcomings are examined. A similarity map based on the DSRF for different types of targets is given to demonstrate the potential to classify, hence discriminate, targets based on the discrete model.

In Chapter 2, a sparsity-regularized DSRF estimation method using a single measurement is developed. The estimation problem is first linearized through enumeration in the relaxation frequency domain. The linearized problem is then solved by a sparsity-regularized least-squares. Through tests performed using synthetic, laboratory, and field data, this method is found to give satisfactory estimates. A soil model is proposed based on observed soil responses, and an augmented dictionary that includes the DSRF and the soil model is developed to model the target and soil response simultaneously. A simulation is performed to study the regularization parameter λ and then derive a simple formula for selecting λ as function of SNR.

In Chapter 3, the DSRF estimation method proposed in Chapter 2 is generalized to accommodate multiple measurements. Exploiting the invariance of the relaxation frequencies, a matrix equation is formulated with the property of row-sparsity. Using this row-sparsity, a robust DSRF estimation method is developed for the multiple-measurement case. Through simulations and tests using the laboratory and field data, this proposed method is found to be robust and fast. A performance gain over the single measurement method is observed over a wide range of SNRs in the simulated results.

In Chapter 4, the DSRF is applied to discriminate targets using classification algorithms in conjunction with the EMD. A soil prescreener is introduced to filter out responses that lack metallic objects. A detection framework is developed to include the soil prescreener, the DSRF estimation method, and the classifier. A sliding-window voting mechanism is introduced to discourage temporary mislabeling. The DSRF-based target detection is demonstrated to deliver high detection but low false-alarm rate. The detection framework provides a working example for DSRF-based subsurface target detection.

Two ideas for future research are suggested in Section 2.4.2 and Section 3.6. The first is to investigate the effect of soil and to *quantify* the range of signal-to-soil ratio in which the DSRF estimation performs satisfactory. The second is to perform a more comprehensive regularization parameter simulation that accounts for the nonuniform SNRs in multiple measurements. The results of this future research can further improve the robustness of the DSRF estimation methods.

APPENDIX A

THE EMI MODEL

The physical electromagnetic model of the EMI response and its relation to the discrete EMI model is presented here. It is also discussed here the relationship among several forms of the EMI model, including time-domain and frequency-domain model.

A.1 A Physical Model for the EMI Response

The EMI response of a metallic object is the result of the interaction between the transmitting loops, the receiving loops, and the object's magnetic polarizability $\boldsymbol{M}$ [63]. It can be shown by using reciprocity that response $H(\omega)$ is

$$H(\omega) = \alpha {\mathrm{H_R}}^T \boldsymbol{M}(\omega) \mathrm{H_T}, \tag{67}$$

where α is a real constant, $\mathrm{H_T}$ is the magnetic field generated by the transmitting loop, $\mathrm{H_R}$ is the magnetic field of the receiving loop if it is driven, and $\boldsymbol{M}$ is a complex, frequency independent, second-rank tensor.

Equation (67) can be expanded because the magnetic polarizability of a target can be written as a sum of relaxations [64]:

$$\boldsymbol{M}(\omega) = T_0 \boldsymbol{T}_0 - \sum_{k=1} T_k \left(\frac{j\omega/\zeta_k}{1 + j\omega/\zeta_k}\right) \boldsymbol{T}_k, \tag{68}$$

where T_k is a real constant and $\boldsymbol{T}_k$ is a real, symmetric, second-rank tensor. The first term is due to the bulk magnetic permeability of the target, which is assumed to be frequency independent, and the second term is due to the currents induced in the target [63].

Expanding $\boldsymbol{M}$ in (67) using (68), the response becomes

$$\begin{aligned} H(\omega) &= \alpha {\mathrm{H_R}}^T \left[T_0 \boldsymbol{T}_0 - \sum_{k=1} T_k \left(\frac{j\omega/\zeta_k}{1 + j\omega/\zeta_k}\right) \boldsymbol{T}_k \right] \mathrm{H_T} \\ &= \alpha \left[T_0 {\mathrm{H_R}}^T \boldsymbol{T}_0 \mathrm{H_T} - \sum_{k=1} T_k \left(\frac{j\omega/\zeta_k}{1 + j\omega/\zeta_k}\right) {\mathrm{H_R}}^T \boldsymbol{T}_k \mathrm{H_T} \right] \end{aligned}$$

$$= d_0 - \sum_{k=1} d_k \frac{j\omega/\zeta_k}{1 + j\omega/\zeta_k}, \tag{69}$$

where $d_k = \alpha T_k \mathrm{H_R}^T \boldsymbol{T}_k \mathrm{H_T}$. Note that ζ_k is independent of position and orientation while d_k is dependent of the position and orientation of the target relative to the sensors. This form provides more intuition about the physical process of EMI, where, again, the first term is due to the bulk magnetic permeability of the target and the second term is due to the eddy currents induced in the target.

From (69), a unit-step time response can be obtained using the inverse Laplace transform:

$$\begin{aligned} h(t) &= \mathcal{L}^{-1} \left\{ \frac{1}{j\omega} \left[d_0 - \sum_{k=1} d_k \frac{j\omega/\zeta_k}{1 + j\omega/\zeta_k} \right] \right\} \\ &= \mathcal{L}^{-1} \left\{ \frac{d_0}{j\omega} - \sum_{k=1} \frac{d_k}{\zeta_k + j\omega} \right\} \\ &= d_0 u(t) - \sum_{k=1} d_k e^{-t\zeta_k} u(t) \end{aligned} \tag{70}$$

A.2 Forms of the EMI Model

The EMI model (69) can be written in other forms that are useful for signal processing. Two alternative forms are examined in this section. When the nonnegative least-squares method was first developed in this research, the following form was introduced [33]:

$$H(\omega) = r_0 + \sum_{k=1} \frac{r_k}{1 + j\omega/\zeta_k}, \tag{71}$$

where the parameters are related to the physical form (69) by

$$d_0 = r_0 + \sum_{k=1} r_k \qquad \text{and} \qquad d_k = r_k. \tag{72}$$

The relationship between (69) and (71) is as follows:

$$\begin{aligned} H(\omega) &= d_0 - \sum_{k=1} d_k \frac{j\omega/\zeta_k}{1 + j\omega/\zeta_k} \\ &= d_0 - \sum_{k=1} \left(d_k \frac{j\omega/\zeta_k}{1 + j\omega/\zeta_k} + d_k - d_k \right) \\ &= \left(d_0 - \sum_{k=1} dk \right) - \sum_{k=1} \left(d_k \frac{j\omega/\zeta_k}{1 + j\omega/\zeta_k} - d_k \frac{1 + j\omega/\zeta_k}{1 + j\omega/\zeta_k} \right) \end{aligned}$$

$$= \left(d_0 - \sum_{k=1} dk \right) + \sum_{k=1} \frac{d_k}{1 + j\omega/\zeta_k}$$
$$= r_0 + \sum_{k=1} \frac{r_k}{1 + j\omega/\zeta_k}.$$

In the sparsity-promoting methods, another form (6) was introduced to give uniform-normed columns in the linearized model, which is related to (71) by

$$\begin{aligned} H(\omega) &= r_0 + \sum_{k=1} \frac{r_k}{1 + j\omega/\zeta_k} - \left(r_0 + \sum_{k=1} \frac{r_k}{2} \right) + \left(r_0 + \sum_{k=1} \frac{r_k}{2} \right) \\ &= \sum_{k=1} \frac{(1 - 1/2 - j\omega/\zeta_k/2)\, r_k}{1 + j\omega/\zeta_k} + \left(r_0 + \sum_{k=1} \frac{r_k}{2} \right) \\ &= \left(r_0 + \sum_{k=1} \frac{r_k}{2} \right) + \sum_{k=1} \frac{r_k}{2} \frac{1 - j\omega/\zeta_k}{1 + j\omega/\zeta_k} \\ &= c_0 + \sum_{k=1} c_k \frac{1 - j\omega/\zeta_k}{1 + j\omega/\zeta_k}, \end{aligned} \tag{73}$$

$$\text{where} \qquad c_0 = r_0 + \sum_{k=1} \frac{r_k}{2} \qquad \text{and} \qquad c_k = \frac{r_k}{2}. \tag{74}$$

This uniform-norm model (73) is relate to the physical form (69) using (72) and (74):

$$d_0 = c_0 + \sum_{k=1} c_k \qquad \text{and} \qquad d_k = 2c_k. \tag{75}$$

The form in (73) is preferred for the DSRF estimation because $\frac{1-j\omega/\zeta_k}{1+j\omega/\zeta_k}$ has a unit norm independent of ζ_k, so the dictionary in (16), populated by enumerating $\frac{1-j\omega/\zeta_k}{1+j\omega/\zeta_k}$, has columns with equal norms, implying that each $\tilde{\zeta}_m$ is equally likely to be selected by the DSRF estimator. This is true because the proposed DSRF estimation (18) minimizes the ℓ_p norm, and the ℓ_p norm discourages large entries. If a column has a smaller norm, then its corresponding entry in the weighted selection vector needs to take on a larger value to compensate the small column norm, which is penalized. Therefore, selecting a column with a smaller norm is penalized more compared to other columns with larger norms. For this reason, a dictionary with uniform column norms is desired and the unit-norm form for $H(\omega)$ (73) is preferred.

APPENDIX B

JOINTLY SPARSE VECTOR RECOVERY VIA ITERATIVELY REWEIGHTED ℓ_1 MINIMIZATION

The sparse minimization problem (45) can be approximated by minimizing the log-sum objective function on the norm of the rows:

$$\arg\min_{X} \sum_{m=1}^{M+1} \log\left(||\mathbf{x}_{\mathrm{m}}||_q + \epsilon\right) \quad \text{s.t.} \quad \boldsymbol{B} = \boldsymbol{A}\boldsymbol{X}, \tag{76}$$

where $\epsilon > 0$ is a small positive real number introduced for stability. Recall that $||\mathbf{x}_{\mathrm{m}}||_q \geq 0$ are the entries of $\mathcal{R}_{\ell_q}(\boldsymbol{X})$, the ℓ_q-norm of the rows of $\boldsymbol{X}$ defined in (32). For simplicity, $q = 1$ is considered here.

Following the reweighting scheme in [40], (76) can be solved with an iterative algorithm referred here as M-IRL1:

Step 1) Initialize count $i = 0$ and $w_m^{(0)} = 1$, $i = 1, \ldots, M+1$.

Step 2) Solve the weighted ℓ_1 minimization problem

$$\boldsymbol{X}^{(i)} = \arg\min_{\boldsymbol{X}} ||\mathbf{W}^{(i)}\mathcal{R}_{\ell_1}(\boldsymbol{X})||_1 \quad \text{subject to} \quad \boldsymbol{B} = \boldsymbol{A}\boldsymbol{X},$$
$$\text{where } \mathbf{W}^{(i)} = \mathrm{diag}[w_1^{(i)}, w_2^{(i)}, \ldots, w_{M+1}^{(i)}]. \tag{77}$$

Step 3) Update the weights:

$$w_m^{(i+1)} = \frac{1}{||\mathbf{x}_{\mathrm{m}}||_1^{(i)} + \epsilon}, \quad m = 1, \ldots, M+1. \tag{78}$$

Step 4) Terminate on convergence or when i reaches a specified maximum number of iterations $i_{\max}$. Otherwise, iterate from Step 2.

While (76) better promotes sparsity, it is nonconvex and a unique solution is not guaranteed. The proposed M-IRL1 method can be trapped in local minima. However, when an initial point is properly chosen, the algorithm does converge to the global minimum, as shown empirically in Section 3.3. The proposed method converges as argued in [50].

B.1 Algorithm Justification

This section provides a justification for the proposed method. A similar derivation is found in [40], which is the following with $L = 1$.

In (76), substitute for $||\mathbf{x}_\mathrm{m}||_q$ using (31):

$$\arg\min_{\boldsymbol{X}} \sum_{m=1} \log\left(\sum_{l=1}^{L} |x_{m,l}| + \epsilon\right) \quad \text{s.t.} \quad \boldsymbol{B} = \boldsymbol{A}\boldsymbol{X}. \tag{79}$$

The minimization in (79) is equivalent to

$$\arg\min_{s} \sum_{m=1} \log\left(\sum_{l=1}^{L} u_{m,l} + \epsilon\right) \quad \text{s.t.} \quad s \in \mathcal{C}, \tag{80}$$

where $s = (\boldsymbol{X}, \boldsymbol{U})$ and $\mathcal{C}$ is the convex set $\{(x_{m,l}, u_{m,l}) \,|\, \boldsymbol{B} = \boldsymbol{A}\boldsymbol{X} \text{ and } |x_{m,l}| \le u_{m,l}\}$.

Recognizing the objective function in (80) is concave, which is below its tangent, a guess $s^{(k)} \in \mathcal{C}$ can be improved by minimizing a linearized objective function around $s^{(k)}$:

$$\begin{aligned} s^{(k+1)} = \arg\min_{s} g(s^{(k)}) + \nabla g(s^{(k)})(s - s^{(k)}) \text{ s.t. } s \in \mathcal{C}, \\ \text{where } g(s) = \sum_{m=1} \log\left(\sum_{l=1}^{L} u_{m,l} + \epsilon\right). \end{aligned} \tag{81}$$

It can be readily shown that

$$\frac{\partial g}{\partial u_{m,l}} = \left(\sum_{l=1}^{L} u_{m,l} + \epsilon\right)^{-1}. \tag{82}$$

From (81) and (82),

$$\begin{aligned} (\boldsymbol{X}^{(k+1)}, \boldsymbol{U}^{(k+1)}) = \arg\min \sum_{m=1} \frac{\sum_{l=1}^{L} u_{m,l}}{\sum_{l=1}^{L} u_{m,l}^{(k)} + \epsilon} \\ \text{s.t.} \quad \boldsymbol{B} = \boldsymbol{A}\boldsymbol{X} \text{ and } |x_{m,l}| \le u_{m,l}, \end{aligned} \tag{83}$$

which is equivalent to

$$\boldsymbol{X}^{(k+1)} = \arg\min \sum_{m=1} \frac{\sum_{l=1}^{L} |x_{m,l}|}{\sum_{l=1}^{L} |x_{m,l}^{(k)}| + \epsilon} \quad \text{s.t.} \quad \boldsymbol{B} = \boldsymbol{A}\boldsymbol{X}.$$

Using (31),

$$\boldsymbol{X}^{(k+1)} = \arg\min \sum_{m=1} \frac{||\mathbf{x}_\mathrm{m}||_q}{||\mathbf{x}_\mathrm{m}||_q^{(k)} + \epsilon} \quad \text{s.t.} \quad \boldsymbol{B} = \boldsymbol{A}\boldsymbol{X}. \tag{84}$$

The iteration and weights in (84) define the proposed algorithm.

APPENDIX C

EARTH MOVER'S DISTANCE

Given two distributions $\hat{S} = \{(\hat{\zeta}_i, \hat{c}_i) : i = 1 \dots \hat{K}\}$ and $S = \{(\zeta_j, c_j) : j = 1 \dots K\}$, the Earth Mover's Distance (EMD) between the two distributions can be computed by solving the optimization problem [43]:

$$\text{EMD}(\hat{S}, S) = \min_{f_{ij}} \frac{\sum_{i=1}^{\hat{K}} \sum_{j=1}^{K} f_{ij} d_{ij}}{\sum_{i=1}^{\hat{K}} \sum_{j=1}^{K} f_{ij}} \tag{85}$$

$$\text{subject to} \quad \sum_{j=1}^{K} f_{ij} \leq \hat{c}_i \quad i = 1 \dots \hat{K} \tag{86}$$

$$\sum_{i=1}^{\hat{K}} f_{ij} \leq c_j \quad j = 1 \dots K \tag{87}$$

$$\sum_{i=1}^{\hat{K}} \sum_{j=1}^{K} f_{ij} = \min(\sum_{i=1}^{\hat{K}} \hat{c}_i, \sum_{j=1}^{K} c_j) \tag{88}$$

$$f_{ij} \geq 0 \quad i = 1 \dots \hat{K},\ j = 1 \dots K \tag{89}$$

where f_{ij} is an intermediate variable used during the optimization and d_{ij} is the distance function. Adapting the illustration in Section 2.2.1, $\hat{S}$ is the piles of earth and S the holes. Equation (86) guarantees no overdraw from each pile of earth, (87) guarantees no over fill at each hole, (88) sets the problem to fill up the holes with as much earth as possible, and (89) allows only moving earth into holes and not the reverse.

In this work, spectra should be normalized having sum of all spectral amplitudes be unity ($\sum c_i = 1$). In this case, the above optimization problem is simplified to having the denominator in (85) be one and the right-hand-side of (88) be unity. The EMD also becomes symmetric.

REFERENCES

[1] International Campaign to Ban Landmines, *Landmine Monitor 2010*. Ottawa: Mines Action Canada, 2010.

[2] L. Collins, P. Gao, and L. Carin, "An improved Bayesian decision theoretic approach for land mine detection," *IEEE Trans. Geosci. Remote Sens.*, vol. 37, no. 2, pp. 811–819, Mar. 1999.

[3] D. A. Keiswetter, I. J. Won, J. Miller, T. Bell, E. Cespedes, and K. O'Neill, "Discriminating capabilities of multifrequency EMI data," in *Proc. IGARSS*, vol. 4, Honolulu, HI, Jul. 2000, pp. 1415–1417.

[4] P. Gao, L. Collins, P. M. Garber, N. Geng, and L. Carin, "Classification of landmine-like metal targets using wideband electromagnetic induction," *IEEE Trans. Geosci. Remote Sens.*, vol. 38, no. 3, pp. 1352–1361, May 2000.

[5] L. S. Riggs, J. E. Mooney, and D. E. Lawrence, "Identification of metallic mine-like objects using low frequency magnetic fields," *IEEE Trans. Geosci. Remote Sens.*, vol. 39, no. 1, pp. 56–66, Jan. 2001.

[6] E. B. Fails, P. A. Torrione, W. R. Scott, Jr., and L. M. Collins, "Performance of a four parameter model for modeling landmine signatures in frequency domain wideband electromagnetic induction detection systems," in *Proc. SPIE*, vol. 6553, Orlando, FL, Apr. 2007, p. 65530D.

[7] G. Ramachandran, P. D. Gader, and J. N. Wilson, "GRANMA: Gradient angle model algorithm on wideband EMI data for land-mine detection," *IEEE Geosci. Remote Sens. Lett.*, vol. 7, no. 3, pp. 535–539, 2010.

[8] W. R. Scott, Jr., "Broadband array of electromagnetic induction sensors for detecting buried landmines," in *Proc. IGARSS*, Boston, MA, Jul. 2008.

[9] H. Nyquist, "Thermal agitation of electric charge in conductors," *Physical Review*, vol. 32, no. 1, pp. 110–113, 1928.

[10] F. S. Grant and G. F. West, *Interpretation Theory in Applied Geophysics*. New York: McGraw-Hill, 1965, ch. 17.

[11] S. H. Ward, "Electromagnetic theory for geophysical applications," in *Mining Geophysics*, D. A. Hansen, W. E. Heinrichs, Jr., R. C. Holmer, R. E. MacDougall, G. R. Rogers, J. S. Sumner, and S. H. Ward, Eds. Tulsa, OK: The Society of Exploration Geophysicists, 1967, vol. 2, ch. 2, pp. 10–196.

[12] C. E. Baum, "On the singularity expansion method for the solution of electromagnetic interaction problems," Air Force Weapons Laboratory, Interaction Notes 88, 1971.

[13] A. A. Kaufman and P. A. Eaton, *The theory of inductive prospecting*. Amsterdam: Elsevier, 2001, ch. 3.

[14] J. T. Miller, T. H. Bell, J. Soukup, and D. Keiswetter, "Simple phenomenological models for wideband frequency-domain electromagnetic induction," *IEEE Trans. Geosci. Remote Sens.*, vol. 39, no. 6, pp. 1294–1298, Jun. 2001.

[15] K. S. Cole and R. H. Cole, "Dispersion and absorption in dielectrics I. Alternating current characteristics," *J. Chem. Phys.*, vol. 9, no. 4, pp. 341–351, Apr. 1941.

[16] G. D. Sower, "Eddy current responses of canonical metallic targets theory and measurements," EG&G MSI, Interaction Notes 526, May 1997.

[17] D. W. Davidson and R. H. Cole, "Dielectric relaxation in glycerol, propylene glycol, and n-propanol," *J. Chem. Phys.*, vol. 19, no. 12, pp. 1484–1490, Dec. 1951.

[18] S. Havriliak and S. Negami, "A complex plane representation of dielectric and mechanical relaxation processes in some polymers," *Polymer*, vol. 8, pp. 161–210, 1967.

[19] N. Geng, C. E. Baum, and L. Carin, "On the low-frequency natural response of conducting and permeabletargets," *IEEE Trans. Geosci. Remote Sens.*, vol. 37, no. 1, pp. 347–359, Jan. 1999.

[20] M. McFadden and W. R. Scott, Jr., "Computing simple models for scatterers in eddy current problems using a modal decomposition [prepublished]," *IEEE Trans. Geosci. Remote Sens.*

[21] A. N. Tikhonov, "Solution of incorrectly formulated problems and the regularization method," *Sov. Math. Dokl.*, vol. 4, pp. 1035–1038, Oct. 1963.

[22] R. L. Wolpert, K. Ickstadt, and M. B. Hansen, "A nonparametric Bayesian approach to inverse problems," in *Bayesian Statistics 7*, J. M. Bernardo, A. P. Dawid, J. O. Berger, M. West, D. Heckerman, M. J. Bayarri, and A. F. M. Smith, Eds. Oxford, UK: Clarendon Press, 2003, pp. 403–418.

[23] E. Tuncer and S. M. Gubanski, "On dielectric data analysis. Using the Monte Carlo method to obtain relaxation frequency distribution and comparing non-linear spectral functionfits," *IEEE Trans. Dielectr. Electr. Insul.*, vol. 8, no. 3, pp. 310–320, Jun. 2001.

[24] J. Xiang, N. B. Jones, D. Cheng, and F. S. Schlindwein, "Direct inversion of the apparent complex-resistivity spectrum," *Geophysics*, vol. 66, no. 5, pp. 1399–1404, 2001.

[25] Y. Hua and T. K. Sarkar, "Matrix pencil method for estimating parameters of exponentially damped/undamped sinusoids in noise," *IEEE Trans. Acoust., Speech, Signal Process.*, vol. 38, no. 5, pp. 814–824, 1990.

[26] T. K. Sarkar and O. Pereira, "Using the matrix pencil method to estimate the parameters of a sum of complex exponentials," *IEEE Antennas Propag. Mag.*, vol. 37, no. 1, pp. 48–55, Feb. 1995.

[27] M. R. Osborne and G. K. Smyth, "A modified Prony algorithm for exponential function fitting," *SIAM J. Sci. Comp.*, vol. 16, no. 1, pp. 119–138, 1995.

[28] M. L. V. Blaricum and R. Mittra, "A technique for extracting the poles and residues of a system directly from its transient response," *IEEE Trans. Antennas Propag.*, vol. 23, no. 6, pp. 777–781, 1975.

[29] E. C. Levy, "Complex-curve fitting," *IRE Trans. Automat. Contr.*, vol. 4, pp. 37–43, 1959.

[30] Y. Das and J. E. McFee, "Limitations in identifying objects from their time-domain electromagnetic induction response," in *Proc. SPIE*, vol. 4742, Orlando, FL, Apr. 2002, pp. 776–788.

[31] S. L. Tantum and L. M. Collins, "A comparison of algorithms for subsurface target detection and identification using time-domain electromagnetic induction data," *IEEE Trans. Geosci. Remote Sens.*, vol. 39, no. 6, pp. 1299–1306, Jun. 2001.

[32] K. Ho, L. Collins, L. Huettel, and P. Gader, "Discrimination mode processing for EMI and GPR sensors for hand-held land mine detection," *IEEE Geosci. Remote Sens. Lett.*, vol. 42, no. 1, pp. 249–263, Jan. 2004.

[33] M. Wei, W. R. Scott, Jr., and J. H. McClellan, "Robust estimation of the discrete spectrum of relaxations for electromagnetic induction responses," *IEEE Trans. Geosci. Remote Sens.*, vol. 48, no. 3, pp. 1169–1179, Mar. 2010.

[34] M. Wei, "Estimation of the discrete spectrum of relaxations for electromagnetic induction responses," Master's thesis, Georgia Institute of Technology, Atlanta, 2011.

[35] Y. Rubner, C. Tomasi, and L. J. Guibas, "A metric for distributions with applications to image databases," in *Proc. ICCV*, Bombay, India, Jan. 1998, pp. 59–66.

[36] C. D. Austin, E. Ertin, J. N. Ash, and R. L. Moses, "On the relation between sparse sampling and parametric estimation," in *Proc. DSP Workshop*, Marco Island, FL, Jan. 2009, pp. 387–392.

[37] P. C. Hansen, *Rank-Deficient and Discrete Ill-Posed Problems: Numerical Aspects of Linear Inversion.* Philadelphia, PA: Society for Industrial Mathematics, 1998.

[38] K. Holmström and J. Petersson, "A review of the parameter estimation problem of fitting positive exponential sums to empirical data," *App. Math. and Comp.*, vol. 126, no. 1, pp. 31–61, Feb. 2002.

[39] R. Chartrand and W. Yin, "Iteratively reweighted algorithms for compressive sensing," in *ICASSP*, Las Vegas, NV, Mar. 2008, pp. 3869–3872.

[40] E. J. Candès, M. B. Wakin, and S. P. Boyd, "Enhancing sparsity by reweighted ℓ_1 minimization," *J. Fourier Anal. Appl.*, vol. 14, no. 5, pp. 877–905, 2008.

[41] M. A. T. Figueiredo and R. D. Nowak, "A bound optimization approach to wavelet-based image deconvolution," in *ICIP*, vol. 2, Genoa, Italy, Sep. 2005, pp. 782–785.

[42] S. J. Kim, K. Koh, M. Lustig, and S. Boyd, "An efficient method for compressed sensing," in *ICIP*, vol. 3, San Antonio, TX, Sep. 2007, pp. 117–120.

[43] B. Fisher. (2012, Apr.) The earth mover's distance. [Online]. Available: http://homepages.inf.ed.ac.uk/rbf/CVonline/LOCAL_COPIES/RUBNER/emd.htm

[44] G. D. Larson and W. R. Scott, Jr., "Automated, non-metallic measurement facility for testing and development of electromagnetic induction sensors for landmine detection," in *Proc. SPIE*, vol. 7303, Orlando, FL, Apr. 2009, p. 73030X.

[45] Y. Das, "Effects of magnetic soil on metal detectors: preliminary experimental results," in *Proc. SPIE*, vol. 6553, New York, 2007, p. 655306.

[46] M. McFadden and W. R. Scott, Jr., "The effect of frequency-dependent properties of soils on EMI sensors [prepublished]," *IEEE Trans. Geosci. Remote Sens.*

[47] J. Chen and X. Huo, "Theoretical results on sparse representations of multiple-measurement vectors," *IEEE Trans. Signal Process.*, vol. 54, no. 12, pp. 4634–4643, 2006.

[48] D. L. Donoho, "Compressed sensing," *IEEE Trans. Inf. Theory*, vol. 52, no. 4, pp. 1289–1306, 2006.

[49] B. D. Rao and K. Kreutz-Delgado, "An affine scaling methodology for best basis selection," *IEEE Trans. Signal Process.*, vol. 47, no. 1, pp. 187–200, Jan. 1999.

[50] G. Harikumar and Y. Bresler, "A new algorithm for computing sparse solutions to linear inverse problems," in *ICASSP*, vol. 3, 1996, pp. 1331–1334.

[51] J. A. Tropp, "Greed is good: Algorithmic results for sparse approximation," *IEEE Trans. Inf. Theory*, vol. 50, no. 10, pp. 2231–2242, 2004.

[52] D. L. Donoho and M. Elad, "Optimally sparse representation in general (nonorthogonal) dictionaries via ℓ_1 minimization," vol. 100, no. 5. National Acad Sciences, 2003, pp. 2197–2202.

[53] S. F. Cotter, B. D. Rao, K. Engan, and K. Kreutz-Delgado, "Sparse solutions to linear inverse problems with multiple measurement vectors," *IEEE Trans. Signal Process.*, vol. 53, no. 7, pp. 2477–2488, 2005.

[54] M. Wei, W. R. Scott, Jr., and J. H. McClellan, "Jointly sparse vector recovery via reweighted ℓ_1 minimization," in *ICASSP*, Kyoto, Mar. 2012.

[55] J. A. Tropp, "Algorithms for simultaneous sparse approximation. Part II: Convex relaxation," *Signal Processing*, vol. 86, no. 3, pp. 589–602, 2006.

[56] M. Mishali and Y. C. Eldar, "Reduce and boost: Recovering arbitrary sets of jointly sparse vectors," *IEEE Trans. Signal Process.*, vol. 56, no. 10, pp. 4692–4702, 2008.

[57] J. A. Tropp, "Algorithms for simultaneous sparse approximation. Part I: Greedy pursuit," *Signal Processing*, vol. 86, no. 3, pp. 572–588, 2006.

[58] A. Lutoborski and V. N. Temlyakov, "Vector greedy algorithms," *J. Complexity*, vol. 19, no. 4, pp. 458–473, 2003.

[59] I. F. Gorodnitsky and B. D. Rao, "Sparse signal reconstruction from limited data using focuss: A re-weighted minimum norm algorithm," *IEEE Trans. Signal Process.*, vol. 45, no. 3, pp. 600–616, Mar. 1997.

[60] M. Grant, S. Boyd, and Y. Ye. (2012, Apr.) CVX: Matlab software for disciplined convex programming. [Online]. Available: http://cvxr.com/cvx/

[61] O. Chapelle, P. Haffner, and V. N. Vapnik, "Support vector machines for histogram-based image classification," *IEEE Trans. Neural Netw.*, vol. 10, no. 5, pp. 1055–1064, 2002.

[62] J. Zhang, M. Marszalek, S. Lazebnik, and C. Schmid, "Local features and kernels for classification of texture and object categories: A comprehensive study," in *CVPRW*, New York, 2006.

[63] W. R. Scott, Jr. and G. D. Larson, "Modeling the measured EM induction response of targets as a sum of dipole terms each with a discrete relaxation frequency," in *Proc. IGARSS*, Honolulu, Hawaii, Jul. 2010.

[64] C. E. Baum, "Low-frequency near-field magnetic scattering from highly, bu not perfectly, conducting bodies," in *Detection and Identification of Visually Obscured Targets*, C. E. Baum, Ed. Philadelphia, PA: Taylor & Francis, 1999, ch. 6, pp. 163–218.